# Automatic Image Analysis for Biomedical Research: Rapid Drug Susceptibility Testing and Investigation of Cell Specialization in Early Embryo

Submitted to
Graduate School of Information Science and Technology
Osaka University

January 2018

Andrey Grushnikov

*For my parents*

## Abstract

Cell analysis is one of the core procedures done frequently during the course of research in a number of fields, including bacteriology and embryology. The information about cell morphology, lineages, and growth characteristics is gathered with microscopes, providing visual data in the form of images for investigation. Human-based study of these images is labor-intensive, error-prone due to subjective biases, lacks reproducibility and gives the qualitative assessment of the subject, rather than the quantitative. These negative aspects emphasize the importance of an automatic solution for the cell analysis problem. Although a number of software applications, capable of performing cell detection and tracking, are available, they have to be heavily altered and tailored to solve each particular task, complicating the processing pipeline. This thesis presents image processing based solutions for two cell analysis problems: drug susceptibility testing and early stage embryo segmentation.

Drug susceptibility testing is a process where a bacteria strain resistance to multiple drugs with different concentration levels is investigated. Existing approaches for testing rely on processing with specialized equipment that provides results not earlier than 24 hours. Recently a new device, drug susceptibility testing microfluidic device, that performs analysis of cell images after 3 hours, has been introduced. Development of an algorithm for processing these images to extract cell features and determine, whether a strain is susceptible to a drug in presented concentration or not, was the focus of the research. The designed method showed more than 97% accuracy of estimating minimum inhibitory concentration on a dataset that contained 101 bacteria strains, tested in presence of 5 different drugs. The implementation of the algorithm was created as a stand-alone software application that is currently used frequently to perform drug susceptibility tests by biology experts.

Analysis of cell morphology at early stages of embryo development present interest for the medical community, for information about cell characteristics such as position, volume, size, and others facilitates designing comprehensive models of internal processes, occurring in the embryo during its growth, thus, leading to new treatments of genetic disorders and artificial tissue growth. To extract cell features cell segmentation must be carried out in advance. Previously introduced methods processed single or multiple phase contrast microscopy images and showed efficiency in segmenting embryos with 4 or fewer cells, yet were not able to achieve high accuracy for embryos with more blastomeres. Advances in fluorescence imaging allowed to target particular cell parts providing visual cues that simplify segmentation. The aim of the studies presented in this thesis was to design a method for automatic segmentation of early-stage embryos from multiple cross sections fluorescence images. This task was solved by constructing energy functions to describe desired segmentation and applying a 3D level set. The method achieved 93% accuracy for 4-cell embryos, yet it was lower for the higher number of blastomeres, reaching 75% for 32-cell embryo.

**Acknowledgments**

First and foremost, I want to express my enormous gratitude to my scientific supervisor Professor Yasushi Yagi for his guidance and encouragement throughout the long way towards my Ph.D.

I would also like to express appreciation to my second supervisor Professor Takeo Kanade under whose leadership I had pleasure and honor to work on my research. His always insightful feedback helped me to sharpen and broaden my thoughts in both scientific and engineering domains.

My special thanks go to Professors Yoshimi Matsumoto and Ritsuya Niwayama for providing data necessary for conducting experiments and contributing in testing the developed software applications for drug susceptibility testing and embryo segmentation.

I would also like to thank my dearest family and also my friends. Their emotional support and care helped me not to give up and continue moving towards my goal. Without them, this work probably would never be done.

Lastly, I would like to thank all the members of the music band CyberJizz: Nimrat, Jhonny Jazz-Hands and Zongo. Their splendid tracks kept me energized during writing this thesis.

## Publication list

Journal publications

- Andrey Grushnikov, Kazuma Kikuchi, Yoshimi Matsumoto, Takeo Kanade and Yasushi Yagi. Automatic Image Analysis for Rapid Drug Susceptibility Testing, Advanced Biomedical Engineering, vol. 6, pages 76-82, 2017, doi: 10.14326/abe.6.76
- Andrey Grushnikov, Ritsuya Niwayama, Takeo Kanade, and Yasushi Yagi. 3D Level Set Method for Blastomere Segmentation of Preimplantation Embryos in Fluorescence Microscopy Images. Machine Vision and Application, pages 1-11, 2017, doi: 10.1007/s00138-017-0880-0
- Yoshimi Matsumoto, Shouichi Sakakihara, Andrey Grushnikov, Kazuma Kikuchi, Hiroyuki Noji, Akihito Yamaguchi, Ryota Iino, Yasushi Yagi and Kunihiko Nishino. A Microfluidic Channel Method for Rapid Drug-Susceptibility Testing of Pseudomonas aeruginosa. PLoS One, vol. 11-2, 2016, doi: 10.1371/journal.pone.0148797

Conferences and workshops (without review)

- Andrey Grushnikov, Kazuma Kikuchi, Takeo Kanade, Yoshimi Matsumoto, Kunihiko Nishino, Yasushi Yagi. A Bacteria Cell Feature Extraction System for Drug Susceptibility Testing. The 18th Meeting on Image Recognition and Understanding, 2015
- Andrey Grushnikov, Kazuma Kikuchi, Takeo Kanade, Yoshimi Matsumoto, Kunihiko Nishino, Yasushi Yagi. An Automatic System for Drug Susceptibility Testing. The 10th International Workshop on Robust Computer Vision 21, 2015
- Kazuma Kikuchi, Andrey Grushnikov, Yoshimi Matsumoto, Kunihiko Nishino, Takeo Kanade, Yasushi Yagi. Cell Detection for Automatic Drug Susceptibility Testing System. The 10th International Workshop on Robust Computer Vision 21, 2015

## Contents


**1 Introduction** **2**
- 1.1 Image Processing in Biomedical Research . . . 2
- 1.2 Automated Cell Analysis . . . 3
- 1.3 Challenges and Goals . . . 3
- 1.4 Thesis Organization . . . 6

**2 Automatic drug susceptibility testing** **8**
- 2.1 Introduction . . . 8
  - 2.1.1 Introduction . . . 8
  - 2.1.2 Anitbiotic resistance crisis . . . 9
  - 2.1.3 Drug Susceptibility Testing . . . 11
  - 2.1.4 DSTM . . . 13
  - 2.1.5 DST with DSTM device . . . 14
- 2.2 Method: SVM for susceptibility estimation . . . 15
  - 2.2.1 Manual vs Automatic cell analaysis . . . 15
  - 2.2.2 Related work . . . 16
  - 2.2.3 Algorithm for drug susceptibility testing . . . 17
  - 2.2.4 Noise reduction and Illumination correction . . . 18
  - 2.2.5 Channel detection . . . 20
  - 2.2.6 Cell detection . . . 22
  - 2.2.7 Feature extraction . . . 23
  - 2.2.8 Susceptibility estimation with SVM . . . 25
  - 2.2.9 Minimum Inhibitory Concentration . . . 26
- 2.3 Experimental results . . . 27
  - 2.3.1 Dataset . . . 27
  - 2.3.2 Channel detection accuracy . . . 27
  - 2.3.3 Cell detection accuracy . . . 29
  - 2.3.4 Susceptibility estimation . . . 29
  - 2.3.5 Susceptibility estimation: 2h vs 3h incubation . . . 30
  - 2.3.6 MIC estimation accuracy . . . 32
  - 2.3.7 SVM classifier vs human expert . . . 32
- 2.4 Discussion . . . 33
  - 2.4.1 Comparison with existing DST methods . . . 33

2.4.2 Time lapse analysis . . . 34

**3 Automatic embryo segmentation** **37**
3.1 Introduction . . . 37
3.1.1 Cell analysis in embryology . . . 37
3.1.2 Embryo development and cell specialization . . . 38
3.1.3 Methods for blastomere segmentation . . . 39
3.1.4 Fluorescence microscopy . . . 41
3.1.5 Embryo segmentation from fluorescence images . . . 42
3.2 Method: 3D Level Set . . . 43
3.2.1 Segmentation methods . . . 43
3.2.2 3D level set segmentation . . . 44
3.2.3 Energy functions . . . 45
3.2.4 Level set evolving equations . . . 48
3.2.5 Fast two-cycle algorithm . . . 48
3.2.6 Discrete approximation . . . 50
3.3 Experimental results . . . 51
3.3.1 Dataset . . . 51
3.3.2 Qualitative accuracy evaluation . . . 51
3.3.3 Quantitative accuracy evaluation . . . 53
3.3.4 Comparison with other methods . . . 54
3.3.5 Analysis of individual energy terms . . . 54
3.4 Discussion . . . 56
3.4.1 Improving the accuracy . . . 56

**4 Conclusion** **58**

**Appendices** **70**

**A Implementation of the algorithm for DST with DSTM device** **72**
A.1 Implementation details . . . 72
A.2 Importing data . . . 73
A.3 Processing microscopy images . . . 73
A.4 Examining the results . . . 74
A.5 Processing speed . . . 74

**B Implementation of the algorithm for embryo segmentation** **76**
B.1 Implementation details . . . 76
B.2 Visualization of the segmentation . . . 80
B.3 Processing speed . . . 80

## List of Figures


1.1 Two input images of the DSTM device, used in analysis of drug susceptibility. Different drugs are applied to a singular strain of *Pseudomonas aeruginosa* resulting in distinct changes in cell morphology and number of live cells. . . . . 4
1.2 Fluorescence microscopy images of an embryo with four cells. Images in top row present membranes, while in the bottom row display cell nuclei. . 5

2.1 Charts that demonstrate increase in multidrug resistance in two common patogens *Escherichia coli* and *Pseudomonas aeruginosa* observed in the United States. . . . . 9
2.2 A chart illustrating the decrease of new antibiotics developed and approved worldwide over the past decade . . . . . 10
2.3 MIC determination of an isolate by microbroth dilution method using 96-well plate [21]. . . . . 12
2.4 Two methods of drug susceptibility testing: (a) gradient method is used to test an isolated strain of *Staphylococcus aureus*; (b) disk diffusion test used to determine resistance of *Escherichia coli* [49]. . . . . 13
2.5 An actual photograph and a scheme of the DSTM device, together with a microscopy image of the microfluidic channels with P. aeruginosa growing in the presence of different concentrations of ceftazidime (CAZ). . . . 14
2.6 Photographs of DSTM device channels illustrating cell responses to different antimicrobial agents: (a) cell elongation for ciprofloxacin, meropenem, piperacillin; (b) decrease in the number of living cells for amikacin; (c) formation of spheroplasts for meropenem. . . . . 15
2.7 A scheme of the proposed algorithm for processing an input image of DSTM device channel to extract cell features, estimate susceptibile for each drug concentration and obtain MIC . . . . . 18
2.8 An example of an input image and the result of executing noise reduction step of the proposed algorithm: (a) input image; (b) fitted quadratic polynomial; (c) output . . . . . 20
2.9 Images illustrating channel detection stage of the algorithm: (a) output of the Canny edge detector, applied to the result image of the illumination correction procedure; (b) lines representing channel border which were detected with the PPHT algorithm; (c) an input image with the detected channels displayed in yellow. . . . . 22

2.10 An illustration of steps of the cell detection procedure: (a) detection of vertices; (b) construction of the graph representation; (c) determining the longest route with satisfied smoothness constraint. . . . . 23
2.11 Two close-up examples of elongated cells (a, c) and results of the cell detection stage of the algorithm (b, d) for the corresponding images. . . . 23
2.12 Two examples of the binary image and the output of cell detection stage of the algorithm for a sensitive strain (a) and a resistant strain (b). . . . . 24
2.13 Two images of channels, used as control, illustrate that different bacteria strains show dissimilar growth rates even without any presence of antimicrobial agents. . . . . 24
2.14 The illustration of the SVM method, that solves the classification problem by constructing a hyperplane with the larges margin between classes. . . . 25
2.15 MIC is the minimum concentration of the applied drug to which the bacteria strain is susceptibile. . . . . 26
2.16 Images taken after 3h of incubation for 5 different drugs, applied to a single bacteria strain. . . . . 28
2.17 Example of a channel, which the algorithm was not able to detect correctly due to lack of dark pixels in the channel border. . . . . 28
2.18 Scatter plot that represents the accuracy of cell detection with the proposed algorithm. . . . . 29
2.19 Left image displays several overlapping cells as seen in the input image. Middle image presents the ground truth separation of cells. Image on the right shows misdetections. . . . . 30
2.20 ROC curves built for each one of five antimicrobial agents: amikacin (AMK), ciprofloxacin (CIP), meropenem (MPM), ceftazidime (CAZ), piperacillin (PPC) . . . . . 31
2.21 Example DSTM device microscope images taken after 2h (left) and 3h (right) of incubation. . . . . 32
2.22 Two cumulative charts demonstrating distribution of cells with particular lengths when all three samples are resistant to injected drug (left) and sensitive (right). . . . . 33
2.23 Time-lapse sequence images with CAZ injected into test channels. Each image from top left to bottom right was taken with a 15 minute interval. The first image was taken after 15 minutes from the beginning of incubation, and the last - after 3 hours. . . . . 35
2.24 Changes of cell count through time from the beginning of the incubation till 3h for a bacteria strain, grown in the presence of . . . . . 36

3.1 Phase-contrast images of human embryo development from day 0 to day 7. Following fertilization, embryos undergo a series of mitotic cell divisions forming morula at day 4. A fluid-filled structure composed of an inner cell mass called blastocyst forms at day 5. [80] . . . . . 38

3.2 Overview of the pre-implantation development of a mouse embryo during which a fertilized egg divides into increasingly smaller cells resulting in the formation of the blastocyst. . . . . 39
3.3 A 4-cell embryo captured with the Hoffman Modulation Contrast (HMC) technique. . . . . 40
3.4 Results of blastomere detection for Hough transform-based method (middle row) and LSCF (bottom row) [115]. . . . . 41
3.5 Cross sections images of a 4 cell embryo nuclei and membranes. To mark nuclei and membranes H2B-mCherry and mG proteins were used. . . . . 42
3.6 To perform segmentation of an embryo 3D level set method is applied to two Z-stacks of fluorescence microscopy images. One of the Z-stacks composed of images displaying cell membranes, while the other one contains visual information about cell nuclei positions. . . . . 43
3.7 A 3D model of a 4 cell embryo with labelled elements: membrane, nucleus, inner cell region. . . . . 44
3.8 Illustrations of the inner region energy terms: $E_{edge}(\phi_i)$ forces the detected inner region boundary to be closer to membrane; $E_{nucleus}(\phi_i)$ includes nuclei inside the cell regions; $E_{overlap}(\phi_i)$ prevents overlap. . . . . 46
3.9 Illustrations of the membrane energy terms: $E_{volume}(\psi)$ determines membrane location depending on intensity; $E_{overlap}(\psi)$ prevents overlap with inner regions; $E_{inclusion}(\psi)$ fills the gaps in the membrane. . . . . 47
3.10 3D reconstruction of segmentation results for inner cell regions and membranes for embryos containing 4, 8, 16, 24, and 32 cells. . . . . 52
3.11 Cross sections of embryos that contain 4, 8, 16, 24, and 32 blastomeres that display the results of the inner region segmentation with the developed method. . . . . 52
3.12 (a) An input cross section. (b) Inner cell regions detected with $E_{overlap}(\phi_i)$ term included into the definition. (c-d) Inner cell regions detected without using $E_{overlap}(\phi_i)$. . . . . 55
3.13 (a) An input cross section. (b) Detected inner cell regions. (c) Detected membranes with $E_{inclusion}(\psi)$. (d) Detected membranes without $E_{inclusion}(\psi)$. . . . . 56
3.14 (a) A 3D model reconstructed from the input cross sections of the 32 cell embryo. (b) A cross section of a 32 cell embryo. (c) Missdetection of membrane regions. . . . . 56

A.1 A screenshot of the graphical interface of the developed software applications. The menu panels on the left side of the application allow to choose imported images, manually select channel areas, and specify processing parameters. The central area is designated for displaying input and processed images. The panel of the right displays a frequency chart and cell characteristics. . . . . 73

A.2 A screenshot of the GUI of the application, where a channel area has been manually selected by the user. . . . . 74
A.3 Top row displays an example of cell miss-detection that occurs due to channel regions containing channel borders. Bottom row shows how shrinking of the channel area prevents treating channel borders as cells. . 75
A.4 Two different ways of examining output of the cell detector: (left) cells surrounded with bounding boxes; (right) colour coded cells. . . . . 75

B.1 A scheme of the implemented algorithm. First the sets $L_in$ and $L_out$ are computed for each inner cell region and membrane. Then the two cycle iterative algorithm is executed. . . . . 76
B.2 The graphical user interface of the application, that implements the 3D level set method. . . . . 80
B.3 Results of the segmentation, displayed on a cross-section, after several iteration steps. . . . . 81
B.4 Several images of the 3D renders of the segmentation results captured from different angles. . . . . 81

## List of Tables


2.1 Susceptibility estimation accuracies for feature vectors constructed from different cell characteristics . . . . . 30
2.2 Susceptibility estimation accuracy using a feature vector, reflecting only cell count and average length, on samples incubated for 2 h or 3 h . . . . 31
2.3 Accuracy of MIC estimation for different drugs based on a feature vector containing only cell count and average length. . . . . 32
2.4 MIC estimation with the trained SVM classifier vs criterie selected by a human expert . . . . . 33

3.1 Segmentation accuracies for inner cell regions presented as precision, recall, F-score for embryos with different number of blastomeres. . . . . 53
3.2 Segmentation accuracies for cell membranes presented as precision, recall, F-score for embryos with different number of blastomeres. . . . . 53
3.3 Comparison of inner cell region segementation accuracy achieved with the developed 3D level set method and watershed method. . . . . 54
3.4 Accuracy of cell region segmentation depending on weight values for an embryo with 8 cells presented as F-score . . . . . 55
3.5 Accuracy of membrane segmentation depending on weight values for an embryo with 8 cells presented as F-scores . . . . . 55

A.1 Processing speed, given in seconds, of the implemented algorithm for different average number of cells in a single channel. . . . . 75

B.1 Processing speed, measured in seconds, for embryos with different number of cells. . . . . 81

# Chapter 1

# Introduction

## 1.1 Image Processing in Biomedical Research

Biology is one of the scientific fields which heavily depends on processing visual information. The increased resolving power and efficiency of microscope hardware have allowed acquiring huge amount of precise visual information without any considerable effort. Imaging has become the main source of data collection for biologists, facilitating testing and validating new hypotheses.

Understanding the structure and dynamics of internal processes in living microorganisms with the help of new image capturing equipment has become the prime target of biological research. Significant endeavors have been made to modify existing imaging techniques or design new procedures to visualize cells with high specificity and accuracy.

For example, for continuous observations of cell culture growth, a variety of devices have been created and successfully tested on different types of cells. Futhermore, development of methods for using naturally fluorescent proteins and derived fluorescent probes and laser scanning confocal microscope allowed to target and display specific parts of cells. All these advances led to an explosive increase in the rate at which digital image data is acquired in biological studies.

With the increased number of images produced during observations, there is now a unified understanding in scientific community that sophisticated computational methods are desperately needed to support high-throughput biological research [78], [96], [120]. Such methods not only are necessary to handle a gigantic volume of data, but more importantly to provide a level of sensitivity and objectivity that human observer can not match [91].

An increasing number of efforts in applying computational image processing methods to biological data has been made [9], [30], [31], [101], [126]. Nevertheless, the field of automatic cellular bioimage analysis is still very much in its infancy. The application of computational tools is often limited to low-level signal manipulation, while the extraction of biologically meaningful information from the image data is still done manually.

There are a number of factors which make the task of automating high-level analyses of biology images challenging. First of all, the captured images can vary significantly, demanding to design a specific tool for each case individually. Next, both biologists and computer scientists have to work closely together to achieve the goal, requiring both sides

to have substantial knowledge of the two domains. Finally, the once developed method often has to be constantly adapted to support further biological research.

All these points have to be addressed in order to successfully apply the most advanced and powerful image processing and computational techniques to the task of automating extraction of valuable information from biology images.

## 1.2 Automated Cell Analysis

Analysis of cell morphology, growth, reaction to chemical agents is a frequently occurring problem in biological research. It is a core task in many different fields including bacteriology and embryology. The studies presented in this thesis were focused on solving the task of cell analysis automation in these two particular fields of biomedical research.

The emergence of new dangerous pathogens, resistant to the multitude of existing antimicrobial agents, requires meticulous search of effective drugs and establishing optimal dose for each individual patient. Thus, the process of investigating if a drug has an effect on a bacteria strain - drug susceptibility testing (DST) - is a task of crucial importance in the field of bacteriology. The process of DST has been partially automated by means of building new devices for cell growth and image acquisition. Furthermore, for some types of microorganisms fully automatic robotic systems have become commercially available not long ago. Despite their efficiency and ability to support full cycle of testing - from strain selection to measuring an optimal dose of a potent drug - such systems are not widely exploited due to high cost. Thus, the issue of designing a cheap, rapid approach for imaging and carrying out DST remains unresolved.

Investigation of an early development of organisms and related genetic diseases is one of the main topics of investigation in embryology. During early stages of growth, an embryo consists of similar looking cells which later transform to create different complex tissues. A complete detailed model of the process, during which cells become specialized, would not only greatly enhance detection rates of early abnormalities, but also facilitate engineering of transplant tissues for therapies. Even though a dramatic number of studies attempted to construct such model, none were able to fully explain observed phenomena. In addition to the intricate process taking place in an embryo the task of building a model is challenging due to an excessive quantity of visual data and lack of computer-based systems for automatic image analysis. Thus, a system capable of aiding in cell segmentation and analysis would be highly beneficial to this field of research.

## 1.3 Challenges and Goals

The primary motivation for the research projects, presented in this thesis, was to aid biology experts by automating the high-level analysis of processes related to cell growth and development. Two different problems in biomedicine were in the focus of the studies.

The first problem was the automation of drug susceptibility testing procedure. Drug susceptibility testing (DST) is a process of determination which drug at what minimum

concentration is effective against a bacteria strain. Not long ago a new approach of conducting DST has been proposed. It is based on investigating cell growth under influence of a drug with a specified concentration by observing images of cells growing in a specialized device - drug susceptibility testing microfluidic (DSTM) device [47]. Previously this has been done manually, resulting in significant time for data acquisition and more importantly reducing reproducibility. To overcome this deficiency an automatic algorithm was required to be able to detect cells, extract measurable characteristics and based on obtained data estimate if the drug was effective or not.

There were a number of challenges which needed to be resolved in order to design a robust, accurate tool. Input images of the DSTM device are taken with a camera attached to a phase contrast microscope. Hence they suffer from common drawbacks, such as noise, nonuniform illumination, and others (see Fig. 1.1). One of the observed reactions to drugs for some bacteria strains is elongation which causes the cells to be seen as occluded or overlapped in the input images. This factor increases the complexity of cell detection and demands to design a specific algorithm for handling such cases correctly. Finally, to identify if a drug has an effect it is vital to select and extract cell characteristics, corresponding to changes in bacteria growth, and then make the judgment based on this data.

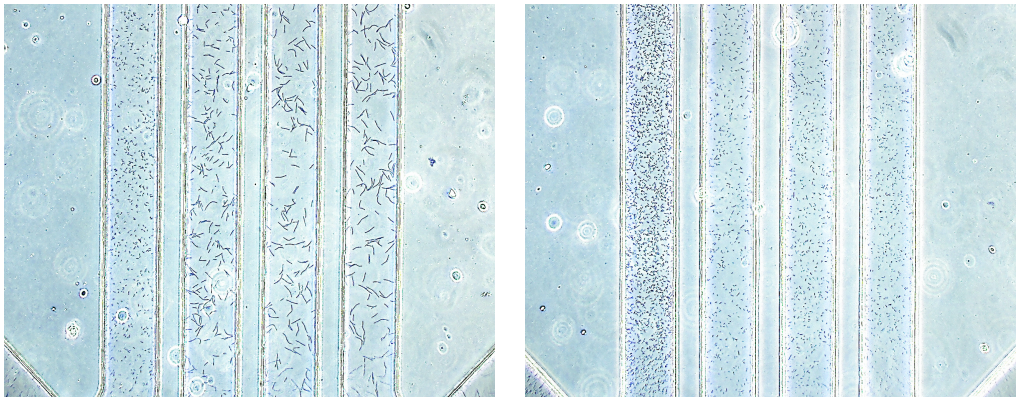

Figure 1.1: Two input images of the DSTM device, used in analysis of drug susceptibility. Different drugs are applied to a singular strain of *Pseudomonas aeruginosa* resulting in distinct changes in cell morphology and number of live cells.

The investigation of cell specialization during early stages of embryo development was the second biomedical problem the studies presented in this thesis were focused on. At early stages of growth, a mammalian embryo consists of identical cells, that are called blastomeres. In the course of growth these cells divide, transform and specialize to become part of a complex tissue. Factors, that contribute to the specialization process present a high interest for scientists, since this knowledge would allow developing techniques for growing artificial transplants and treatment of genetic illnesses. Recent studies revealed that important factors include cell morphology and position. Acquisition of this data by carrying out manual observations is sophisticated procedure that requires

a considerable amount of time.

It is possible to automate the process of examining cell characteristics by introducing a blastomere segmentation method that can further facilitate extracting of cell characteristics that present interest for biologists. Previously-reported approaches solve the segmentation problem for HMC microscopy images for embryo stages with not more than 4 cells [37], [105]. However, these methods aren't able to detect blastomeres for embryos with a higher number of cells successfully. Thus, the goal was to design a framework able to execute segmentation in these cases correctly.

Microscopy images taken with the HMC technique are not the best source of visual data to carry out segmentation. Cells, seen in these images, are overlapped, cluttered together and have side lit appearance. These factors are main obstacles, preventing the development of a simple elegant method for segmentation. Instead of attacking the problem straightforward, attempting to get around the mentioned drawbacks, it was decided to use an alternative imaging approach, fluorescence microscopy, to acquire input data (see Fig. 1.2). Therefore, the main aim was set as to design a segmentation algorithm for cell detection from the 3D data, presented as stacks of fluorescence microscopy images. A challenging issue was to address embryo morphology to produce robust and accurate results.

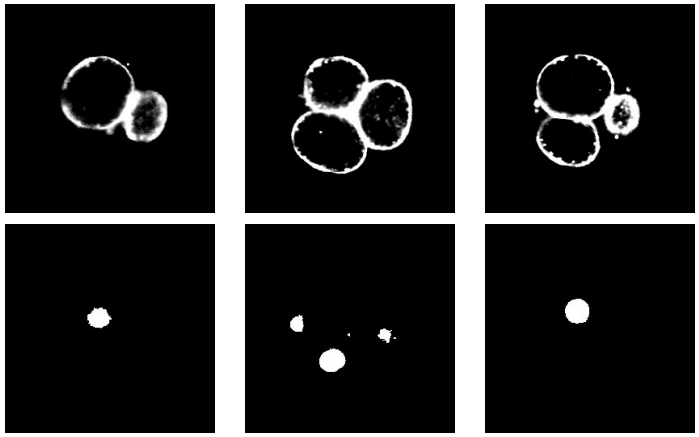

Figure 1.2: Fluorescence microscopy images of an embryo with four cells. Images in top row present membranes, while in the bottom row display cell nuclei.

Regardless of different biological background, the two problems in their core share the same objective - cell detection. Yet in each particular case, the cells visible on input images have remarkably different appearances. In case of cell detection for DST with the DSTM device the bacteria are seen as small connected regions of black pixels, while, on the other hand, blastomeres in the study of early-stage embryo occupy a substantial area of input cross sections and provide visual cues for the location of membranes and nuclei. This difference in observable morphology prevents the adoption of identical approaches for both task, thus forcing to tailor a separate method for each individual problem.

In this thesis, I present two methods for automatizing of the cell analysis problem for

two biomedical tasks reviewed above: drug susceptibility testing with the DSTM device and and investigation of cell specialization in early stage mammalian embryos.

I solved the problem of drug testing automation by introducing an algorithm that, first, detects each individual microfluidic channel of the DSTM device, present in the image, then executes cell detection, followed by feature extraction. The obtained cell characteristics are fed into a support vector machine that predicts whether a bacteria strain is affected by a drug with particular concentration. The method overcomes the issue of nonuniform illumination of the input image by applying correction technique, while the matter of cell overlapping is addressed with the specialized cell separation procedure. The created algorithm was tested on a dataset that contained images of 101 bacteria strains grown in the presence of 5 different drugs, injected into microfluidic channels in 3 distinctive concentrations. Experimental result demonstrated the efficiency of the method, since it was able to achieve an average accuracy of 97% for estimation of minimum inhibitory concentration. The implementation was designed as a stand alone tool with a graphical interface, that can be effortlessly used even by non specialists for performing cell analysis [39].

For the second task, I proposed an energy minimisation approach based on 3D level set to perform segmentation of embryos at early stages of development into a membrane and inner cell regions. The level set functions were designed to describe various morphological features of the blastomeres as well as to penalize over-segmentation. The choice of particular procedure for solving PDEs defined by the level set was done in favor of the one that does not require solving PDE directly. Instead it uses simple operations over discrete sets, achieving a high speed of computation. The constructed algorithm was tested on a dataset, that contained embryos with 4-32 cells, achieving 90% accuracy for 4-cell and minimum of 75% for 32-cell cases. The implementation was also programmed as a stand-alone application with a graphical user interface.

## 1.4 Thesis Organization

This thesis is divided into two parts, presented in Chapter 2 and Chapter 3 respectively. The first part is dedicated to the problem of developing an algorithm for automation of drug susceptibility testing by processing microscopy images of bacteria cell cultures grown in the DSTM device. The second part describes a 3D level set based method for performing segmentation of a pre-implantation embryo from Z-stacks of fluorescence microscopy images.

Chapter 2 has the following structure. In section 2.1, an overview of biological background which prompted research in the field of antibiotics development is done. First, the data, that highlights an increasing tendency of bacteria strains to become resistant to multiple existing drugs is presented. Thereafter, existing techniques for DST are described. Next, the scheme of a novel DSTM device and manual procedure for testing and acquisition of minimum inhibitory concentration of a drug for a bacteria strain with this device is explained.

Section 2.2 is dedicated to reporting the developed method for automatic DST in details. First, existing approaches for automatic analysis of cells and their strong and weak points are reviewed and discussed. Next, an overview of five modules of the new algorithm is given, and then functioning of each module is explained in individual sections.

The description of the dataset and results of various types of testing, including accuracy evaluation for cell detection procedure, susceptibility estimation for each individual sample, and determination of the minimum concentration of a drug to which a strain is susceptible is presented in section 2.3.

The comparison of existing susceptibility testing methods and discussion of further improvements that could be achieved by processing time-lapse sequence of bacteria growing in the DSTM device are discussed in the last section (section 2.4). Details of the developed implementation, description of the functions of the released tool can be found in Appendix A.

The second part of this thesis, presented in Chapter 3, is focused on solving the segmentation problem for pre-implantation mammalian embryos. section 3.1 provides an overview of biological processes occurring in embryos on early stages of their growth. Next, the mechanism of cell specialization is explained and necessity of designing automatic system for carrying out analysis is stated. In this section various techniques for capturing microscopy images are also discussed.

Section 3.2 discuses existing approaches to the segmentation tasks, their advantages, and disadvantages. Thereafter, a detailed design of the 3D level set algorithm for segmenting embryo into inner cell regions and membranes is given. The implementation of the 3D level set method is described in the Appendix B

The results of testing on a dataset containing 4-32 cell embryos and analyses of the affect of individual energy terms on the final segmentation are presented in section 3.3. And the discussion of using alternative energy terms for increasing segmentation accuracy for embryos with more than 24 cells can be found in section 3.4.

The final section of the thesis dedicated to an overview of the conducted studies and achieved results.

# Chapter 2

# Automatic drug susceptibility testing

## 2.1 Introduction

### 2.1.1 Introduction

In rescent years a rapid increase of bacteria strains, resistant not to one, but to multiple antibiotics, has been observed. This is an extremely alarming issue which directly affects human health. The factors responsible for the emergence of resistance include innapropriate use of antibiotics, increase of immunocompromised patients and others. The multidrug resistant bacteria, such as *Pseudomonas aeruginosa*, have already caused nosocomial outbreaks in Japan [99], [100]. Few antibiotics are available for treating multidrug resistant infections and new drug development is lacking.

Traditional methods for investigating the susceptibility of clinically isolated strains are based on detailed analysis of gene expression to identify factors contributing to cell resistance. It takes significant time to perform testing, thus a method for rapid determination of susceptibility to select effective drugs for each individual patient promptly has been highly desired. Altough some newly developed methods reduce time to obtain results, the drug testing remains time consuming. One of the major reasons is that the existing approaches are mostly based on optical density or colorimetric methods to detect bacterial growth, which require control bacteria to become visible after the incubation of intact cells with drugs.

A number of methods, attempting to reduce the time needed to perform testing, have been proposed in the last decade. Some of them are based on analyses of microscopy images of bacteria cells [51], [89] while other approaches focus on desgining microfluidic chips facilitating observations of cell growth [18], [47], [52]. One of the proposed devices, a drug susceptibility testing microfluidic (DSTM) device [47], [70], allowed evaluating drug efflux pump activity for detection of infections and diagnosis of diseases. Its first version showed efficiency in permitting enzyme reactions following short turm incubation, but it was not useful for bacterial cultivation. The device was redesigned to have four microfluidic channels, sharing a single inlet hole, to be used for bacterial cultivation.

The protocol for estimating minimum inhibitory concentration to a drug for a bacteria strain with the DSTM device has been based on manual analyses of microscopy images.

The procedure starts with introduction of drugs with different concentrations into bacteria solution. After several hours of incubation in the controlled environment an image of the microfluidic channels of the device is taken by a camera, attached to a phase contrast microscope. The obtained image is then manually analyzed by comparing cell growth of a test and control sample. Abnormalities, such as alterations of cell morphology or decrease of vital bacteria, signify that the input strain is susceptible to a drug with a particular concentration. The MIC is obtained by observing cell reactions for a variety of drug concentrations and selecting the lowest one [47].

Manual visual inspection of the DSTM device channels for determination of MIC can provide useful qualitative information concerning alteration in cell numbers or morphology. At the same time this procedure is highly labor intensive, based on subjective biases, lacks reproducibility and prone to errors if carried out by a trained expert. Motivated by these drawbacks and inspired by the number of papers where image processing methods were successfully applied to solve biomedical problems, it was decided to develop a new algorithm for providing a quantiative base analysis for MIC determination with DSTM device.

### 2.1.2 Anitbiotic resistance crisis

For several decades emergence of multiple drug resistant bacteria strains has been a growing threat for countries worldwide [59], [62], [63]. The data, presented by the Center For Disease Dynamics, Economics & Politics (CDDEP) demonstrates that the percentage of strains of common pathogens *Pseudomonas aeruginosa* and *Escherichia coli*, which show resistance for a variation of antibiotics has increased (see Fig. 2.1) [113].

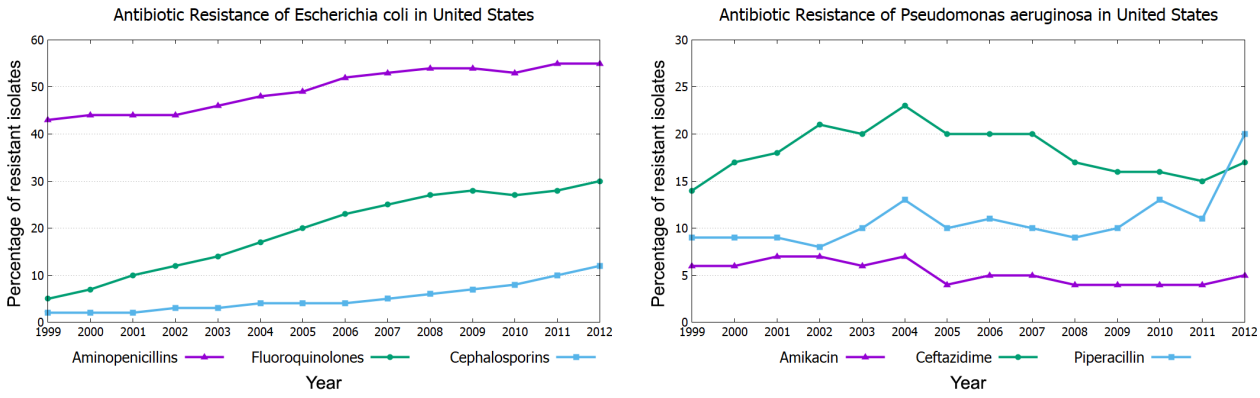


Figure 2.1: Charts that demonstrate increase in multidrug resistance in two common patogens *Escherichia coli* and *Pseudomonas aeruginosa* observed in the United States.

The term multidrug resistance (MDR) initially described resistant mammalian tumor cells, but later it has been extended to represent the multidrug resistance of any microorganism – bacterium, fungus or parasite. The emergence of MDR and antibiotic resistance crisis has been attributed to the overuse and misuse of antimicrobial agents and other

medications.

In bacteria, genes can be inherited from relatives or can be acquired from nonrelatives on mobile genetic elements such as plasmids. This horizontal gene transfer can allow antibiotic resistance to be transferred among different species of bacteria. Resistance can also occur spontaneously through mutation. Antibiotics remove drug sensitive competitors, allowing resistant bacteria to reproduce. Despite warnings regarding overuse, antibiotics are overprescribed worldwide [94].

Incorrectly assigned antibiotics also contribute to the promotion of resistant bacteria. Studies have shown that choice of agent or duration of antimicrobial agent is incorrect in 30% to 50% cases [74]. Subinhibitory concentrations of drugs can potentially support genetic alterations, such as changes in gene expression, and mutagenesis and lead to increasing resistance and virulence. This process has been observed for a number of common pathogens, including *Pseudomonas aeruginosa* [117].

Extensive agricultural use is an additional factor that boosts bacteria resistance. Antibiotics are commonly used in animals primarily to promote growth and to prevent infections [63], [107]. Treating livestock with antimicrobials is said to improve the overall health of the animals and produce larger yields. However, there is a downside to these actions as well. Drugs used in food-producing animals kill or suppresses susceptible bacteria, allowing to survive only those that acquired mechanisms to overcome agent's influence. Next, resistant bacteria are transmitted to humans through the food supply. These bacteria can cause infections in humans, leading to adverse health consequences.

The development of new antibiotics is no longer considered to be a wise economical investment for the pharmaceutical industry (see Fig. 2.2) [22], [48]. Antibiotics are not profitable as drugs, since research and testing require high expenses while the agents are used for relatively short periods of time [59]. Additional restraints imposed by infectious disease specialists regarding antibiotic use also lead to a decrease of commercial interest of investments.

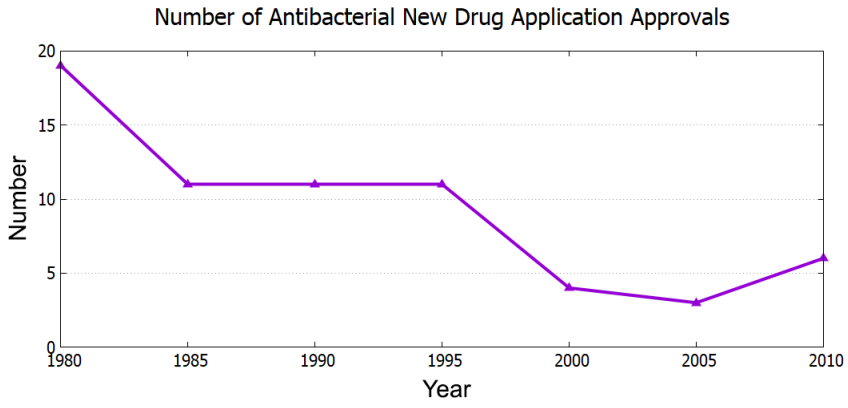


Figure 2.2: A chart illustrating the decrease of new antibiotics developed and approved worldwide over the past decade

All the factors presented above emphasize the importance of developing new antibiotics. In recent years a significant effort has been done to facilitate this process by introducing novel methods, techniques, and devices.

### 2.1.3 Drug Susceptibility Testing

An important task that is carried out during the clinical research of new potential antibiotic agents is the drug susceptibility testing (DST) of bacterial isolates. The goal of DST is to detect possible drug resistance in common pathogens as well as to determine the lowest concentration of antibiotic that prevents bacterial growth. This concentration is referred to as minimum inhibitory concentration (MIC).

There are two different types of DST: genotypic and phenotypic. Genotypic assays involve gene sequencing for detecting mutated genes, related to drug action and requires deep knowledge of internal mechanisms, occurring in bacteria cells. This type of testing uses complex specialized equipment and highly trained personnel. On the other hand, phenotypic assays measure the ability of a bacteria or a virus to grow in presence of different drug concentrations. During inspection replication of cells at different antibiotic concentrations is monitored and compared with replication of a reference control strain.

Unlike genotypic, phenotypic drug testing it is a simple process, however, it is rather time-consuming, since a full cycle of culture growth has to be observed for both control and test samples, and that has to be done for multiple drugs [49].

A commonly used DST method is a microbroth dilution method. This procedure involves preparing two-fold dilutions of antibiotics in a liquid growth medium dispensed in test tubes [32], [49]. Test tubes are assembled in trays, that often contain 96 wells of 0.1 mL volume. This design allows approximately 12 antibiotics to be tested in a range of 8 two-fold dilutions in a single tray (see Fig. 2.3). To carry out testing, drugs are pre-introduced and then the bacterial suspension is transferred into each well. Following incubation, MICs are determined manually or using an automated device by inspecting rate of cell growth. The accuracy of the method is very high, so it is commonly used for obtaining ground truth MIC for bacteria strains. The other advantage of this approach for MIC determination is relatively low cost of performing tests.

An alternative to broth dilution method is the antimicrobial gradient method. It is based on establishing a drug concentration gradient in an agar medium. A commercially available version employs a thin plastic test strips that contain on the underside a dried antibiotic concentration gradient and are marked on the upper side with a concentration scale. These strips are placed in a radial fashion on the surface of an agar plate that has been inoculated with a bacteria suspension (see Fig. 2.4 (a)) . The MIC is determined after an overnight of incubation by analyzing shapes of inhibition areas. Gradient method is most suitable for testing not more than 3 drugs simultaneously or when a microorganisms requires special incubation atmosphere [45], [49], [50].

The least costly of all susceptibility testing methods is the disk dilution susceptibility test [6], [19], [49]. To perform susceptibility testing with this method a bacterial inocu-

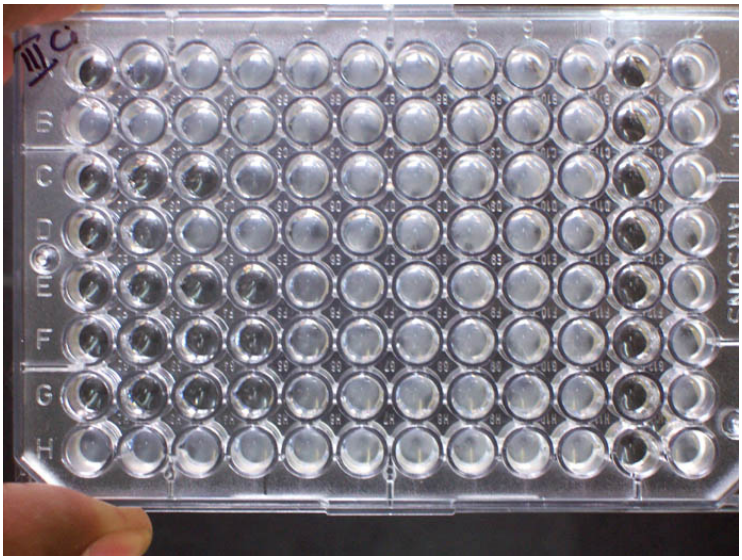


Figure 2.3: MIC determination of an isolate by microbroth dilution method using 96-well plate [21].

lum is applied to the surface of a large agar plate. Then paper antibiotic disks with fixed concentration of the agent are placed on the inoculated agar surface (see Fig. 2.4 (b)). Next, plates are incubated for 16-24 hours in a controlled environment. The zones of growth inhibition around each disk are measured and susceptibility to each drug is determined using criteria published by Clinical and Laboratory Standards Institute (CLSI) [19].

Several attempts to automatize the process of susceptibility testing have been made in order to standardize the readings and produce results in a shorter period of time [95]. For example, the MicroScan machined, developed by Siemens Healthcare Diagnostics, was designed to incubate and analyze up to 96 standard microdilution trays. The device grows manually prepared samples, examines them periodically with either a photometer or fluorometer. Finally, it applies advanced computer software to measure susceptibility and determine MIC. It takes approximately 22 hours to obtain results with the MicroScan system [76].

The Vitek 2 System (bioMerieux) uses compact plastic reagent cards, that contain small quantities of an antibiotic and test media in a 64-well format. The device can be configured to perform up to 240 simultaneous tests. It determines the susceptibility of a test by measuring the loss of intensity of transmitted light in the bacteria solution. The results of the tests are obtained after 4-10 hours of incubation.

A number of studies showed that rapid susceptibility tests reduce time, required to specify an appropriate antimicrobial agents, allowing to lower the cost of treatment due to a shortened length of stay, fewer laboratory tests and invasive procedures [5], [27]. Therefore, automatic DST systems provide valuable contribution towards rapid result acquisition by relieving experts from time-consuming labor-intensive work. However,

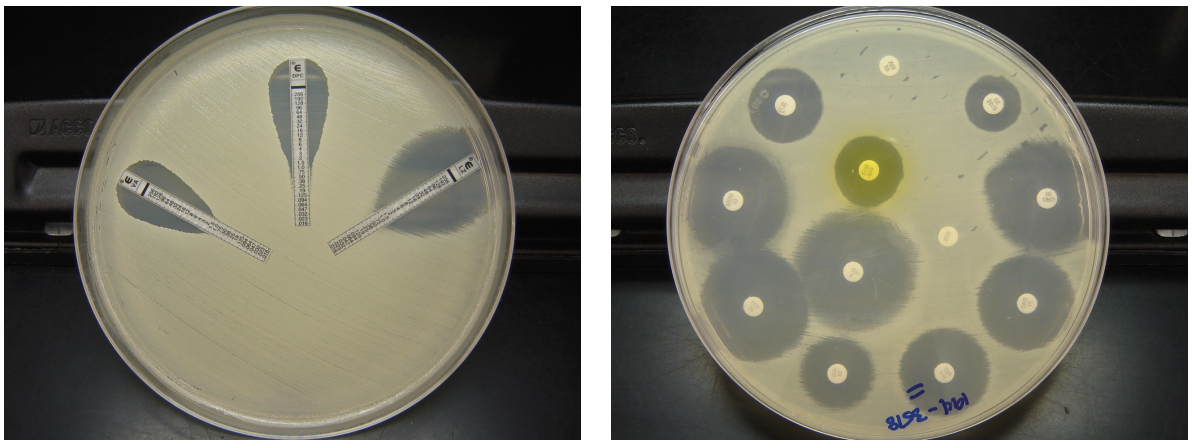

(a) (b)

Figure 2.4: Two methods of drug susceptibility testing: (a) gradient method is used to test an isolated strain of *Staphylococcus aureus*; (b) disk diffusion test used to determine resistance of *Escherichia coli* [49].

high price of the devices and necessity to perform full-length incubation cycle of bacteria isolates restricts the wide spread of these testing systems.

In rescently published works a number of new inexpensive devices and rapid DST techniques has been proposed [47], [51], [52], [92]. One of the proposed methods involves using the drug susceptibility testing microfluidic (DSTM) device designed by Matsumoto et al. [47], [71]. It was showed that this device can provide readable data in no more than 3 hours.

### 2.1.4 DSTM

The mechanisms of bacteria strain sensitivity are highly related to the efficiency of proteinaceous transporters, i.e. efflux pumps, localized in the cytoplasmic membrane. In particular, resistance-nodulation-cell division (RND) can decrease the sensitivity of such cells as *P. aerugionsa* [68]. Measuring activity of these efflux pumps allows easily determine levels of inhibition of an antimicrobial agent.

Not long ago Matsumoto et. al [70] and Iino et. al [47] proposed new techniques for a simple and rapid measurements of the activities of efflux pumps and inhibitors using microfluidic devices with different shape of channels. The following research of these groups was focused on improving the developed instruments and increasing accuracy of the observations. Their final design of the DSTM device allowed to acquire results of the DST in less than 3 hour period.

The DSTM device is prepared as follows. It contains five sets of four microfluidic channels, printed in a polymer on a cover glass by a conventional soft lithography method [122]. The width of the microfluidic channels is 100 $\mu m$, height 50 $\mu m$ and the length in the observation area is 3-5 mm (see Fig. 2.5) . Four channels in one set share inlet

hole allowing to perform observations of cell growth with an introduced drug with three different concentrations and a control sample. The protocol of susceptibility estimation with the DSTM device is presented in the next section.

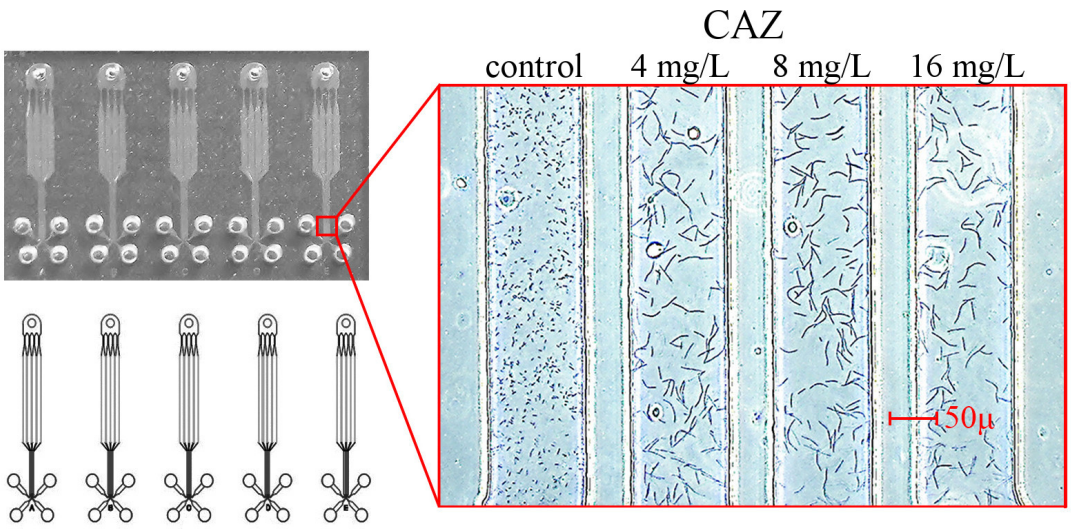


Figure 2.5: An actual photograph and a scheme of the DSTM device, together with a microscopy image of the microfluidic channels with P. aeruginosa growing in the presence of different concentrations of ceftazidime (CAZ).

### 2.1.5 DST with DSTM device

Determination of MICs for bacteria strains using the DSTM device is conducted as follows. At first, a drug is added at three different concentrations into three test microfluidic channels of one of the channel sets. The remaining channel is used as the control sample for the observations. The drug solution is dried, and then a cation-adjusted Mueller-Hinton broth of bacteria culture, grown in advance on Heart infusion agar, is introduced into the device using a micropipette. To completely separate each channel, air is introduced into the device from the shared inlet hole. Finally, the fully prepared device is incubated under humid conditions at 37°C for up to 3 hours.

The protocol of measuring the MIC consists of visual inspections of bacteria cells in each channel by phase contrast microscopy. An image of a set of microfluidic channels is taken with a camera attached to a phase contrast microscope. Visible differences in cell shape, number of cells between microorganisms, present in the test sample, and those in the control sample, signify that the input strain is susceptible to the used drug at a particular concentration. The minimum concentration of the drug to which the strain is susceptible constitutes its MIC.

The growth rate of each individual bacteria strain can differ from other strains. Thus, it is not possible to carry out comparison of the changes using a uniform control sample

for all range of strains. Hence, the control sample must be incubated together with the test samples to perform correct observations.

Bacteria cell responses to the presence of a drug vary greatly depending on the strain, antimicrobial agent, and its concentration. Among the most common reactions of the two widely spread pathogens *P. aeruginosa* and *E. coli* are elongation, cell number decrease and change of shape (see Fig. 2.6) .

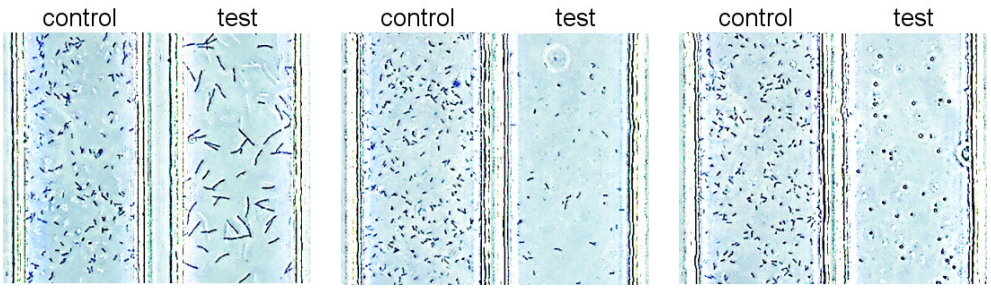


(a) (b) (c)

Figure 2.6: Photographs of DSTM device channels illustrating cell responses to different antimicrobial agents: (a) cell elongation for ciprofloxacin, meropenem, piperacillin; (b) decrease in the number of living cells for amikacin; (c) formation of spheroplasts for meropenem.

Manual measurements of these characteristics with visual inspection are extremely labor-intensive and time-consuming. Moreover, such approach is prone to errors due to subjective biases and lacks reproducibility. To overcome these drawbacks, an automatic tool able to extract desired cell features and perform the analysis has been highly desirable.

## 2.2 Method: SVM for susceptibility estimation

### 2.2.1 Manual vs Automatic cell analaysis

Examining cells with a microscope has long been a primary method for studying cellular mechanisms. Nowadays, with the advance of screening techniques and capturing devices, it is possible to easily collect thousands of high-resolution images from time-lapse experiments and from large-scale screens. A bottleneck exists at the image analysis stage. It is commonly done by visual inspection of obtained data by expert biologists. This process has a lot of hindrances and drawbacks.

First, due to direct manual measurements of cell features, human-scored image analysis is qualitative, rather than quantitative. Samples are usually categorized as 'hits' or 'non-hits'. By contrast, automated tools produce consistent quantitative measurements of a variety of cell characteristics for every image. Acquisition of large number of features has already proven useful for grouping genes and revealing drug mechanisms [14], [75].

Second, human-based inspection is not capable to assess each individual cell and conclusions and judgments are based on whole population data, which is not ideal for detailed investigation of internal processes. On the contrary, automatic approaches are able to measure features of each cell and even detect some characteristics that are not readily detectable by a human observer [41].

Third, manual analysis conducted by an expert is extremely time consuming and labor-intensive. Automatic methods are higher-throughput and generate reliable results from a large-scale experiment in hours, versus months of tedious visual inspection in case of manual processing of obtained data. This is a significant improvement, substituting routinely conducts for such experiments.

Thus, automatic cell analysis increases accuracy and reproducibility of the results; relieves human researchers from boring mundane work, allowing to focus on building models and verifying hypothesis; significantly reduced the time for data acquisition.

### 2.2.2 Related work

In recent years a number of software implementations based on different approaches were designed to perform cell detection, tracking, and analysis.

One of the oldest and most popular developed packages for biological image analysis is ImageJ [1]. This software has been successfully used by many laboratories. It supports most of the common and important formats of input images used in the field of biomedical images. In addition, it allows direct acquisition of data from scanners, cameras, and other video sources. This tool can perform basic operations, similar to Adobe Photoshop, such as edge detection, convolution, Fourier transform and particle analysis. The main advantages of the ImageJ include ability to run on different platforms and support user-written macros and plug-ins. Overall, ImageJ is a highly useful tool for performing preliminary general analysis of the target subject and preprocessing captured images. However, it is not particularly suitable for complex tasks and deep analysis.

While not creating a general, flexible software tool, many groups have benefited from dedicate automated cell detection and tracking instruments [9], [101].

For example, Carpenter et al. [13] presented an open-source system CellProfiler capable of simultaneously measuring size, shape, intensity, and texture of a variety of cell types in a high throughput manner. CellProfiler carries out illumination correction by applying common, as well as customly designed, algorithms [114]. Next, it applies a variety of well known robust techniques for identifying cells using fluorescence markers. In order to prevent miss-detection for cases where cells touch each other, the system utilizes a three-step strategy. First, clumped objects are recognized and separated; second, the dividing lines between objects are found; and third, some of the resulting objects are either removed or merged together, depending on their size or shape [13], [66]. To perform analysis CellProfiler measures a large number of simple and complex features for each cell including area, shape, intensity, texture, Zernike shape, Haarlick and Gabor texture features.

Automated image analysis software CellC was developed for quantification of bacterial cells and estimation of cell morphology in fluorescence images [101]. The procedure of microorganism identification is divided into two phases [54]. The first phase is segmentation and analysis of the cell count in images stained with *4',6-diamino-2-phenylindole*. The second phase is the calculation of cell count from the image obtained with fluorescence in situ hybridization [4]. The aim of the first phase is the extraction of individual cells from cell clusters to enable data acquisition on a cell-by-cell basis. The image is corrected for brightness variation by fitting a two-dimensional quadratic polynomial to the input picture and then, subtracting it [57]. Next, global thresholding is applied and clustered cell are separated from each other, followed by marker watershed segmentation [87]. This algorithm is repeated for the second image type and a logical AND operation is performed between the results to produce the output [55].

Another system Cellscreen - for automated non-invasive cell counts in small volume cultivation vessels - was introduced not long ago [9]. The system consists of an inverse microscope, equipped with a 10x lense, a camera, and a special application software. Initially, 96 well plate, filled with cell suspension is positioned on the motor stage. An automated procedure calibrates the position of the plate, guaranteeing that exactly the same area is analyzed. The positioning of the culture followed by an autofocus, and then image recordings are done a the base of the well. A modified version of the Cedex image is applied to the captured images extracting the number of viable and dead cells and their morphology.

Commercial software has also been developed, mainly for the pharmaceutical screening market [35]. Development of these packages has been primarily focused on mammalian cell types and cellular features needed for medical analysis. The benefits of the commercial software are reliability, usability and user support. For these reasons it has been successfully adopted in many laboratories, however, the high cost of such solutions and inaccessibility to the code limit their widespread.

To solve the task of measuring strain susceptibility from an image of DSTM device, the existing methods require significant modification. Different packages must be used at different stages of analysis, resulting in a complex workflow and an increased processing time. Thus, a new dedicated method for processing microscopy images was needed.

### 2.2.3 Algorithm for drug susceptibility testing

The developed algorithm for quantitative analyses and susceptibility assessment of a bacterial strain from a microscopy image of the DSTM device is divided into five stages: noise reduction, localization of the channel regions, cell detection, feature extraction, susceptibility, and MIC estimation.

The scheme of the algorithm is presented in the Fig. 2.7. The input image of the DSTM device channels is enhanced by applying illumination correction and denoising. Next, the areas in the image corresponding to microfluidic channels are located by identifying their borders with Probabilistic Hough Transform (PHT). After that, for each channel a cell

detection is carried out assigning a label for each pixel to be background or a part of a cell. From this information it is easy to extract a vast number of statistics and cell features. Attributes obtained for the control sample are used for calculating relative cell features. Finally, the features are assembled into feature vectors and fed into pre-trained SVM, which determines if the bacteria strain is susceptible to a particular drug concentration or not. The least concentration of the drug for which the SVM predicted susceptibility is the MIC.

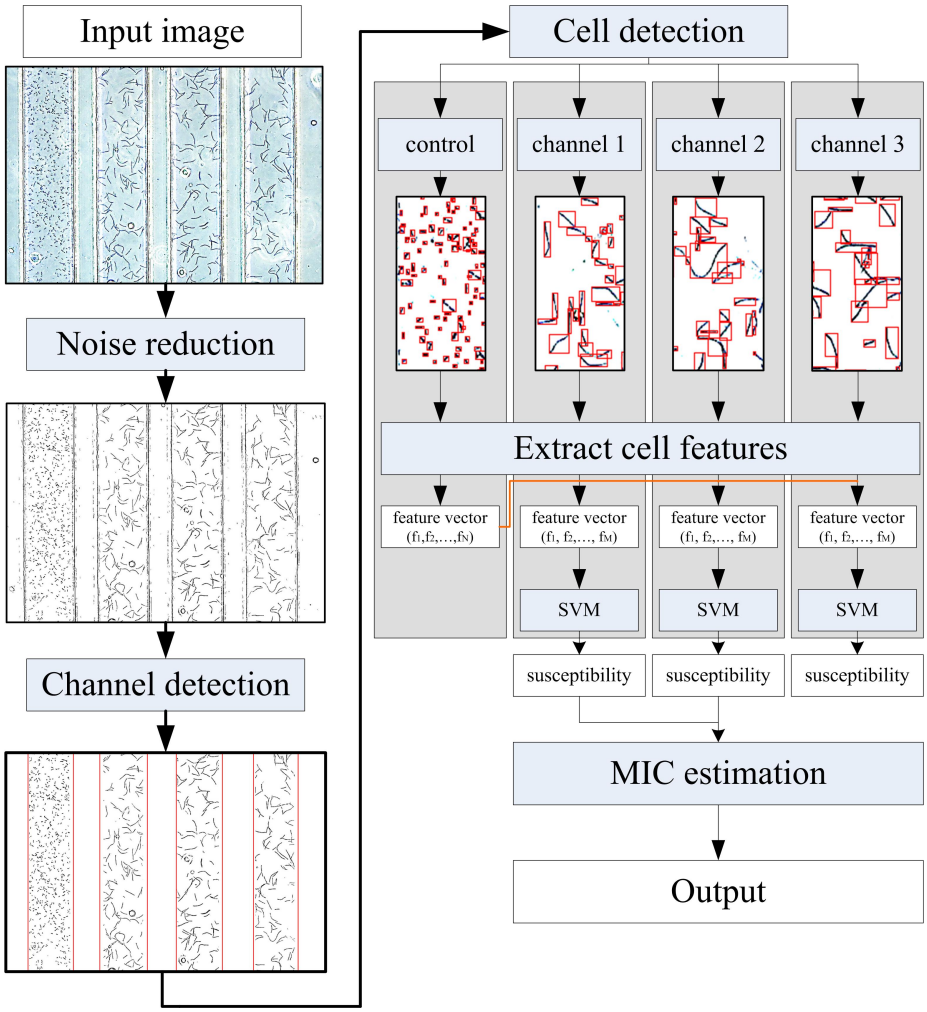


Figure 2.7: A scheme of the proposed algorithm for processing an input image of DSTM device channel to extract cell features, estimate susceptibile for each drug concentration and obtain MIC

### 2.2.4 Noise reduction and Illumination correction

The process of capturing digital images using microscopy often results in nonuniform illumination of the scene. For further correct processing of the visual data it is essential

to enhance the image by performing illumination calibration.

Since the distribution of the light intensity at the captured photograph can be assumed to have a quadratic form it can be modelled using the following function [57].

$$I_q(x, y) = a_1x^2 + a_2y^2 + a_3xy + a_4x + a_5y + a_6 \tag{2.1}$$

The approach in the illumination correction is to fit this light distribution to an input image. This fit is based on least-squares estimators. For an input $M \times N$ image $I(m, n)$ the paramters $a_i, \;\; i = 1, ..., 6$ are calculated by minimizing the merit function $\chi^2$.

$$\chi^2 = \sum_{m=1}^{M}\sum_{n=1}^{N}(I(m, n) - I_q(m, n))^2 \tag{2.2}$$

The minimum of the merit function (2.2) occurs when its derivatives with respect to all parameters $a_i$ are equal zero. This condition yields the following 6 equations.

$$\sum_{m=1}^{M}\sum_{n=1}^{N}[(I(m, n) - \sum_{j=1}^{6} a_jX_j(m, n))X_k(m, n)] = 0 \qquad k = 1, ..., 6 \tag{2.3}$$

Where $X_j = X_j(x, y)$ is the $j - th$ function from all the basis functions $X(x, y) = \{x^2, y^2, xy, x, y, 1\}$. Interchanging the order of summations the equation (2.3) can be written as the matrix equation.

$$\sum_{j=1}^{6} a_j\alpha_{kj} = \beta_k \tag{2.4}$$

Where $\alpha_{kj}$ is a $6 \times 6$ matrix and $\beta_k$ is a vector.

$$\alpha_{kj} = \sum_{m=1}^{M}\sum_{n=1}^{N} X_j(m, n)X_k(m, n) \quad \text{or equaivalently} \quad [\alpha] = A^T \cdot A \tag{2.5}$$

$$\beta_k = \sum_{m=1}^{M}\sum_{n=1}^{N} I(m, n)X_k(m, n) \quad \text{or equaivalently} \quad [\beta] = A^T \cdot b \tag{2.6}$$

The equations (2.5) and (2.6) are called normal equations of the least-squares problem. They can be solved for the vector of paramters $a_i, \;\; i = 1, ..., 6$ by LU decomposition, Choleksy decomposition, Gauss-Jordan elimination or other methods [34].

This illumination correction approach was directly applied to the input images of the DSTM device channels and its output was used in channel detection stage (see Fig. 2.8). Yet before being processed and the cell detection phase in undergoes and additional procedure - binarization.

Binarization is done by applying Otsu adaptive thresholding [87]. This method involves iterating through all possible threshold values and calculating a measure of spread

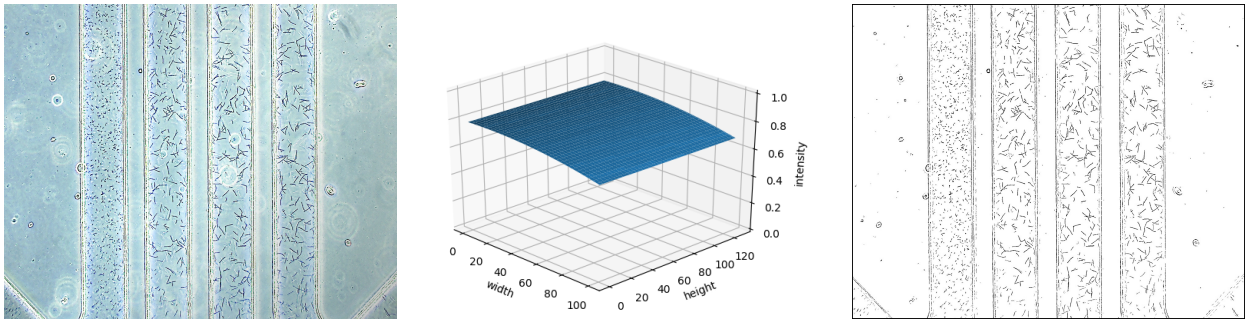


(a) (b) (c)

Figure 2.8: An example of an input image and the result of executing noise reduction step of the proposed algorithm: (a) input image; (b) fitted quadratic polynomial; (c) output

of foreground and background pixels in an attempt to find threshold $t$ which minimizes the weighted within-class variance of each type of pixels (2.7).

$$\sigma_w^2(t) = q_1(t)\sigma_1^2(t) + q_2(t)\sigma_2^2(t) \tag{2.7}$$

Where $q_1$, $q_2$ and $\sigma_1$ and $\sigma_2$ are defined with the following equations (2.8), (2.9), and (2.10).

$$q_1(t) = \sum_{i=1}^{t} P(i) \;\; \& \;\; q_2(t) = \sum_{i=t+1}^{I} P(i) \tag{2.8}$$

$$\mu_1(t) = \sum_{i=1}^{t} \frac{iP(i)}{q_1(t)} \;\; \& \;\; \mu_1(t) = \sum_{i=t+1}^{I} \frac{iP(i)}{q_2(t)} \tag{2.9}$$

$$\sigma_1^2(t) = \sum_{i=1}^{t} (i - \mu_1(t))^2 \frac{P(i)}{q_1(t)} \;\; \& \;\; \sigma_2^2(t) = \sum_{i=t+1}^{I} (i - \mu_2(t))^2 \frac{P(i)}{q_2(t)} \tag{2.10}$$

### 2.2.5 Channel detection

The next step of the algorithm is the detection of DSTM device microfluidic channels in the input image. This is done by locating left and right borders for each channel. Since, there is significant change in intensity on the border, an edge detection technique can be exploited to determine the position of each border. In the proposed algorithm Canny edge detection is applied to the output of the illumination correction step. Then, channel border candidates are located utilizing probabilistic Hough transform. Finally, additional constraints are imposed to select among all detected lines those, which represent channel borders.

The Hough Transform (HT) is a robust statistical method of detection lines and other predifined features. In order to detect straight lines $y = mx + b$ in a large set of edge

points $P = \{(x_i, y_i), i = 1, ..., M\}$, each possible line that goes through the point $x_i$ is expressed in polar coordinates.

$$\rho = x \cos\theta + y \sin\theta \tag{2.11}$$

The intersection of a large number of sinusoids in the $(\rho, \theta)$ plane corresponds to a straight line which goes through a large collinear subset of points in $P$. The standard implementation of the HT is the Duda and Hart algorithm [29] in which the $(\rho, \theta)$ plane is divided into $N_p \times N_p$ rectangular cells and represented by an accumulator array. The algorithm, first, for each line increments corresponding accumulators and then searches for maxima. Thus, it represents normal parameters of straight lines through a large number of points.

HT is a widely used and robust algorithm, however, it has two major drawbacks. First, for each nonzero pixel in the image, the parameters for the existing line and redundant ones are both accumulated. Second, the accumulator array is predefined in a heuristic way. The more accuracy needed, the higher parameter resolution should be defined.

The Probabilistic Hough Transform (PHT) approach minimizes the proportion of points that are used in the voting rule. A number of techniques to implement PHT exist. Kiryati et al. [56] showed that it is often possible to obtain results identical to those of standard HT even if only a fraction of input points is used. However, the method they described requires *a priori* knowledge of the number of points belonging to the line, which is rare in practice. It was also showed by Bergen and Shvaytser [8] that PHT can be formulated as a Monte-Carlo estimation of the HT. Nevertheless, this method requires *a priori* knowledge as well.

For the task of detecting channel borders an alternative implementation of HT, called Progressive Probabilistic Hough Transform (PPHT), described in [69]. This algorithm, unlike the above-mentioned works, minimizes the amount of computations, needed to detect lines by exploiting the difference in the fraction of votes needed to reliably detect lines with different numbers of supporting points. To minimise the computation requirements the PPHT repeatedly selects a new random point for voting. Then, after casting a vote it is tested if the point has random noise or not by sampling $m$ out of $N$ total points and calculating if any bin count exceeds the threshold of $s$ points, which would be expected from random noise. This test requires a single comparison with a threshold per bin. After detecting the line the supporting points retract their votes and then they are removed from the set of points not yet voted. The procedure continues until all points are not checked.

The output of PPHT is a set of lines, some of which represent channel borders while others are misdetections. To select only those lines that correspond to channel borders the developed algorithm imposes several additional constraints: vertical orientation of the borders, number of neighbor lines, equality of channel widths. First, all lines, that deviate from vertical orientation more than pre-defined threshold are removed. Next, lines intersecting each other are combined together to produce an average approximation. Finally, since the microfluidic channels in reality have same width, the method refines the

border candidates taking into account for each line the distance to its neighbor, and the number of lines it was combined from.

The result of channel detection step for an example input image is presented in the Figure 2.9.

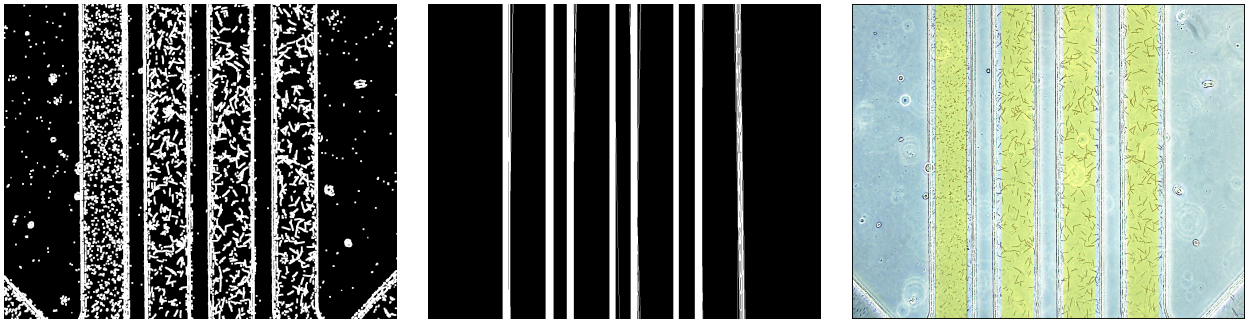

(a) (b) (c)

Figure 2.9: Images illustrating channel detection stage of the algorithm: (a) output of the Canny edge detector, applied to the result image of the illumination correction procedure; (b) lines representing channel border which were detected with the PPHT algorithm; (c) an input image with the detected channels displayed in yellow.

### 2.2.6 Cell detection

Cell detection is the most challenging step in image analysis and its accuracy determines the efficiency of the resulting cell measurements. The main challenge that has to be resolved at this step is separation of overlapped cells.

This issue arrises from the phenomena of cell filamentation – anomalous growth in which bacteria do not divide and continue to elongate. Due to three dimensional structure of the microfluidic channels, movements of the microorganisms and flow of the solution the bacteria cells are percieved as overlapped on a captured image. Existing approaches for segmentation of cells, such as watershed or level set techniques [55], [93], show poor results due to inability to distinguish where membranes of cells touch. Thus, to oppose this matter a separation algorithm modeling overlapped cells as graphs and performing splitting has been developed.

At first the algorithm extracts all conected regions using connected-component labeling method [26], [98] applying it to the binary image obtained as the result of procedures carried out at the noise reduction stage (see Section 2.2.4). Next, aim is to idenitfy in each connected region all intersections between cell candidates. To accomplish that morphological thinning is applied [42], [43], [125]. The most common way to perform this procedure is to use the method introduced by Zhang and Suen [125]. For each pixel this method checks neighbours and removes pixels if they correspond to a certain pattern. Thinning produces a skeleton representation of the original structure in which the intersection points are pixels two or more non-background neighbors. In addition to in-

tersections, points where potential cells touch are located. This is done by analyzing if smoothness, i.e. second derivative, violates the constraint, defined by a threshold constant.

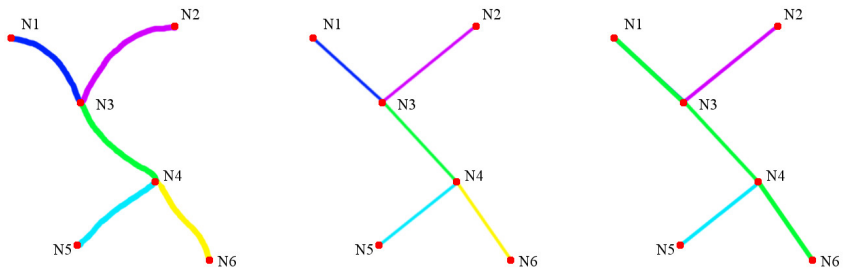


(a) (b) (c)

Figure 2.10: An illustration of steps of the cell detection procedure: (a) detection of vertices; (b) construction of the graph representation; (c) determining the longest route with satisfied smoothness constraint.

The next step is to model a cell as a graph preserving its morphological structure. Interesction, end points and touch points become nodes, while connection between these points become edges (see Fig. 2.10). All possible routes in the graph are extracted using the breadth-first search [106]. For each route, smoothness constraint is checked and if it is not satisfied the route is removed from the set. The smoothness constraint is defined as the maximum allowed angle between nodes. A set of routes with maximum number of nodes to cover the entire graph is chosen. The found routes represent individual cells. Finally, for all pixels removed at the thinning stage a corresponding cell label is assigned.

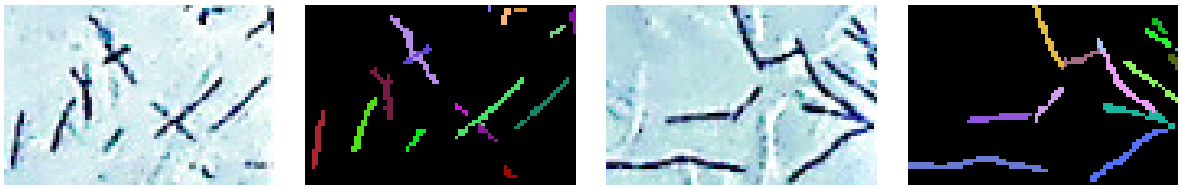

(a) (b) (c) (d)

Figure 2.11: Two close-up examples of elongated cells (a, c) and results of the cell detection stage of the algorithm (b, d) for the corresponding images.

### 2.2.7 Feature extraction

The output of the cell detection stage is a set of labeled pixels, which describes bacteria cells. From this data extracting a variety of different features to represnet changes in cell growth is a fairly straightforward task.

Cell morphology is one of the major indicators of the strain sensitivity. To represent this attribute for each cell its area and length are calculated. It has to be noted that area is

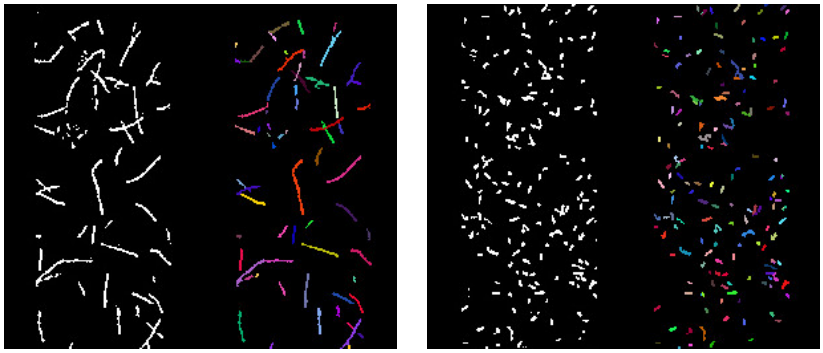

(a) (b)

Figure 2.12: Two examples of the binary image and the output of cell detection stage of the algorithm for a sensitive strain (a) and a resistant strain (b).

defined as the total number of pixels, while length is approximated as the number of pixels in the thinned representation of the cell. Statistics of these two features, mean, minimum, and maximum, as well as a 8-bin histogram of cell frequencies in relation to length are used to characterize strain growth in the presence of a particular drug concentration. In addition to shape features cell count is also added to the set of features to represent the number of living cell.

The growth rate of different bacteria strains varies significantly. Two different bacteria strains, obtained from different patients, could show completely distinct growth rates, even without the presence of a drug (see Fig. 2.13). Hence, it is not appropriate to perform comparison between samples of different strains using characteristics presented in absolute values, i.e. pixels. Thus, cell features extracted for each one of three test channels are divided by those calculated for the control channel, producing a set of relative attributes.

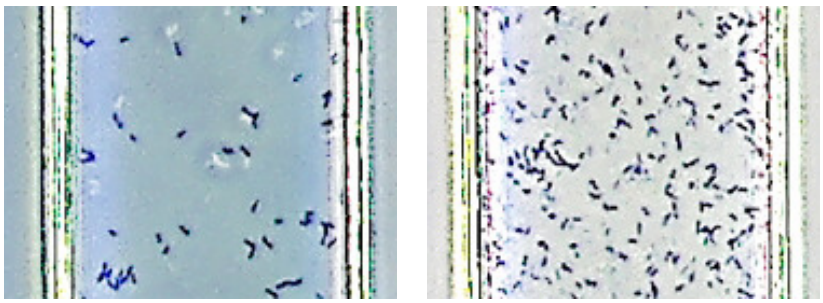

(a) (b)

Figure 2.13: Two images of channels, used as control, illustrate that different bacteria strains show dissimilar growth rates even without any presence of antimicrobial agents.

### 2.2.8 Susceptibility estimation with SVM

The prediction of susceptibility from a set of relative features for each test microfluidic channel is performed with a Support Vector Machine.

Support Vector Machine (SVM) is a widely used supervised learning technique for classification and regression [11], [116], [118]. Let set $X = \{(\vec{x_i}, y_i), i = 1, ..., N;\}$ be the training data where $\vec{x_i} \in R^d$ represents feature vectors and $y_i \in \{-1, 1\}$ are labels. SVM solves the classification problem by identifying a hyperplane, separating two classes.

$$\vec{x} \cdot \vec{w} + b = 0 \tag{2.12}$$

In equation (2.13) parameter $\vec{w}$ is normal to the hyperplane, $|b|/||w||$ is the perependicular distance from the hyperplane to the origin, and $||w||$ is the Euclidean norm of $\vec{w}$. Let $d_+$ and $d_-$ are the shortest distances from the separating hyperplane to the closest positive and negative point respectively. For the lineraly separable case SVM locates the hyperplane with the largest margin defined as $d_+ + d_-$. The method achieves that by minimizing $||w||^2$, subject to the following constraints.

$$y_i(\vec{x_i} \cdot \vec{w} + b) - 1 \geq 0 \ \ \forall i \tag{2.13}$$

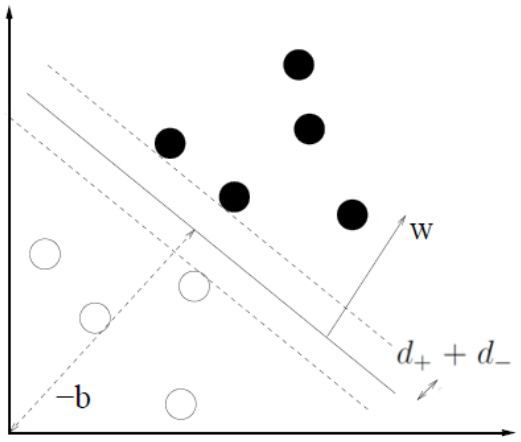


Figure 2.14: The illustration of the SVM method, that solves the classification problem by constructing a hyperplane with the larges margin between classes.

This could be done by minimizing Lagrangian, representing all inequality constraints (2.13) with respect to $\vec{w}, b$. In addition the derivatives of this Lagrangian 2.14 with respect to all the $\alpha_i$ has to be equal zero.

$$L_P = \frac{1}{2}||w||^2 - \sum_{i}^{N} \alpha_i y_i(\vec{x_i} \cdot \vec{w} + b) + \sum_{i=1} \alpha_i \tag{2.14}$$

The requirement that the gradient of $L_P$ with the repsect to $\vec{w}$ and $b$ vanish give the conditions (2.15) and (2.16).

$$\vec{w} = \sum_{i=1}^{N} \alpha_i y_i \vec{x_i} \tag{2.15}$$

$$\sum_{i=1}^{N} \alpha_i y_i = 0 \tag{2.16}$$

By substituting these conditions into the Lagrangian equation (2.14) a dual formulation of the problem cand be given: to maximize functional $L_D$ (2.17) with the respect tot $\alpha_i$, subject to constraints (2.16) and positivity of $\alpha_i$, with solution given by (2.15).

$$L_D = \sum_{i=1}^{N} \alpha_i - \frac{1}{2} \sum_{i=1}^{N} \sum_{j=1}^{N} \alpha_i \alpha_j y_i y_j \vec{x_i} \cdot \vec{x_j} \tag{2.17}$$

Since the dual maximization problem is a quadratic function of the $\alpha_i$ subject to linear constraints, it is efficiently solvable by quadratic programming algorithms.

### 2.2.9 Minimum Inhibitory Concentration

The pre-trained SVM for each feature vector representing microfluidic channel of the input image produces a binary output. Either the strain is susceptibile to the injected drug with the particular concentration or not. To obtain MIC it is simply necessary to chose minimum drug concentration to which SVM - using cell features extracted from corresponding channels - predicted susceptibility.

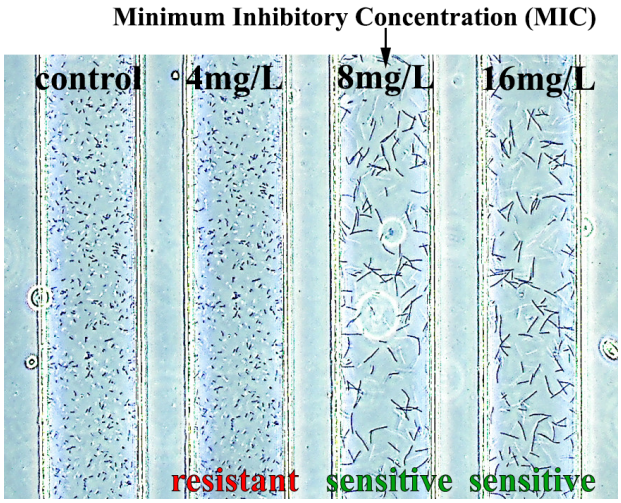


Figure 2.15: MIC is the minimum concentration of the applied drug to which the bacteria strain is susceptibile.

## 2.3 Experimental results

### 2.3.1 Dataset

The image dataset used for testing the developed algorithm was obtained with the DSTM device that was prepared by fabricating microfluidic channels (width, 100$\mu m$; height, 50 $\mu m$) in a polymer (polydimethylsiloxane - PDMS; Silpot184, Dow Corning Toray Co., Ltd., Tokyo, Japan) on a glass cover (Matsunami Glass Ind., Ltd., Osaka, Japan) using soft lithography technique [122]. The input images were captured with a USB camera, attached to a phase contrast microscope with 10-fold objective lens with JPEG compression and 1280x1024 resolution (see Fig. 2.16).

The drug pool contained five different drugs: amikacin (AMK; Nichi-Iko Pharmaceutical Co., Ltd. Toyama, Japan), ciprofloxacin (CIP; Meiji Seika Kaisha, Ltd., Tokyo, Japan), meropenem (MPM; Meiji Seika Kaisha, Ltd.), ceftazidime (CAZ; Sawai Pharmaceutical Co., Ltd, Osaka, Japan), piperacillin (PPC; TOYAMA CHEMICAL CO., LTD, Tokyo, Japan). Each one of the drugs was used in three different concentrations during the testing phase: AMK (4, 8 and 16 mg/L), CIP (1, 2 and 4 mg/L), MPM (1, 2 and 4 mg/L), CAZ (4, 8 and 16 mg/L) and PPC (4, 8 and 16 mg/L). The antimicrobial agents were dissolved in water, pre-introduced to each microfluidic channel from the outlet hole, and freeze-dried before use [71].

Strains of 101 clinically isolated specimens of *Pseudomonas aeruginosa* ATCC27853 were used in experiments. Among these 55 showed resistance to multiple drug compounds, 21 were sensitive to a single agent, and the rest were sensitive to all compounds [71]. The strains were grown overnight on Heart infusion agar and suspended in cation-adjusted MuellerHinton broth, and then were introduced with a micropipette into the DSTM devices. Next, the DSTM devices then were incubated under humid conditions (37C) for up to 3h.

The ground truth minimum inhibitory concentrations were determined for the same set of bacteria strains with the microbroth dilution method using a Dry plate Eiken (DPD2) (EIKEN Chemical Co., Ltd, Tokyo, Japan).

### 2.3.2 Channel detection accuracy

The first stage of the conducted experiments was focused on determining the accuracy of channel detection. The whole dataset provided 505 images (101 images for each one of 5 drugs), each one of them had 4 observable microfluidic channels. Thus, in total the number of channels reached 2020. Among all these channels the algorithm was not capable of correctly determining only 8 channels, which is 0.003% of the total number.

During the course of developing algorithm after careful observation of input images it was deduced that channel borders are visible as dark lines. And for major cases that observation is correct, yet in some cases due to image artifacts the borders could have higher levels of intensity, without any traces of black lines, making it impossible to correctly apply Canny edge detection, paired with PPHT (see Fig. 2.17).

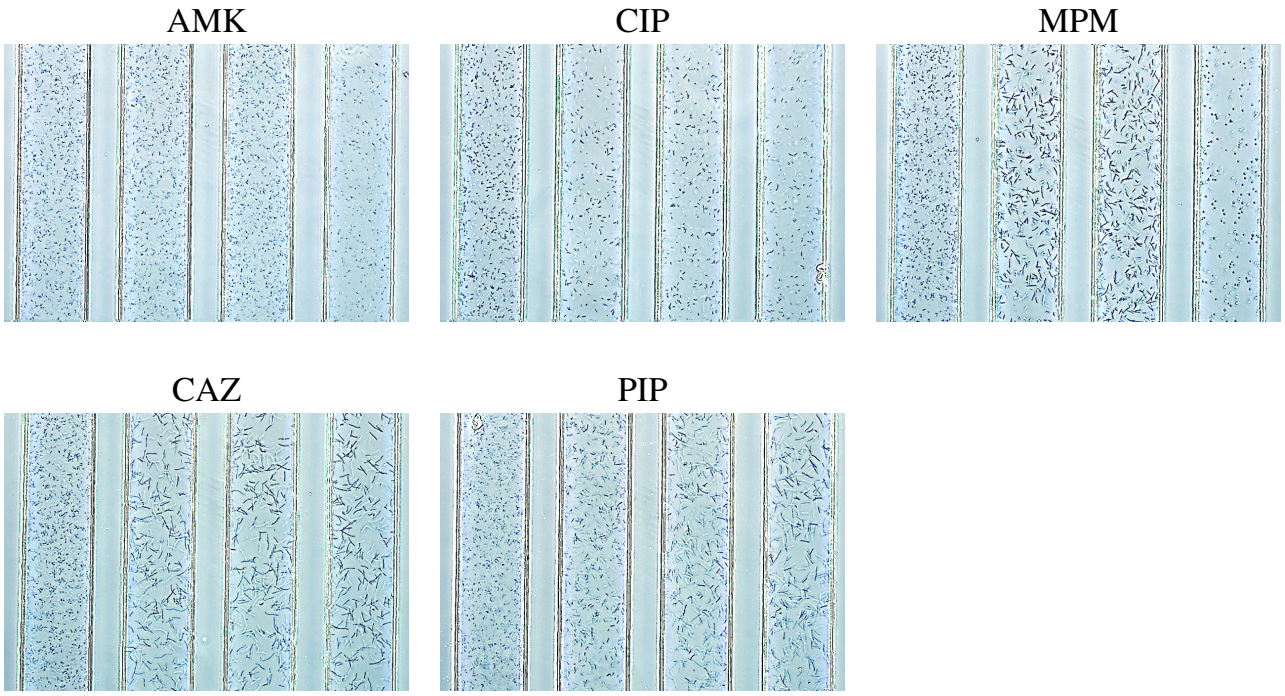


Figure 2.16: Images taken after 3h of incubation for 5 different drugs, applied to a single bacteria strain.

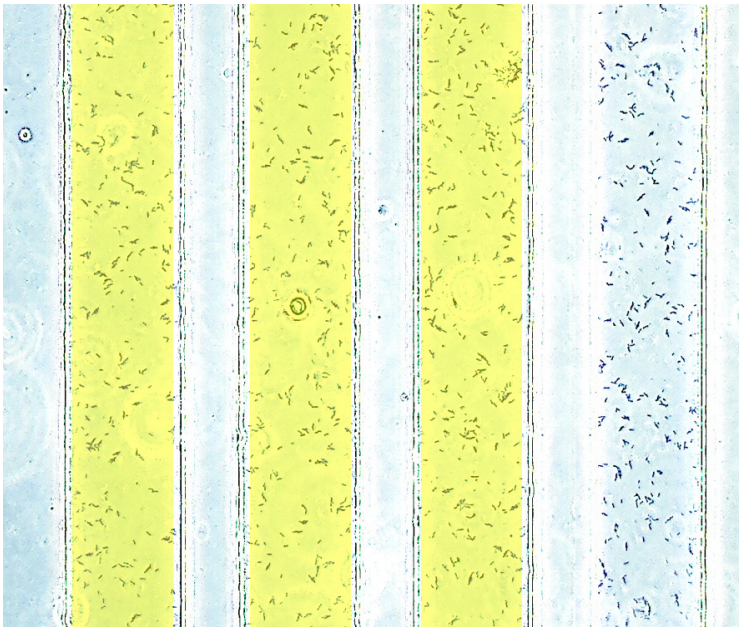

Figure 2.17: Example of a channel, which the algorithm was not able to detect correctly due to lack of dark pixels in the channel border.

### 2.3.3 Cell detection accuracy

Next step of experiments was dedicated to examining if the developed algorithm capable of correctly detecting bacteria cells. It is impossible to obtain directly ground truth pixel-based segmentation of cells that can be compared with the output of the cell detection stage of the algorithm. Manually labeling cells in all the samples was also not possible due to the sheer number of data. Therefore, to conduct estimation of cell detection accuracy the cells in 100 sample channels from 25 randomly chosen images were manually counted. Then, the obtained values were compared with those calculated by the proposed technique.

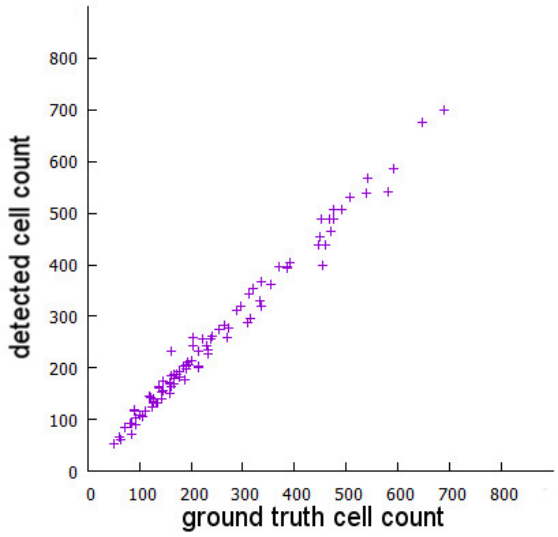


Figure 2.18: Scatter plot that represents the accuracy of cell detection with the proposed algorithm.

The Figure 2.18 represents the relationship between the number of cells identified automatically with those counted manually. The average accuracy of correctly detected cells was 93%. Careful analysis of the samples where misdetection had occurred revealed that the main cause of errors is highly overlapped elongated cells where the algorithm labels segments as individual cells.

### 2.3.4 Susceptibility estimation

Next step in evaluating the efficiency of the method was to calculate the accuracy of determining the susceptibility of bacteria strains to each drug with particular concentration. To accomplish that separate SVMs were trained for each antimicrobial agent. The entire dataset containing 303 feature vectors (3 test samples for each one of 101 images) was split into training and testing sets in the ratio 80:20 and testing was done with cross validation.

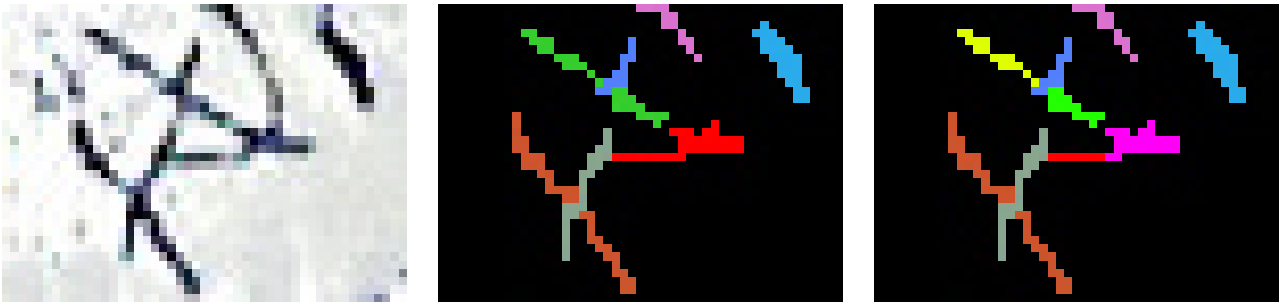

Figure 2.19: Left image displays several overlapping cells as seen in the input image. Middle image presents the ground truth separation of cells. Image on the right shows misdetections.

Several feature vectors for SVM training was combined with different cell characteristics to investigate which set of features is able to achieve the highest accuracy. The following feature sets were used: (F1) length statistics, (F2) area statistics, (F3) count and average length, (F4) count and average area, (F5) average length and area, (F6) histogram (see Table 2.1).

| | **Drug** | | | | |
|---|---|---|---|---|---|
| **Feature** | **AMK** | **CIP** | **MPM** | **CAZ** | **PPC** |
| ALL | **0.91** | **0.96** | **0.94** | **0.95** | **0.9** |
| $F_1$ | 0.81 | 0.85 | 0.9 | 0.88 | 0.89 |
| $F_2$ | 0.83 | 0.88 | 0.89 | 0.86 | 0.87 |
| $F_3$ | **0.9** | **0.96** | **0.94** | **0.94** | **0.9** |
| $F_4$ | 0.85 | 0.88 | 0.87 | 0.85 | 0.88 |
| $F_5$ | 0.78 | 0.83 | 0.87 | 0.87 | 0.89 |
| $F_6$ | 0.89 | 0.95 | 0.94 | 0.92 | 0.9 |

Table 2.1: Susceptibility estimation accuracies for feature vectors constructed from different cell characteristics

For CAZ and PPC, features indicating length (F3, F4 and F5) were more reliable characteristics for estimation, whereas for AMK and CIP it was cell count. For MPM, feature vectors indicating length or cell count were equally accurate. The average accuracy of susceptibility estimating exceeded 90%.

The figure 2.20 provides visualization of the trained SVM classifiers for the two-dimensional feature vector combined from cell count and average length for each one of five drugs.

### 2.3.5 Susceptibility estimation: 2h vs 3h incubation

For bacteriologists, it is a matter of crucial importance to determine whether a bacteria strain is susceptible to a particular concentration of an antimicrobial agent as quick as

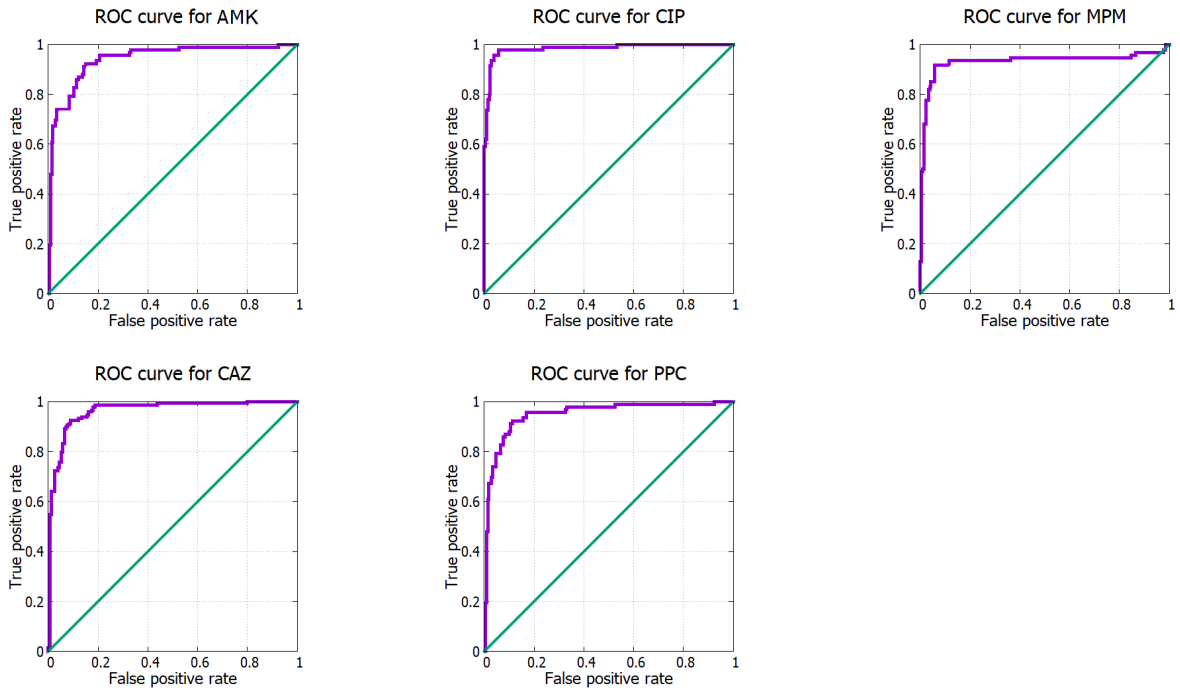


Figure 2.20: ROC curves built for each one of five antimicrobial agents: amikacin (AMK), ciprofloxacin (CIP), meropenem (MPM), ceftazidime (CAZ), piperacillin (PPC)

possible. Therefore, the next stage of experiments was dedicated to investigating how well the SVM can predict susceptibility from images taken earlier than 3h.

The same dataset of 101 strains and 5 drugs was used during this experiment, yet the input images were captured merely after 2h of incubation. The feature vectors fed into the SVM consisted of only two elements: cell count and average length.

Then, the accuracy of susceptibility estimation after 2h for each drug was compared with the one, achieved after 3h. The results of this examination is presented in Table 2.3.

| | **Drug** | | | | |
|---|---|---|---|---|---|
| **Incubation time** | **AMK** | **CIP** | **MPM** | **CAZ** | **PPC** |
| 2 h | 0.74 | 0.85 | 0.82 | 0.8 | 0.79 |
| 3 h | 0.9 | 0.96 | 0.94 | 0.94 | 0.9 |

Table 2.2: Susceptibility estimation accuracy using a feature vector, reflecting only cell count and average length, on samples incubated for 2 h or 3 h

Due to less prominent difference between cell features of the control and test samples the overall accuracy of susceptibility estimation was dramatically lower after 2 h incubation than after 3 h. The lowest value was of 74% was observed for the amikacin (AMK). The primary reason for this outcome was that the bacteria strains grown in the presence of AMK expressed lesser morphological changes in comparison to other drugs.

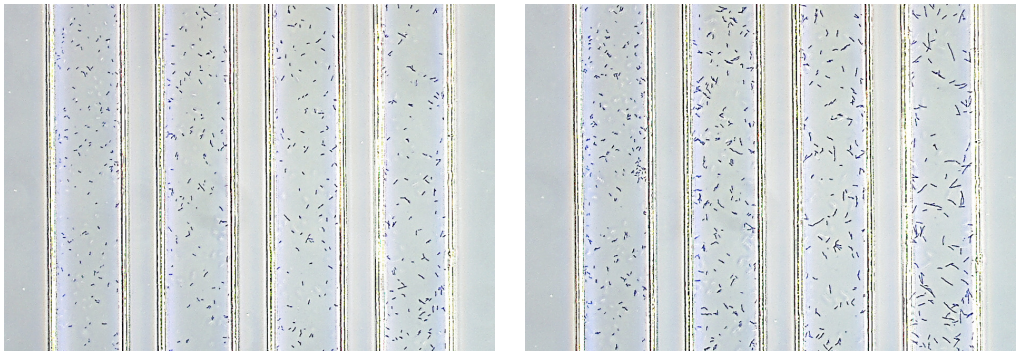

Figure 2.21: Example DSTM device microscope images taken after 2h (left) and 3h (right) of incubation.

### 2.3.6 MIC estimation accuracy

Next stage of the evaluation of the constructed algorithm was to determine the degree of correlation between predicted minimum inhibitory concentration (MIC) and the ground truth. To get the estimation of the minimum concentration for each individual bacteria strain, the susceptibility of each channel in the corresponding image was calculated with the pre-trained SVM from a feature vector, containing only cell count and average length. Then, the MIC was assigned as the minimum concentration among susceptible channels. The ground truth MIC was obtained by applying the microbroth dilution method using the same bacterial solution on the same day.

Including samples that showed a two-fold difference in the MIC, as determined by the traditional microbroth dilution method, the matching rate of the proposed method was at least 96% (see Table 2.3).

| | **Drug** | | | | |
|---|---|---|---|---|---|
| | **AMK** | **CIP** | **MPM** | **CAZ** | **PPC** |
| **Accuracy** | 0.97 | 0.99 | 0.97 | 0.97 | 0.96 |

Table 2.3: Accuracy of MIC estimation for different drugs based on a feature vector containing only cell count and average length.

### 2.3.7 SVM classifier vs human expert

Finally, the accuracy of MIC prediction with the SVM was compared with the criteria devised by a human expert, that investigated various features: length, count, the ratio of cell pixels to the background, and distribution of cells with different lengths (see Figure 2.22). The criteria were derived through trial and error to obtain the best correlation between estimated and ground truth MICs [71].

The accuracy of MIC estimation with the SVM and manually by a human expert were mostly same. The differences of not more than 1% were observed for AMK and CIP.

| | Drug | | | | |
|---|---|---|---|---|---|
| | **AMK** | **CIP** | **MPM** | **CAZ** | **PPC** |
| **SVM** | 0.97 | 0.99 | 0.97 | 0.97 | 0.96 |
| **Human** | 0.96 | 1.0 | 0.97 | 0.97 | 0.96 |

Table 2.4: MIC estimation with the trained SVM classifier vs criterie selected by a human expert

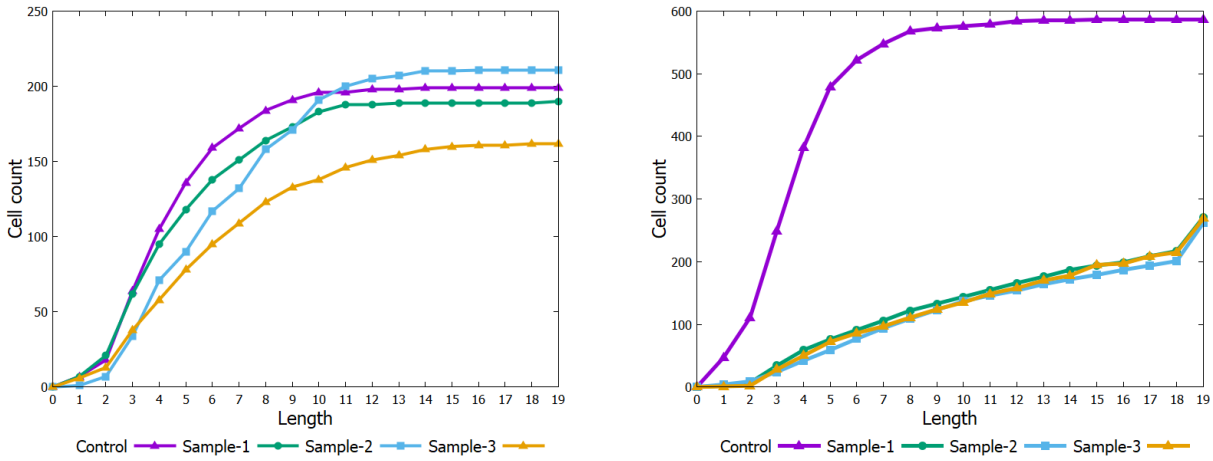


Figure 2.22: Two cumulative charts demonstrating distribution of cells with particular lengths when all three samples are resistant to injected drug (left) and sensitive (right).

## 2.4 Discussion

### 2.4.1 Comparison with existing DST methods

Previously, drug susceptibility tests required long incubation times so that the difference in growth between control and test samples become visible. Development of advanced nanotechnology methods allowed to rely on microfluidic chips and microscopy for a wide range of microbiological experiments [47], [70], [89].

Among all proposed procedures for DST, only a handfull were able to obtain results in less than 4h. For example, Choi J. et al. [51], [52] described a method involving microfluidic agarose channel chip for MIC acquisition by analyzing alterations in bacterial number and size occurred in response to drugs. The method required a complicated process of setting up a 96-well type unique plate and conducting observations where images of the plate had to be taken one by one at a certain time interval. Many other methods use microfluidic chips and measure susceptibility by assessing time-lapse images [18], [72], [77]. Most notable, Price et al. [92] using an automated microscopy system analyzed susceptibility of *Staphylococcus aureus* obtaining results in 2-4h. The suggested approach was not designed to assay multiple strains simultaneously and required 2h preincubation to get logarithmically growing cells. The system has been extended towards rapid

identification and has been applied in clinical environment [28], [73].

The key factor that contributed to the rapidity of susceptibility estimation with the DSTM device is the introduction of a microscope. Under a microscope the damaged bacteria cells treated by antimicrobial agents could be easily visualized and studied. In comparison to other methods, to obtain visual information with the DSTM device requires less than 4 hours: 10min to set-up and 3h of incubation.

The algorithm developed for automatic cell detection facilitates the analysis of bacteria cells, and capable of processing input images within 2 minutes. The advantage of the automatization is not only the speed of result acquisition but also the accuracy of cell detection, susceptibility estimation, and MIC prediction, that was proved with the conducted experiments to be similar to a highly skilled expert.

Probabilistic hough transform allowed to provide rather a high degree of invariance to rotation of channels seen in the input images and the separation technique proved to be useful in cell detection procedure. Although SVM is not a complex machine learning method it showed its efficiency for binary classification of susceptible and resistant strains from feature vectors that contained even only 2 characteristics: length and count.

The implementation of the algorithm as a stand-alone software tool was deemed useful to bacteriologist in daily research, since it provided an easy to use graphical interface and functionality to extract cell features for more detailed analysis.

Currently, the DST procedure using DSTM device is undergoing clinical trials in Japan. It is planned to expand the range of bacteria types for which the method can be applied. The implementation of the developed automatic algorithm for susceptibility testing will be supplied with the device. When this technology is put into practical use, susceptibility testing will elevate the need for expensive equipment providing low cost, simple, accurate and rapid tool.

### 2.4.2 Time lapse analysis

There are different approaches towards increasing the accuracy of the developed algorithm. One of them involves incorporating cell features extracted from time-lapse images of the DSTM device (see Fig. 2.23).

In the beginning of incubation, when an antimicrobial agent has been just introduced into microfluidic channels of the DSTM device there is no significant difference between cells in control and test channels. Gradually, over time, the morphology of cells and the count of alive bacteria start to change and alterations in a strain, susceptible to a particular drug concentration become more prominent (see Fig. 2.24).

To increase the accuracy of susceptibility estimation features can be extracted from each individual image separately, then combined into a feature vector and used as an input for the SVM or other machine learning method. Another wait to exploit the time-lapse data is to attempt to predict susceptibility earlier than 3h. This could be done either by approximating the value of desired features at 3h with linear or quadratic regression or by directly exploiting obtained features.

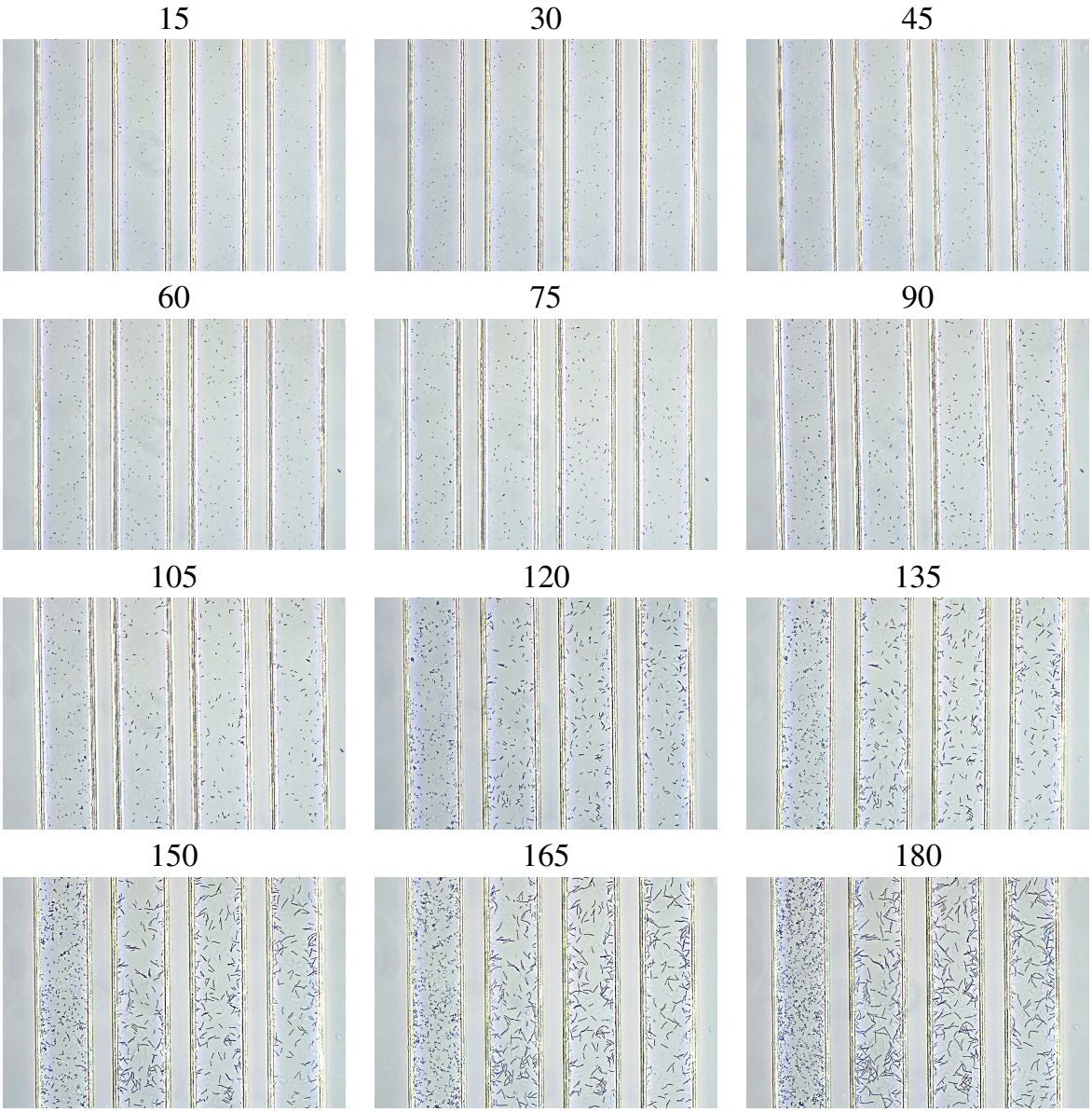


Figure 2.23: Time-lapse sequence images with CAZ injected into test channels. Each image from top left to bottom right was taken with a 15 minute interval. The first image was taken after 15 minutes from the beginning of incubation, and the last - after 3 hours.

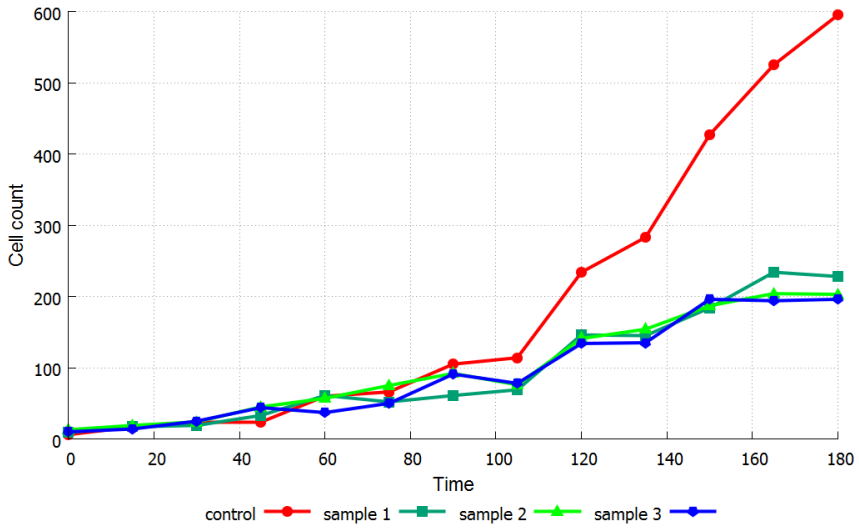


Figure 2.24: Changes of cell count through time from the beginning of the incubation till 3h for a bacteria strain, grown in the presence of

# Chapter 3

# Automatic embryo segmentation

## 3.1 Introduction

### 3.1.1 Cell analysis in embryology

Embryology is a wide field of study that includes investigation of internal mechanisms of a variety of processes such as cellular differentiation, morphogenesis, metamorphosis, tissue regeneration, and many others that occur during development of an organism. The early stages of embryo growth, from fertilization to implantation, are of particular interest to the medical community, since during this time frame the core structure of the future being is established and any flaws in internal functioning directly affect the health of the organism.

To detect disorders in the embryo during its development a pre-implantation genetic diagnosis is performed. This procedure involves genetic profiling of embryos prior implantation to assess its quality and estimate pregnancy rate. In general, profiling for prediction pregnancy rates is focused mainly on visual profiles and short-term biomarkers including expression of RNA and proteins, while profiling for health prediction puts more focus on the genome analysis.

The evaluation of the embryo quality is often done through observations of cell morphology with a microscope at certain time points and calculating the score using a morphological scoring system. This approach has shown to significantly improve pregnancy rates.

Advances in molecular biology and microscopy provided new insights into internal processes occurring at early stages of embryo development. After fertilization, a series of cleavage divisions occur producing identical cells - blastomeres. Blastomeres are undifferentiated cells, they are not yet committed to becoming any particular type of differentiated cells, thus have potential to give rise to any cell of the body that is depleted as they transform to become part of the complex tissue. Pluripotent blastomeres extracted from an embryo are called embryonic stem cells. Embryonic stem cells can continue to proliferate and replicate themselves indefinitely and still maintain the developmental potential to form any cell type of the body, promising an essentially unlimited supply of specific cell types for basic research and for transplantation.

Cultivation of embryonic stem cells is a challenging task, and, although a significant

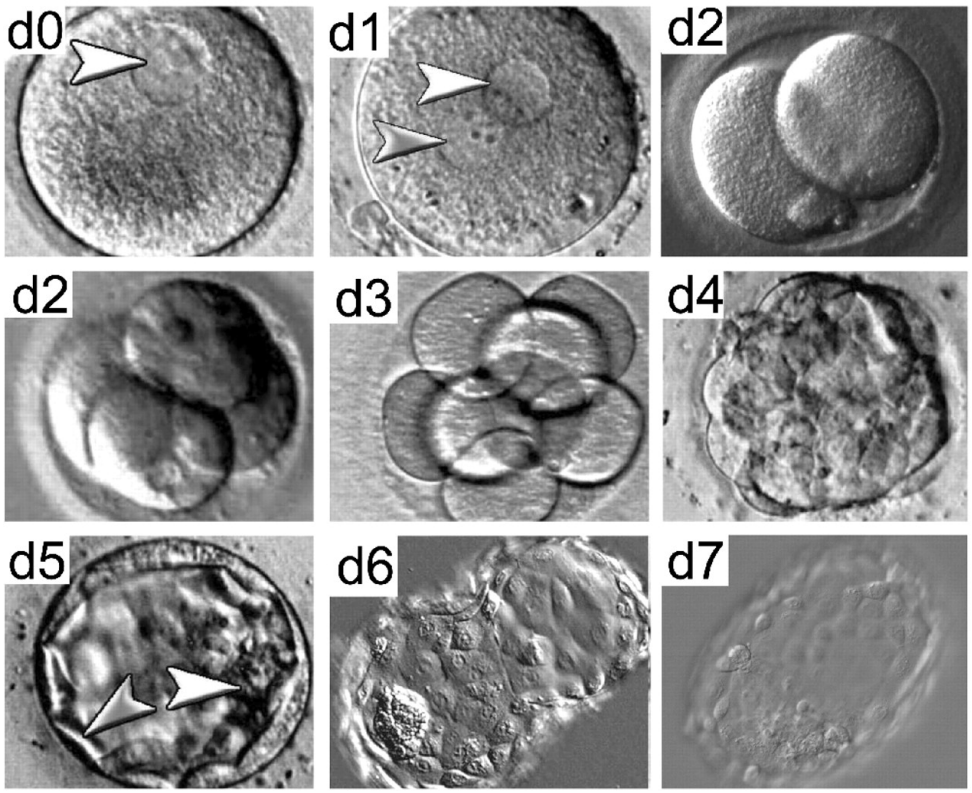


Figure 3.1: Phase-contrast images of human embryo development from day 0 to day 7. Following fertilization, embryos undergo a series of mitotic cell divisions forming morula at day 4. A fluid-filled structure composed of an inner cell mass called blastocyst forms at day 5. [80]

progress was achieved in the field of regenerative medicine, a number of difficulties remain. Primarily the existing models do not fully describe factors contributing to cell specialization, limiting the type of cells that could be grown from stem cells.

### 3.1.2 Embryo development and cell specialization

The development of the pre-implantation embryo starts from a single fertilized cell, the zygote. The first division of the zygote usually occurs within 24 hours after ovulation and produces two cells, known as blastomeres, that contain a full copy of the new embryo genome. Subsequently, a series of mitotic divisions take place, yet the volume of the embryo remains constant, while the newly formed blastomeres become smaller and smaller with each division [7], [80], [124]. When the number of cells reaches 16 the embryo enters the morula stage, during which identical blastomeres start to differentiate. This step in embryo growth is known as compaction (see Fig. 3.1) [80].

The step that follows morula compaction is known as blastulation phase, during which the embryo transforms into a cluster of cells called blastocyst. The blastocyst has a spher-

ical formation with a cavity inside it. At this stage embryo is organized into three distinct cell lineages and cell fate at this point has been already determined [97], [7].

Understanding the mechanism behind the cell specialization process in the preimplantation embryo has been complicated by the flexibility of embryo development. Experiments, where the blastomeres are removed or rearranged manually or cells from two different embryos are combined together to produce a chimaera, demonstrated ability of cells to adapt in response to contextual changes [7], [110], [111].

A number of hypotheses have been proposed to explain the process that drives cells to commit to a distinctive line. Early hypotheses were based on assumptions that development of an embryo was driven by random processes, where cell contributed equally to any type of lineage. However, more recent time-lapse imaging studies suggest that a variety morphological characteristic - volume, shape and relative positions of blastomeres - play a significant role in determining cell fate [44], [83], [97], [112], [121]. Despite significant progress in understanding the process of cell specification there are other aspects that also contribute to the determination of the resulting cell [24], [108].

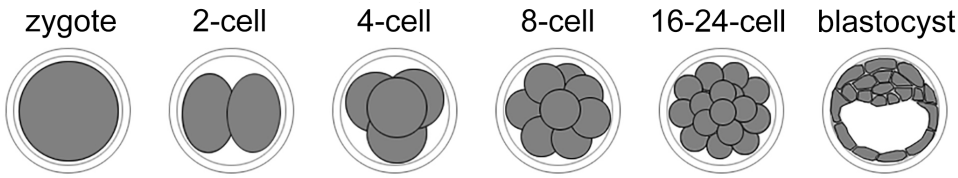


Figure 3.2: Overview of the pre-implantation development of a mouse embryo during which a fertilized egg divides into increasingly smaller cells resulting in the formation of the blastocyst.

Uncovering all the mechanisms, underlying the specification of individual cells and establishing a complete model, requires quantitative analyses of various blastomere characteristics. They can be obtained without a considerable effort if segmentation into individual cells is performed. A number of methods to automate this labor-intensive procedure have been developed over the past decade.

### 3.1.3 Methods for blastomere segmentation

Embryos are commonly imaged by means of phase contrast technique called Hoffman Modulation Contrast (HMC). It detects optical gradients and converts them into variations of light. Obtained HMC images display a transparent embryo with a side-lit appearance (see Fig. 3.3).

Singh et al. [105] presented a segmentation algorithm for processing a single HMC image for estimating embryo viability for fertility. The algorithm successfully segments up to 4 blastomeres, applying isoperimetric graph partitioning, followed by region merging which uses length, vesselness, and entropy of the borders between regions. To estimate shape, least-squared fitting of an ellipsoidal model is used.

Figure 3.3: A 4-cell embryo captured with the Hoffman Modulation Contrast (HMC) technique.

In order to perform 3D morphology measurements and modeling of an embryo, HMC images are captured at different focus levels. Resulting set of slice images is called a Z-stack. Guisti et al. [37] presented a graphcut-like global energy minimization approach for segmenting a Z-stack of HMC images and extracting 3D morphology characteristics. Other approach was introduced by Pederson et al. [88]. It applies a general multiphase variational level set with manually extracted contours to determine relative positions of blastomeres.

Graphcut-based algorithms, being very versatile, showed efficiency in segmenting each individual cell nuclei in histopathology images and tissue samples of higher organisms [3]. The watershed approaches described in [33] [84] [85] [119] were also able to successfully detect nuclei in tissue or cell cultures. Segmentation by gradient vector flow tracking was capable of producing accurate results, however it is sensitive to object texture [58] [64].

Tian et al. [115] proposed an approached based on least square curve fitting apllying it to single phase contrast image to detect blastomeres. This method combines edge detection, removing of multiple connected ponts and mophology operations to obtain part of cell edges. Then least saure circle fitting is used to detect blastomeres. Experiments, showed efficiency of the developed technique on a dataset contatining 381 embryo microscopic images obtained from eight-cell period (see Fig. 3.4).

Thick 3D topology of blastomeres, partial or full occlusions, varying defocus of HMC imaging technique, all these issues complicate the cell segmentation process[115]. Therefore, for the stages of embryo development with more than 4 cells the accuracy and efficiency of existing methods decreases, highlighting the necessity of different approaches for solving the segmentation task for these embryo stages. The choice of other than HMC imaging technique can simplify such endeavours.

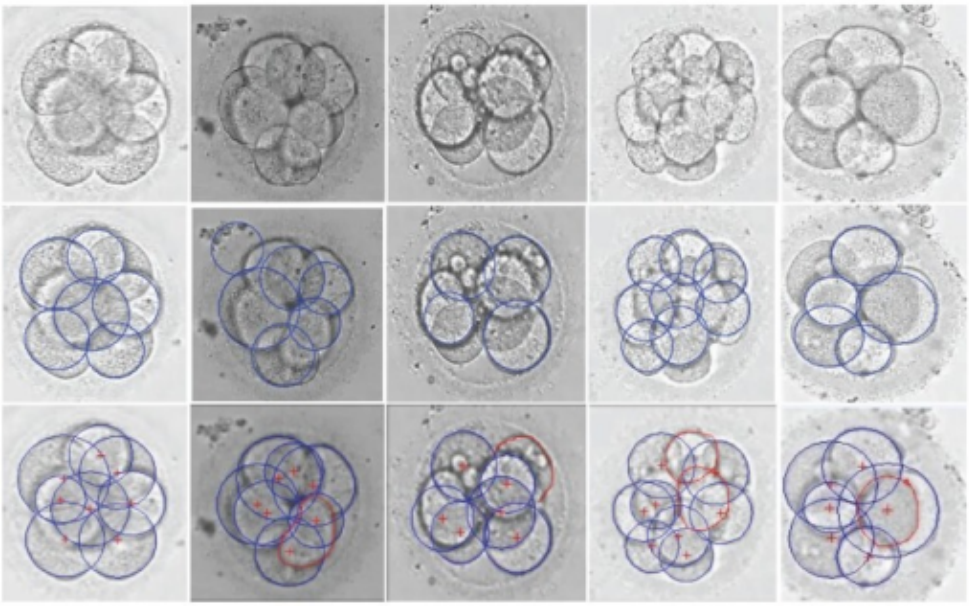

Figure 3.4: Results of blastomere detection for Hough transform-based method (middle row) and LSCF (bottom row) [115].

### 3.1.4 Fluorescence microscopy

Embryonic development is a dynamic three-dimensional process of complex cellular interactions, which are highly regulated spatially and temporally. Investigation of these interactions requires time-lapse visualization of the living embryo during the course of its growth. For high-resolution visualization of development progression genetically encoded fluorescent protein (FP) reportes have been most prominent, because of their high signal-to-noise ratio, minimal toxicity, and ease of use [79], [82],[123]. FPs can be not only used natively but also fused to any protein of interest to provide subcellular segmentation [81].

In order to visualize FP reporters different techniques have been proposed: wide-field fluorescence microscopy for observing whole embryos, confocal microscopy that allows visualize an embryo at subcellular and spatio-temporal resolution, and light sheet fluorscence microscopy, that utilizes plane of light to optically section and view tissues with subcellular resolution.

Unlike segmentation an embryo from HMC images, techniques that provided similar output for fluorscence microscopy images has not been well studied. Nethertheless a number of algorithms for general cell segmentation in fluorescence images have been developed [30], [36], [65]. Dufour et. al [30] proposed a method, based on multiple active surfaces, for automatic segmentation and tracking fluorescent cells in 3D microscopy. The algorithm is able to process multiple cells, even if they touch, divide or move. Improved version of this method, in terms of tracking precision and computational time, was introduced by Dzyubachyk et. al [31]. Xinghua et al. [65] developed at tool designed to

provide quantitative cells measurements in fluorescent intensity 2D and 3D image data. The main algorithm consists of a detection module to identify each nucleus, a segmentation module that propagates assigned labels to the entire body of the respective nucleus, and a classification module identifying different types of cells.

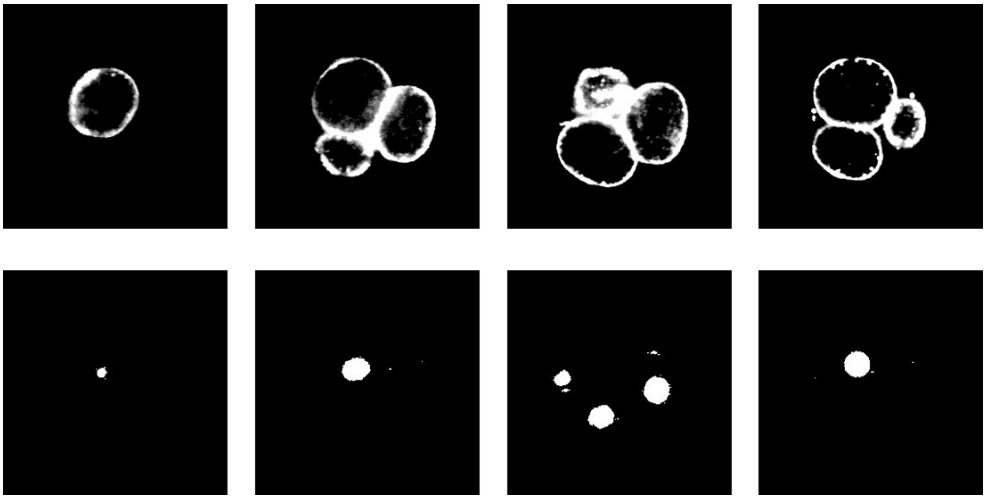

Figure 3.5: Cross sections images of a 4 cell embryo nuclei and membranes. To mark nuclei and membranes H2B-mCherry and mG proteins were used.

### 3.1.5 Embryo segmentation from fluorescence images

The solution of the cell segmentation problem presented in this study was done for the embryos that were obtained by crossing female H2B-mCherry mice with male mG mice making embryo membranes and nuclei visible [79].

As a result the input data consisted of two Z-stacks of 3D fluorescence microscopy images: one stack for cell nuclei and another one for membranes (see Fig. 3.6). The two sets of FP data, though not perfect, represent well borders of cells and the regions of nuclei. Observing the input images it is also possible to conclude that the difficulty arises due to areas of low intensity in parts of membrane and to distinguish the location where a membrane of one cell touches the other one, since there is no visible separation.

Inspired by the results of applying level set based techniques for segmentation and tracking cell, presented in works of Dzyubachyk et. al [31] and Dufour et. al [30], it was decided to design and implement a new level set approach. The segmentation task is formulated as the detection of inner regions for each individual cell as well as localizing the whole volume, occupied by membranes. Membranes, corresponding to individual cells can be afterwards acquired from the solution by locating surfaces equidistant from inner cell region boundaries with the distance transform [40].

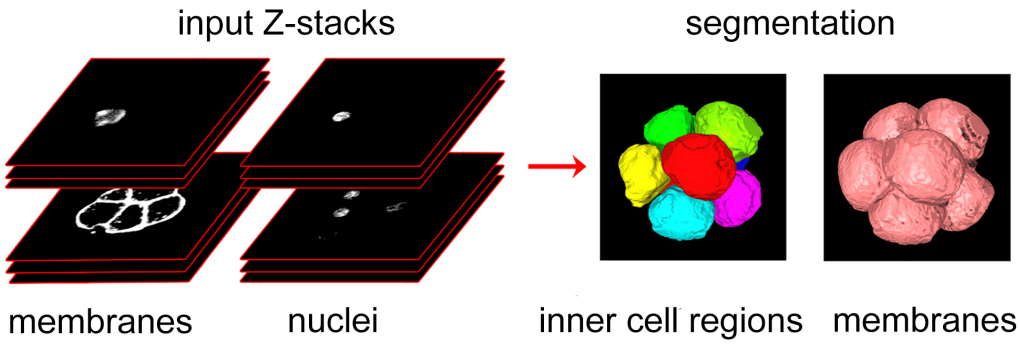


Figure 3.6: To perform segmentation of an embryo 3D level set method is applied to two Z-stacks of fluorescence microscopy images. One of the Z-stacks composed of images displaying cell membranes, while the other one contains visual information about cell nuclei positions.

## 3.2 Method: 3D Level Set

### 3.2.1 Segmentation methods

There are numerous ways to approach the task of image segmentation. Learning based algorithms are capable of achieving high segmentation accuracy, yet they require a considerable amount of input data to train on. Filtering techniques such as the Canny edge detector [12] rely only on local information and cannot guarantee continuous closed edge contours. Region growing and merging methods able to test if the area inside the segmented region satisfies a condition, yet they generate irregular boundaries and produce small holes [61]. Snake [53] and Balloon [20] methods require good initial estimation of the region boundaries and use edge cues to carry out segmentation, however, they lack a meaningful probabilistic interpretation and global conditions. Finally, optimization techniques based on energy functions or Bayesian criteria involve the usage of global criteria for which solving a minimization task is difficult.

A trade-off between local and global criteria is the level set method [2], [86]. It performs evolution by fitting statistical models to intensity, color or texture with each of the separated regions, making it far less sensitive to noise and to varying initialization. The other advantage of the level set method is its ability to handle complex morphology and topological changes automatically. However, the major drawback of the method is that solving the defined partial differential equation (PDE) is often computationally expensive. This issue was overcome by limiting the region where computation is performed [60] or totally avoiding solving the PDE [104]. The second method, in particular, was able to increase processing speed dramatically.

Efficiency in solving not only two dimensional, but three dimensional segmentation tasks [16], the simplicity of defining conditions of region boundaries, speed of existing implementations - all these factors contributed in the choice of the level set algorithm for

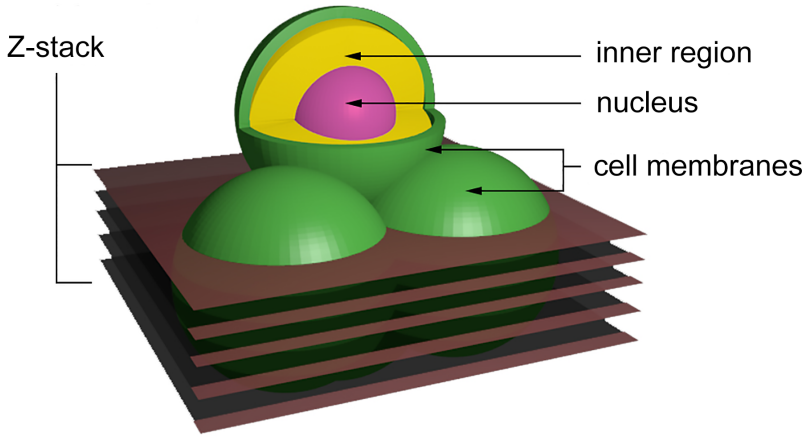


Figure 3.7: A 3D model of a 4 cell embryo with labelled elements: membrane, nucleus, inner cell region.

the embryo segmentation task from fluorescence images.

Embryos in our study have a 3D structure similar to the one shown in Fig. 3.7. They consist of cells, each of which has its own nuclei and membrane that separates the inner region from the external environment. The cell membranes are surfaces without ruptures or gaps, yet there is a likelihood that their representation in the images of the input Z-stack can have areas of low intensity, seen as holes, caused by uneven distribution of fluorescent proteins. To estimate cell membranes correctly, instead of directly attempting to locate each one of them individually the developed algorithm performs segmentation into inner cell regions and the whole region occupied by membranes. For each type of object to segment, a separate level set energy function as a differential equation was defined that penalizes overlapping with other segments, forces membrane to wrap around inner regions, and specifies that inner cell boundary is where intensity changes significantly.

### 3.2.2 3D level set segmentation

The level set method was introduced in [25], then extended in [86] to track moving interfaces for various problems in fluid dynamics. Later it was successfully applied to perform segmentation in computer vision [23]. The central idea behind this method is to evolve the boundary surface $S$ in the domain $\Omega \in R^3$ from some initialization in direction of negative energy gradient with the gradient descent procedure presented in the equation 3.1.

$$\frac{\partial S}{\partial t} = -\frac{E(S)}{S} = F \cdot n \tag{3.1}$$

The boundary $S$ following the geometric active contour model is defined implicitly as a zero level surface of a time-dependent embedding function $\phi$ (3.2).

$$S(t) = \{(x, y, z) \in \Omega | \phi(x, y, z, t) = 0\} \tag{3.2}$$

Since $\phi(S(t), (t)) = 0$, the total time derivative of $\phi$ at the boundary must vanish, giving the following equation:

$$\frac{d}{dt}\phi(S(t), t) = \nabla\phi\frac{\partial S}{\partial t} + \frac{\partial \phi}{\partial t} = \nabla\phi F \cdot n + \frac{\partial \phi}{\partial t} = 0 \tag{3.3}$$

Next by inserting the definition of the normal $n = \frac{\nabla\phi}{|\nabla\phi|}$ in the above equation the evolution equation for $\phi$ is obtained.

$$\frac{\partial \phi}{\partial t} = -|\nabla\phi|F \tag{3.4}$$

On the other hand, equation 3.1 is possible to redefine on the space of level set functions using the variational principle, deriving the Euler-Lagrange gradient descent equation for minimizing the energy functional $E(\phi)$.

$$\frac{\partial \phi}{\partial t} = -\frac{\partial E(\phi)}{\partial \phi} \tag{3.5}$$

Combining equations 3.4 and 3.5 the canonical form of the level set equation for segmentation is obtained.

$$\frac{\partial \phi}{\partial t} = -\frac{\partial E(\phi)}{\partial \phi} = -F|\nabla\phi| \tag{3.6}$$

Following the approach for identifying multiple segmentation regions [10], [67], individual level set functions $\phi_i$ are defined for each of $N$ inner cell region boundaries and one $\psi$ is set to describe the surface of the membranes, all of which are evolved simultaneously.

### 3.2.3 Energy functions

The choice of the energy function $E(\phi)$ is important, since it determines the accuracy and robustness of the level set method. In the developed approach individual energies $E_{inner}(\phi_i)$ and $E_{membrane}(\psi)$ were constructed for the two types of level set functions $\phi_i$ and $\psi$ respectively.

**Inner region energy**
The inner region energy $E_{inner}(\phi_i)$ is designed to describe the morphology of the inner cell region boundary. It is a weighted sum of three terms.

$$E_{inner}(\phi_i) = w_1 E_{edge}(\phi_i) + w_2 E_{nucleus}(\phi_i) + w_3 E_{overlap}(\phi_i) \tag{3.7}$$

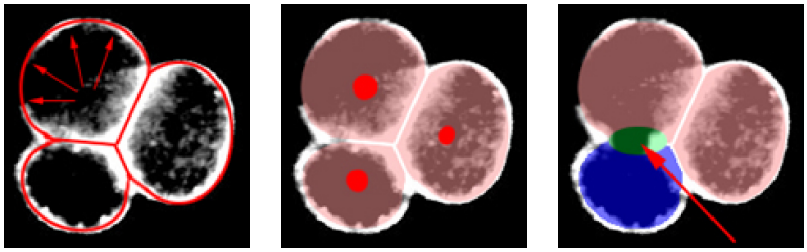

$E_{edge}(\phi_i)$ $E_{nucleus}(\phi_i)$ $E_{overlap}(\phi_i)$

Figure 3.8: Illustrations of the inner region energy terms: $E_{edge}(\phi_i)$ forces the detected inner region boundary to be closer to membrane; $E_{nucleus}(\phi_i)$ includes nuclei inside the cell regions; $E_{overlap}(\phi_i)$ prevents overlap.

The edge energy $E_{edge}(\phi_i)$ measures how well the surface $S_i$ matches the boundary of the $i-th$ cell inner region. It is defined following the approach of geodesic active contours [15], [38].

$$E_{edge}(\phi_i) = \iint_{S_i} e(x,y,z)\, ds \tag{3.8}$$

In the equation above, function $e(x,y,z)$ is the edgeness metric. It can be defined with a number of methods, however, for any definition, the function must be zero at the boundary surface of a segmented object and take large values elsewhere. In the proposed approach the edgeness metric was specified as the Euclidean distance from each point of the detected surface $S_i$ to the cell membranes displayed in fluorescence images.

The energy $E_{nucleus}(\phi_i)$ characterizes the position of the nucleus, forcing the inner region to contain nuclei inside it. Since the optimal partition $P(\Omega)$ of the domain $\Omega \in R^3$ can be obtained by computing the *a posteriori* probability $p(P(\Omega)|I)$. It is possible to describe separate image-based and geometric cues in conditional probabilisty by applying the Bayes rule [23].

$$p(P(\Omega)|I) \propto p(I|P(\Omega))p(P(\Omega)) \tag{3.9}$$

Defining geometric prior with no restrictions on surface area an image prior the previous equation can be presented in the following form.

$$E_{nucleus}(\phi_i) = -\iiint_{Q_i} \log p(Q_i|I(\vec{x}))dx\, dy\, dz - \iiint_{Q_0} \log p(Q_0|I(\vec{x}))\, dx\, dy\, dz \tag{3.10}$$

The $I(\vec{x}) = I(x,y,z)$ is the intensity of the pixel $(x,y)$ in the $z-th$ cross section of the nuclei z-stack. The $Q_i$ denotes the region occupied by the $i-th$ nucleus, while the $Q_0$ is the background. The terms $\log p(Q_i|I(\vec{x}))$ and $\log p(Q_0|I(\vec{x}))$ represent logarithm of posterior probabilities of a pixel $(x,y,z)$ to belong to the inner cell region or background, depending on its intensity $I(\vec{x})$.

To penalize the overlapping of the cell regions the $E(\phi_i)_{overlap}$ energy was constructed. This energy simply achieves its minimum when the none of pairs of cells $(i, j), j \neq i$ has a shared volumes. It is defined with the help of Heaviside functions, $H(-\phi_i(\vec{x}))$ and $H(-\phi_j(\vec{x}))$, that are zero outside cell region and one inside.

$$E_{overlap}(\phi_i) = \sum_{\substack{j=1 \\ j \neq i}} \iiint_{\Omega_i} H(-\phi_i(\vec{x}))H(-\phi_j(\vec{x}))\, dx\, dy\, dz \tag{3.11}$$

**Membranes region energy**

The surface boundaries of the all individual cell membranes combined together are specified by the energy $E_{membrane}(\psi)$. It consists of three terms: one that specifies occupied volume that depends on the intensity of voxels in fluorescence images of membranes, other penalizes overlapping with inner cell regions and the final one, that prevents occurring tearing in the surface by attempting to cover inner cell regions.

$$E_{membrane}(\psi) = v_1 E_{volume}(\psi) + v_2 E_{overlap}(\psi) + v_3 E_{inclusion}(\psi) \tag{3.12}$$

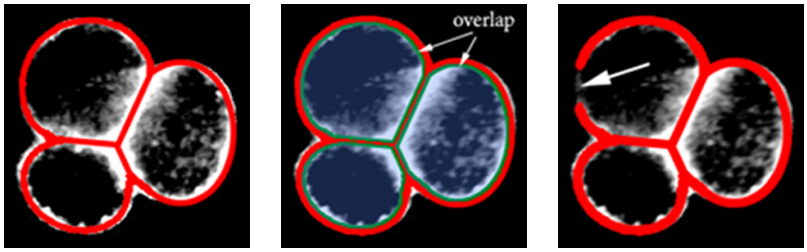


$E_{volume}(\psi)$ $E_{overlap}(\psi)$ $E_{inclusion}(\psi)$

Figure 3.9: Illustrations of the membrane energy terms: $E_{volume}(\psi)$ determines membrane location depending on intensity; $E_{overlap}(\psi)$ prevents overlap with inner regions; $E_{inclusion}(\psi)$ fills the gaps in the membrane.

The primary energy term to characterize the membranes volume is the energy $E_{volume}(\psi)$. It is defined with the help of the Bayesian region-competition framework [23], [127] and represents the joint posterior probability that each pixel $(x, y)$ in cross section $z$ belongs to membranes.

$$E_{volume}(\psi) = -\iiint_{\Omega_1} \log p(\Omega_1|J(\vec{x}))\, dx\, dy\, dz - -\iiint_{\Omega_0} \log p(\Omega_0|J(\vec{x}))\, dx\, dy\, dz \tag{3.13}$$

The components $\Omega_1$ and $\Omega_0$ correspond to membranes region and the background respectively. The $J(\vec{x}) = J(x, y, z)$ is the intensity of the membrane pixel $(x, y, z)$.

The energy function $E_{overlap}(\psi)$ is constructed similar to $E_{overlap}(\phi_i)$ (3.11) penalizes the membrane overlap with cell inner regions.

$$E_{overlap}(\psi) = \sum_{i=1} \iiint_{\Omega_1} H(-\psi(\vec{x}))H(-\phi_i(\vec{x}))\,dx\,dy\,dz \tag{3.14}$$

The fluorescent proteins mark cell membranes nonuniformly, which makes some images display nonexistent holes in membrane surface. To overcome this issue and restore the correct structure of the embryo the term $E_{inclusion}(\psi)$ was designed to force the membrane to cover inner cell region.

$$E_{inclusion}(\psi) = \iiint_{\Omega_1} \frac{1}{1 + e^{(k*(d(x,y,z)-D))}}\,dx\,dy\,dz \tag{3.15}$$

The function $d(x, y, z)$ measures the distance from the point $(x, y, z)$ to the boundary of the inner cell region. The constant $D$ sets the maximum allowed distance from the membrane to the inner cell regions.

### 3.2.4 Level set evolving equations

To summarize all the above, for the segmentation problem defined as locating inner cell regions and membranes it is necessary to solve $N + 1$ PDEs, where $N$ is the number of cells in the embryo.

$$\frac{\partial \phi_i}{\partial t} = -\frac{\partial E_{inner}(\phi_i)}{\partial \phi_i} = -F_{inner}|\nabla \phi_i|,\ i = \overline{1, N} \tag{3.16}$$

$$\frac{\partial \psi}{\partial t} = -\frac{\partial E_{membrane}(\psi)}{\partial \psi} = -F_{membrane}|\nabla \psi| \tag{3.17}$$

It has to be noted that these equations are mutually dependent due to energy functions $E_{inner}(\phi_i)$ interact with each other and with the $E_{membrane}(\psi)$ via the $E_{overlap}(\phi_i)$ and $E_{overlap}(\psi)$. Thus the equations (3.16) and (3.17) have to be solved simultaneously.

### 3.2.5 Fast two-cycle algorithm

The level set method has many advantages, however, its implementations that directly and fully solve PDEs, such as (3.16) and (3.17), with numerical methods are computationally expensive. Different approaches have been taken to increase the processing speeed of the evolution of the zero-level functions. Some proposed techniques were focused on updating the level-set function globally over the entire regular grid [17]. Other methods suggested that in those cases when only the zero level set is of interest, then to accelerate processing it is sufficient to perform computations only in a restricted neighborhood of the zero level set. These methods were called narrow band techniques [60], [90], [103], [104].

One example of narrow band methods is [2], where a tube is constructed in the neighborhood of the zero level set, that is initialized as a signed distance function within this tube. When the zero level set becomes too close to the edge of the tube, then both the tube and level set function is reinitialized with the fast marching method [102]. Modification of this approach in which a Hamilton-Jacobi PDE is solved to initialize the level set was late presented in [90].

A significant number of development methods attempt to solve the associated evolution PDEs accurately, yet for some problems, such as image segmentation, accuracy is not necessary. Exploiting this idea Shi and Karl [103], [104] developed a method, that completely avoids direct calculations of PDEs. This method was able to achieve near real-time performance due to the fact that it does not demand reinitialization of the level set functions and update it only in the narrow band.

The boundary surface in the level set method is defined via the zero level set function $\phi$ that in discrete case is defined over a grid. Specifying that $\phi$ is negative inside the and positive outside the surface with the implicit boundary representation, it is possible to define two sets $L_{in}$ and $L_{out}$ of neighboring points [103].

$$\begin{aligned} L_{in} &= \{\vec{x} | \phi(\vec{x}) < 0, \exists\, \vec{x}_0 \in N(\vec{x}) : \phi(\vec{x}_0) > 0\} \\ L_{out} &= \{\vec{x} | \phi(\vec{x}) > 0, \exists\, \vec{x}_0 \in N(\vec{x}) : \phi(\vec{x}_0) < 0\} \end{aligned} \tag{3.18}$$

In the Shi-Karl method instead of directly solving PDE (3.4) these two sets $L_{in}$ and $L_{out}$ are evolved. The evolution is separated into two cycles: data driven expansion and smoothness regularization with a term derived from a Gaussian filtering process. The first cycle switches grid points from one set $L_{in}$ or $L_{out}$ to another, specified by the sign of the discrete approximation $\hat{F}$ of the speed function, therefore shrinking or expanding the boundary. The regulation cycle provides smoothness regulation to the boundary using local Gaussian filtering. The points during this step are added to one of the sets, depending on the sign of convolution of the level set function with a Gaussian filter. The iteration procedure stops when the stop condition (3.19) is satisfied or if a pre-specified maximum number of iterations is reached.

$$\hat{F}(\vec{x}) \leq 0, \forall x \in L_{out}, \quad \hat{F}(\vec{x}) \geq 0, \forall x \in L_{in} \tag{3.19}$$

Those equations disagree with each other on which direction to evolve the boundary only when the energy minimum is reached.

In comparison to other narrow band techniques, the Shi-Karl algorithm performs computation only with two lists of grid points neighboring the surface boundary. Although it belongs to the class of narrow band techniques, representing one of the extreme cases, it has one fundamental difference. The level set curve evolution is done without solving any PDE, thus there is no need for controlling step size or maintaining numerical stability. Despite avoiding using PDEs, this method preserves all the advantages of the level set: generality of formulations for an arbitrary number of dimensions and automatic handling of topological changes.

### 3.2.6 Discrete approximation

To solve the segmentation problem, defined by the equations (3.16), (3.17), with the Shi-Karl algorithm it is necessary to give a discrete approximation for each term first.

There are numerous ways to define the approximation of the level set functions $\phi_i$ and $\psi$. For faster computation, it is advised to chose values from a limited set of integers, for example as given in equation (3.20).

$$\phi_i(\vec{x}),\ \psi(\vec{x}) = \begin{cases} 3, & \text{if } \vec{x} \text{ is an exterior point} \\ 1, & \text{if } \vec{x} \in L_{out} \\ -1, & \text{if } \vec{x} \in L_{in} \\ -3, & \text{if } \vec{x} \text{ is an interior point} \end{cases} \tag{3.20}$$

This particular definition allows easily distinguish the relative location of any point with respect to boundary surface.

The discrete approximations $\hat{F}_{inner}$ and $\hat{F}_{membrane}$ of the speed functions in (3.16), (3.17) are acquired by approximating derivatives of each term in $\frac{\partial E_{inner}(\phi_i)}{\partial t}$ and $\frac{\partial E_{inner}(\psi)}{\partial t}$.

For the edge speed function $\hat{F}_{edge}$, corresponding to the energy $E_{edge}(\phi_i)$, a central-difference approximation of derivatives of the equation (3.8) is used.

$$\hat{F}_{edge} = \bar{e}_x^{'}\bar{\phi}_{i_x}^{'} + \bar{e}_y^{'}\bar{\phi}_{i_y}^{'} + \bar{e}_z^{'}\bar{\phi}_{i_z}^{'} \tag{3.21}$$

$$\begin{aligned} \bar{e}_x^{'} &= e(x+1,y,z) - e(x-1,y,z) \\ \bar{\phi}_{i_x}^{'} &= \phi_i(x+1,y,z) - \phi_i(x-1,y,z) \end{aligned} \tag{3.22}$$

The edgeness function $e(x,y,z)$ in this equation is defined to be the Euclidean distance transform of the result of Canny edge detector [46] applied to images of cell membranes $J(\bar{x})$

Likewise, $\hat{F}$ of each energy term is created. The value of the discrete functions $\hat{F}_{overlap}$, representing $E_{overlap}(\phi_i)$ and $E_{overlap}(\psi)$, is set to $-1$ in the overlapped region, while everywhere else it is zero. The term $|\nabla\phi_i|$ is calculated with a first order upwind scheme. Finally, for the region speed $\hat{F}_{volume}$ and $\hat{F}_{nucleus}$ a range of intensities is specified, where the function is $-1$, otherwise it is $1$.

$$\hat{F}_{nucleus}(x,y,z) = \begin{cases} -1 & \text{if } I(x,y,z) \in [I_1, I_2] \\ 1 & \text{otherwise} \end{cases} \tag{3.23}$$

$$\hat{F}_{volume}(x,y,z) = \begin{cases} -1 & \text{if } J(x,y,z) \in [J_1, J_2] \\ 1 & \text{otherwise} \end{cases} \tag{3.24}$$

The main parameters in the Shi-Karl algorithm are number of iterations for each cycle and the size of Gaussian filter kernel. Following suggestions, discussed in [103], for the

choice of these parameters the method was set to perform $3$ steps for the evolution and $1$ step with $5 \times 5$ kernel for the regularization cycle.

## 3.3 Experimental results

### 3.3.1 Dataset

For testing the proposed 3D level set method 20 embryo samples at various development stages (4-32 cells) were collected. The embryos were obtained by crossing female H2B-mCherry mice with mG mice. After recovering the embryos they were cultured under the condition of 37C, 5% CO2 in 20$\mu$l drop of KSOM in the chamber installed in the inverted light-sheet microscope [109]. The visual data was composed of 130 optical cross sections, acquired every 10 minutes, the distance between the two consecutive optical slices was 1$\mu$m, then scaled to have 260 images. The resolution of the input images was 260x260.

To initialize the primary sets $L^i_{in}$ and $L^i_{out}$, used in Shi-Karl iterative algorithm, cell nuclei were detected. To do that, first, the input images of the nuclei Z-stack were smoothed with the 3D Gaussian filter, followed by Otsu's adaptive thresholding. Next, among all blobs, located with the connected labeling method, $N$ with a maximum number of points were chosen. Finally, the sets were calculated according to their definitions (3.18). The same approach was applied to determine initial sets of cell membranes.

### 3.3.2 Qualitative accuracy evaluation

The results of the segmentation of embryos with a different number of cells are presented in figures Fig. 3.10 and Fig. 3.11. The Fig. 3.10 presents results of the segmentation as 3D renders of cell inner regions and all membranes for embryos that contain 4, 8, 16, 24, and 32 cells. The Fig. 3.11 displays some selected cross-sections of the same embryos.

Visually examining the results of segmentation it was possible to conclude that the method was able to rather correctly identify inner cell regions and membranes in those cases when embryos consisted of 4, 8, and 16 cells. However, if the number of blastomeres was 24 or 32 the algorithm appeared to provide less accurate results. The shapes of the detected inner regions were less smooth, with traces of under-segmentation (see Fig. 3.11, columns (d) and (e)). The obtained surface of cell membranes, on the other hand, appeared to suffer less from those problems observed for inner regions.

These results can be explained by studying the changes occurring in the embryos with the increase of the number of blastomeres. The most striking morphological change that occurs at the 24-32 stage is the formation of an internal cavity, forcing blastomeres to clutter to one side of the embryo. The outer embryo membranes, separating it from the outside environment become less visible, their intensity is low, while the membranes between cells become more prominent.

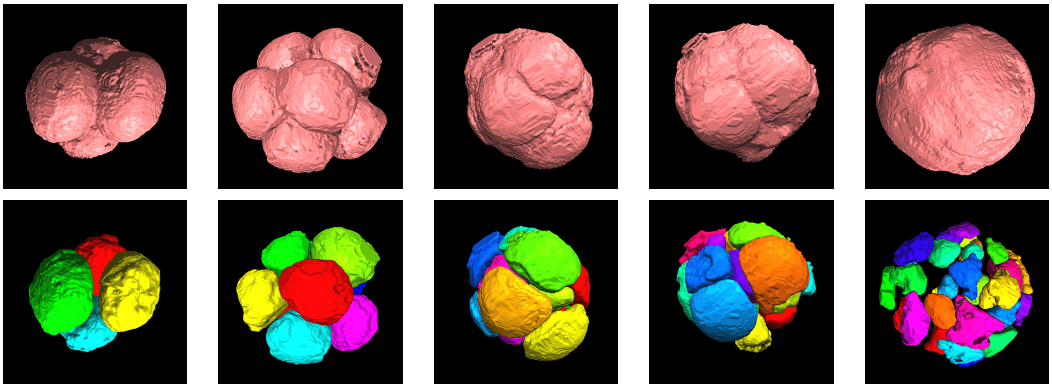

(a) 4 (b) 8 (c) 16 (d) 24 (e) 32

Figure 3.10: 3D reconstruction of segmentation results for inner cell regions and membranes for embryos containing 4, 8, 16, 24, and 32 cells.

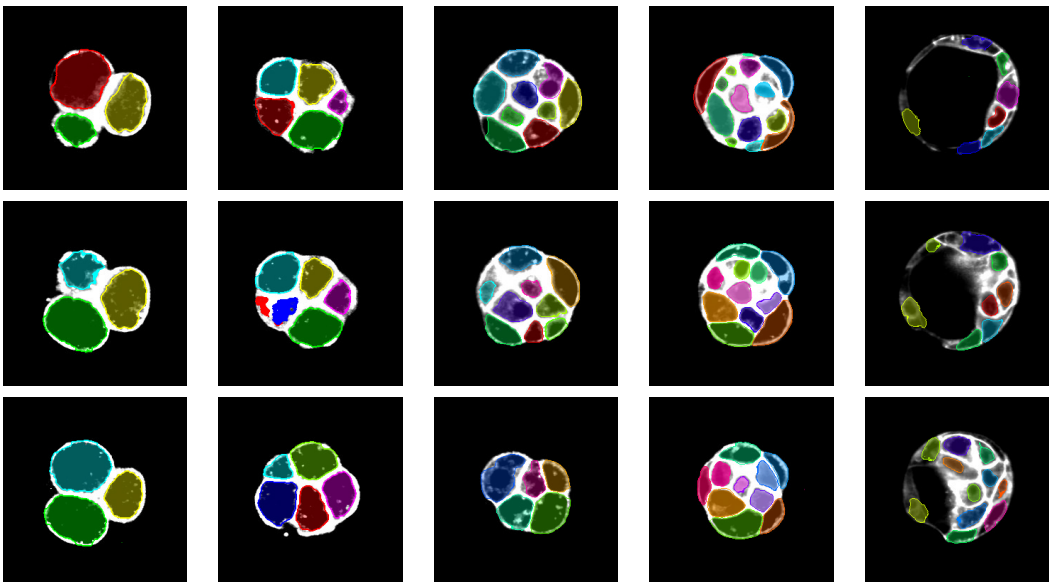

(a) 4 (b) 8 (c) 16 (d) 24 (e) 32

Figure 3.11: Cross sections of embryos that contain 4, 8, 16, 24, and 32 blastomeres that display the results of the inner region segmentation with the developed method.

### 3.3.3 Quantitative accuracy evaluation

Performing quantitative assessment of the segmentation accuracy for the desribed task can not be done straightforward, since it is impossible to obtain ground truth labeling for blastomeres and membranes from any direct measurements. Therefore, to conduct tests, the ground truth set was built by manually specifying areas of inner cell regions and membranes on the input images.

The accuracy of the segmentation for each cell component was evaluated as an average F-score, which is defined as the harmonic mean of precision and recall (see Equations (3.25) and (3.26)).

$$F = \frac{2 \times precision \times recall}{precision + recall} \tag{3.25}$$

If the segmentation result obtained with the proposed method is denoted as $S_e$ and $S_0$ is the ground truth, then precision and recall are defined as:

$$precision = \frac{|S_e \cap S_0|}{|S_e|} \qquad recall = \frac{|S_e \cap S_0|}{|S_0|} \tag{3.26}$$

The results of the segmentation for inner cell regions and membranes given as precision, recall and F-measure are presented in Table 3.1 and Table 3.2.

| Cell count | 4 | 8 | 16 | 24 | 32 |
|---|---|---|---|---|---|
| Precision | 0.93 | 0.93 | 0.85 | 0.8 | 0.66 |
| Recall | 0.93 | 0.9 | 0.9 | 0.83 | 0.80 |
| F-score | 0.93 | 0.91 | 0.88 | 0.81 | 0.75 |

Table 3.1: Segmentation accuracies for inner cell regions presented as precision, recall, F-score for embryos with different number of blastomeres.

| Cell count | 4 | 8 | 16 | 24 | 32 |
|---|---|---|---|---|---|
| Precision | 0.81 | 0.78 | 0.7 | 0.73 | 0.75 |
| Recall | 0.79 | 0.77 | 0.74 | 0.69 | 0.67 |
| F-score | 0.8 | 0.79 | 0.72 | 0.72 | 0.7 |

Table 3.2: Segmentation accuracies for cell membranes presented as precision, recall, F-score for embryos with different number of blastomeres.

The F-measure of labeling inner cell regions is 93% for the 4 cell stage and it gradually dropped as the number of cell increased. For the 32 cell embryos it reached 70%. As it was illustrated above in previous section, this tendency is caused by the increasing embryo's morphological complexity as it undergoes cell division. Segmentation accuracy for the membranes is slightly lower than inner cells, ranging from 70% to 77%, depending on the number of cells.

### 3.3.4 Comparison with other methods

Segmentation results obtained with the proposed algorithm were also compared with those acquired by applying 3D version of the watershed algorithm [66]. Initial markers were set up to be cell nuclei that were extracted in the same way as was described in the previous chapter by applying Gaussian smoothing, followed by adaptive thresholding. The input images of embryo membranes were thresholded to obtain binary image, then dilated in order to separate the volume occupied by the embryo cells from the background, then the binary representation of the membrane is subtracted from the images obtained at the previous step.

The watershed method successfully detected some cell regions, yet other regions suffered from under-segmentation. The segmentation accuracy for embryos with 4, 8, 16, and 24 blastomeres of the watershed algorithm was lower than the proposed 3D level set method (see Table. 3.3). For 32 cell embryo, the watershed approach showed slightly better results. However, it has to be noted that this implementation of the watershed unlike the developed level set method allowed detection only of the inner cell region and not designed for reconstructing membranes.

| Cell count | 4 | 8 | 16 | 24 | 32 |
|---|---|---|---|---|---|
| 3D level set | 0.93 | 0.91 | 0.88 | 0.81 | 0.75 |
| Watershed | 0.73 | 0.89 | 0.83 | 0.78 | 0.77 |

Table 3.3: Comparison of inner cell region segementation accuracy achieved with the developed 3D level set method and watershed method.

For this moment, there are two previous reports on the problem of embryo segmentation with a numerical assessment of the developed approach. Guisti et al. [37] proposed a method that involves processing of Z-stack of HMC images. They assessed its efficiency on 53 4-cell embryo image stacks. During the testing stage, the candidate cell was considered as correct if its Jaccard similarity index was higher than 0.8, achieving 71% of accuracy. Singh et al. [105] applied isoperimetric graph partitioning to HMC embryo images to approximate blastomere position. It achieved 81% of accuracy (Jaccard similarity index was also set to 0.8) on a dataset of 40 embryo images. In comparison, the approach described in this thesis was able to achieve 90% with the same evaluation technique.

### 3.3.5 Analysis of individual energy terms

Fine-tuning weights in the definition of the energy functions $E_{inner}(\phi_i)$ and $E_{membrane}(\psi)$ is a difficult procedure, since there is no guarantee that the chosen set allows achieving the best accuracy. Thus to understand how the individual energies affect accuracy of segmentation a number of weight sets were tested (see Table 3.4 and Table 3.5). The accuracies of blastomere and membrane segmentation were calculated for an embryo with 8 cells.

| $w_1$ | $w_2$ | $w_3$ | Accuracy |
|---|---|---|---|
| 0 | 1 | 1 | 0.63 |
| 1 | 1 | 0 | 0.74 |
| 1 | 1 | 1 | 0.90 |
| 1 | 1 | 3 | 0.91 |

Table 3.4: Accuracy of cell region segmentation depending on weight values for an embryo with 8 cells presented as F-score

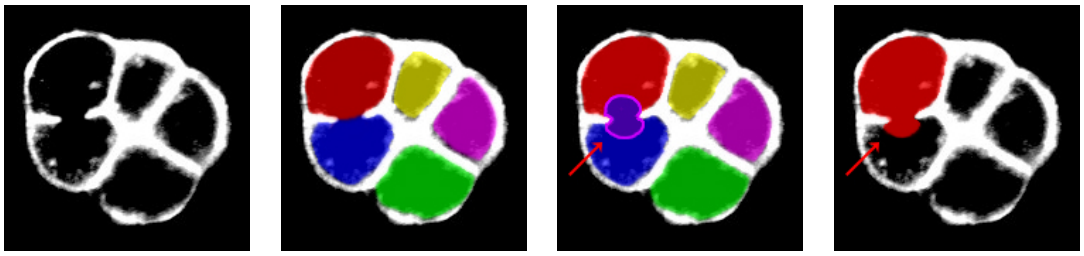

(a) (b) (c) (d)

Figure 3.12: (a) An input cross section. (b) Inner cell regions detected with $E_{overlap}(\phi_i)$ term included into the definition. (c-d) Inner cell regions detected without using $E_{overlap}(\phi_i)$.

The $E_{edge}(\phi_i)$ is the main force which expands the boundaries during evolution. If this term is removed the result of the segmentation algorithm is the initial surfaces – borders of the cell nuclei. The energy function $E_{overlap}(\phi_i)$ plays a significant role in cases when there are holes or gaps in membranes separating two blastomeres. If the energy is not used then the detected inner regions become overlapped (see Fig. 3.12).

| $v_1$ | $v_2$ | $v_3$ | Accuracy |
|---|---|---|---|
| 1 | 0 | 0 | 0.75 |
| 0 | 1 | 1 | 0.77 |
| 1 | 1 | 1 | 0.79 |
| 1 | 1 | 3 | 0.8 |

Table 3.5: Accuracy of membrane segmentation depending on weight values for an embryo with 8 cells presented as F-scores

Exclusion of $E_{volume}(\psi)$ forces to rely only on $E_{inclusion}(\psi)$ during evolution of cell membranes, results in under segmentation.

For restoring the morphology of the embryo and covering the holes in membranes the $E_{inclusion}(\psi)$ is extremely useful (see Fig. 3.12). It approximates the membrane and fills the gaps. The negative effect of using this energy is that the thickness of boundary could increase, if the constant $D$ chosen in equation (3.15) is too high.

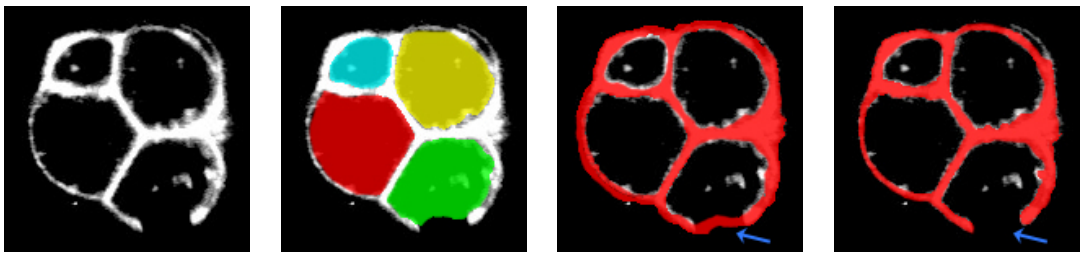

(a) (b) (c) (d)

Figure 3.13: (a) An input cross section. (b) Detected inner cell regions. (c) Detected membranes with $E_{inclusion}(\psi)$. (d) Detected membranes without $E_{inclusion}(\psi)$.

## 3.4 Discussion

### 3.4.1 Improving the accuracy

The second part of this thesis was dedicated to a new method for performing segmentation of early stage embryos from Z-stacks of fluorescence images. The use of fluorescence visual data instead of images, obtained with Hoffman Modulation Contrast (HMC) technique greatly facilitates localization of blastomeres and cell membranes.

Experimental results showed that the developed 3D level set algorithm is capable of segmenting efficiently embryos with up to 24 cells. However due to significant changes in internal embryo morphology it did not achieve good results for the samples containing 32 cells (Figure 3.14: (a), (b)). The advantages of the designed 3D level set method include handling complex embryo morphology, restoring regions of membranes with low visibility and processing speed.

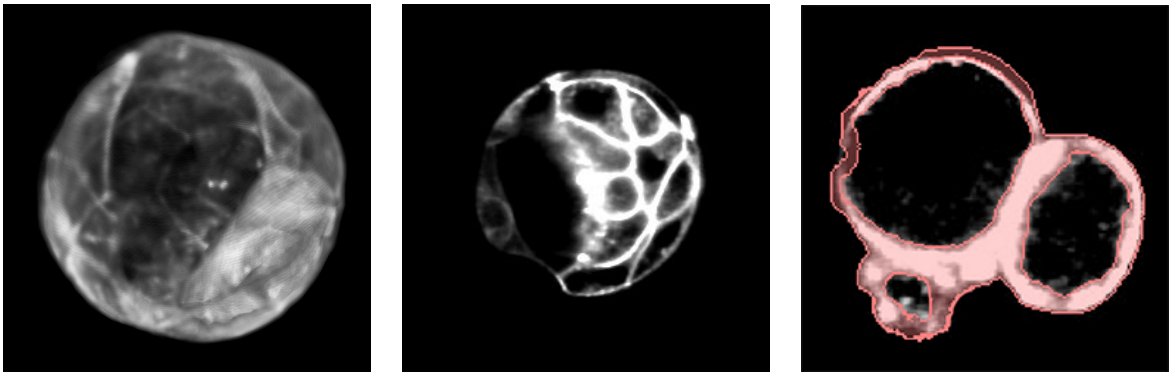

(a) (b) (c)

Figure 3.14: (a) A 3D model reconstructed from the input cross sections of the 32 cell embryo. (b) A cross section of a 32 cell embryo. (c) Missdetection of membrane regions.

There are two factors which primarily affect the segmentation accuracy of the developed method. The first one is the design and usage of the energy term $E_{inclusion}(\psi)$. This energy was created to correctly fill 'holes' by enveloping inner cell regions and in

some cases it forces to incorrectly add regions which are not belong to membranes (Figure 3.14: (c)). The second factor, contributing to estimation accuracy, is the precision of Canny detector used for computing edgeness function $e(x, y, z)$ in (3.21). Re-defining edgeness metric with a different function potentially can increase the accuracy.

Another approach for improving segmentation accuracy, for the 32-cell embryos in particular, is to introduce additional energies into equation (3.7) and (3.8). For example, to carry out more direct control of blastomere smoothness an individual smoothness energy can be included into computations, instead of relying on regularization cycle of the Shi-Karl iterative algorithm. Specifying an energy for a cavity in the 32-cell embryo could also increase the result of segmentation.

# Chapter 4

# Conclusion

The advances in live cell imaging allowed rapid acquisition of big quantities of visual data without effort, dramatically transforming the biomedical science. Image-based experiments became the standardized approach to carry out scientific studies. Despite significant progress achieved in inventing new devices for data acquisition, there is a lack of tools capable to process this data automatically, such as to detect cells, extract features, perform segmentation, or carry high-level analysis. This issue motivated the scientific community to focus on developing new computer-based methods for aiding biomedical research.

Image processing frameworks that were primarily designed for generic tasks of image classification or semantic segmentation are often not directly applicable to biomedical problems. Frequent changes in device settings used to obtain images, high variety of input samples, the necessity of achieving high accuracy - all these factors make it challenging to devise a robust approach. Furthermore, not only the construction of an efficient algorithm, but also an assessment of its accuracy presents difficulties. The main reason is that commonly the ground truth, especially in cases of where it is required to execute cell detection or segmentation, cannot be obtained by direct measurements, demanding to reserve to indirect evaluation, qualitative analysis or providing manually prepared ground truth data.

In this thesis, two new methods for computer-aided biomedical image analysis were presented. More specifically, both of the developed methods targeted the most common task that occurs during biomedical research - cell analysis.

The first method was built to aid bacteriologists with the task of DST. The DST was done with the special microfluidic device - DSTM device, designed to reduce time necessary to obtain the image of cells grown in presence of drug with different concentrations. Before conducting studies, described in this thesis, the cell analysis procedure was carried out manually, by visually observing changes in cell growth rate and morphology, examining images of the device captured with a camera attached to a phase contrast microscope. The implementation of the developed algorithm for automatic cell analysis, which was produced as stand-alone tool, greatly facilitates DST procedure. It allows not only efficiently detect cells and extract their features, that can be used later for detailed analysis by a human expert, but is also capable of determining strain susceptibility and its MIC without any user involvement. The tests, evaluating accuracy of the built algo-

rithm on a dataset, containing 101 images for each one of 5 drugs, showed high accuracy. The method was able to achieve a 97% accuracy, despite the fact, that rather straightforward image processing techniques were used. The developed software application has been planned to supply with the device to hospitals, and other medical organisations to facilitate rapid drug testing.

The second method was designed to solve the task of early-stage embryo segmentation into inner cell regions and membranes. This task has to be carried out in order to extract various features of cells embryo consists of. Knowledge of cell characteristics would allow building new models of cell specialization process, moving forward the field of transplant medicine and genetic disorder diagnosis. Early techniques for achieving embryo segmentation used HMC images, that due to the process of acquisition, make it dramatically more complex to obtain correct results for embryos with high number of cells. Fluorescene protein imaging procedure makes it possible to capture images with marked cell components, such as membranes and nuclei. Exploiting this advantage, a new 3D level set method for embryo segmentation from 2 Z-stacks (cell membrane and nuclei) was introduced in this thesis. The 3D level set involves solving PDEs, derived from definition of energy functions. The energy functions in the proposed methods were designed to take into account intensity levels of cell membranes and internal morphological structure. Instead of solving PDEs directly, an iterative two cycle technique was used, significantly reducing computational burden. To visualize results, and stand-alone tool was created, utilized to conduct qualitative and quantitative assessment of the accuracy of the proposed algorithm. The accuracy of the method achieved 93% for 4-cell embryo, gradually reduced with the increase of blastomeres, reaching 75% for 32-cell case.

More and more challenging tasks in the biomedical field are being automated with the image processing methods. Automated systems, such as those presented in this thesis, provide quick and effective solutions for performing high throughput quantitative analysis, alleviating the necessity in manual processing, which is without doubt beneficial to the scientific community. Further improvements in image processing methods and introduction of learning based algorithms can potentially increase the efficiency of the proposed approaches.

## Bibliography


[1] Abramoff, M. D., Magalhaes, P. J., and Ram, S. J. (2004). Image processing with ImageJ. *Biophotonics international*, 11:36–42. 2.2.2

[2] Adalsteinsson, D. and Sethian, J. A. (1995). A fast level set method for propagating interfaces. *Journal of Computational Physics*, 118:269–277. 3.2.1, 3.2.5

[3] Al-Kofahi, Y., Lassoued, W., Lee, W., and Roysam, B. (2010). Improved automatic detection and segmentation of cell nuclei in histopathology images. *IEEE Trans Biomed Eng*, 57(4):841–52. 3.1.3

[4] Amann, R. I., Krumholz, L., and Stahl, D. A. (1990). Fluorescent-oligonucleotide probing of whole cells for determinative, phylogenetic, and environmental studies in microbiology. *Journal of Bacteriology*, 172:762–70. 2.2.2

[5] Barenfanger, J., Drake, C., and Kacich, G. (1999). Clinical and financial benefits of rapid bacterial identification and antimicrobial susceptibility testing. *J. Clin. Microbiol*, 37:1415–1418. 2.1.3

[6] Bauer, A. W., Kirby, W. M., Sherris, J. C., and Turk, M. (1966). Antibiotic susceptibility testing by a standardized single disk method. *Am J Clin Pathol*, 45:493–6. 2.1.3

[7] Bedzhov, I., Graham, S. J. L., Leung, C. Y., and Zernicka-Goetz, M. (2014). Developmental plasticity, cell fate specification and morphogenesis in the early mouse embryo. *Philosophical Transactions of the Royal Society of London B: Biological Sciences*, 369(1657). 3.1.2, 3.1.2

[8] Bergen, J. R. and Shvayster (Schweitzer), H. (1991). A probabilistic algorithm for computing hough transforms. *Journal of Algorithms*, 12:639–656. 2.2.5

[9] Brinkmann, M., Lutkemeyer, D., Gudermann, F., and Lehmann, J. (2001). New technologies for automated cell counting based on optical image analysis The Cellscreen. *in Proc. of the 17th ESACT Meeting*, 1:269–273. 1.1, 2.2.2

[10] Brox, T. and Weickert, J. (2006). Level set segmentation with multiple regions. *IEEE Trans. on Image Processing*, 15:3213–3218. 3.2.2

[11] Burges, C. J. (1998). A tutorial on support vector machines for pattern recognition. *Data Mining and Knowledge Discovery*, 2:121167. 2.2.8

[12] Canny, J. F. (1986). A computational approach to edge detection. *IEEE Transactions on Pattern Analysis and Machine Intelligence*, 8(6):679 – 698. 3.2.1

[13] Carpenter, A. E., Jones, T. R., Lamprecht, M. R., Clarke, C., Kang, I. H., Friman, O., Guertin, D. A., Chang, J. H., Lindquist, R. A., Moffat, J., Golland, P., and Sabatini, D. M. (2006). Cellprofiler: image analysis software for identifying and quantifying cell phenotypes. *Genome Biology*, 7. 2.2.2

[14] Carpenter, A. E. and Sabatini, D. M. (2004). Systematic genome-wide screens of gene function. 5:11–22. 2.2.1

[15] Caselles, V., Kimmel, R., and Sapiro, G. (1997). Geodesic active contours. *International Journal of Computer Vision*, 22:61–79. 3.2.3

[16] Cates, J. E., Lefohn, A. E., and Whitaker, R. T. (2004). Gist: an interactive, gpu-based level set segmentation tool for 3d medical images. *Journal on Medical Image Analysis*, 8:217–231. 3.2.1

[17] Chan, T. F. and Vese, L. A. (2001). Active contours without edges. *IEEE Transactions on Image Processing*, 10(2):266 – 277. 3.2.5

[18] Chen, C. H., Lu, Y., Sin, M. L. Y., Mach, K. E., Zhang, D. D., Gau, V., Liao, J. C., and Wong, P. K. (2010). Antimicrobial susceptibility testing using high surface-to-volume ratio microchannels. *Analytical Chemistry*, 82:1012–1019. 2.1.1, 2.4.1

[19] Clinical and Institute, L. S. (2009). Performance standards for antimicrobial disk susceptibility tests. approved standard m2-a10. *Wayne, PA: Clinical and Laboratory Standards Institute*. 2.1.3

[20] Cohen, L. D. and Cohen, I. (1990). A finite element method applied to new active contour models and 3d reconstruction from cross sections. *Proceedings Third International Conference on Computer Vision*. 3.2.1

[21] Commons, W. (2010). A completed broth microdilution test. File: MIC microbroth dilution.jpg. (document), 2.3

[22] Conly, J. M. and Johnston, B. L. (2005). Where are all the new antibiotics? the new antibiotic paradox. *The Canadian Journal of Infectious Diseases and Medical Microbiology*, 16(3):159160. 2.1.2

[23] Cremers, D., Rousson, M., and Deriche, R. (2007). A review of statistical approaches to level set segmentation: Integrating color, texture, motion and shape. *International Journal of Computer Vision*, 72:195215. 3.2.2, 3.2.3, 3.2.3

[24] Dard, N., Louvet-Valle, S., and Maro, B. (2009). Orientation of mitotic spindles during the 8- to 16-cell stage transition in mouse embryos. *PLoS ONE*, 4(12):1–8. 3.1.2

[25] Dervieux, A. and Thomasset, F. (1979). A finite element method for the simulation of a rayleigh-taylor instability. *Lecture Notes in Mathematics*, 771:145–159. 3.2.2

[26] Dillencourt, B. M., Samet, H., and Tamminen, M. (1992). A general approach to connected-component labeling for arbitrary image representations. *Journal of the ACM*, 39:253. 2.2.6

[27] Doern, G. V., Vautour, R., Gaudget, M., and Levy, B. (1994). Clinical impact of rapid in vitro susceptibility testing and bacterial identification. *J Clin Microbiol*, 32:1757–62. 2.1.3

[28] Douglas, I. S., Price, C. S., Overdier, K. H., Wolken, R. F., Metzger, S. W., Hance, K. R., and Howson, D. C. (2015). Rapid automated microscopy for microbiological surveillance of ventilator-associated pneumonia. *PubMed*, 191(5):566–73. 2.4.1

[29] Duda, R. O. and Hart, P. E. (1972). Hough transformation to detect lines and curves in pictures,. *Communications of the ACM*, 15:11–15. 2.2.5

[30] Dufour, A., Shinin, V., Tajbakhsh, S., Guillen-Aghion, N., and Olivo-Marin, J.-C. (2005). Segmenting and tracking fluorescent cells in dynamic 3-d microscopy with coupled active surfaces. *IEEE Signal Processing Society*, 14:1396–1410. 1.1, 3.1.4, 3.1.5

[31] Dzyubachyuk, O., A. van Cappellen, W., Essers, J., and J. Nissen, W. (2010). Advanced level-set-based cell tracking in time-lapse fluorescence microscopy. *IEEE Transactions on Medical Imaging*, 29:852–867. 1.1, 3.1.4, 3.1.5

[32] Ericsson, H. M. and Sherris, J. C. (1971). Antibiotic sensitivity testing. report of an international collaborative study. *Acta Pathol Microbiol Scand B Microbiol Immunol.*, 217. 2.1.3

[33] Fernandez, R., Das, P., Mirabet, V., Moscardi, E., Traas, J., Verdeil, J.-L., Malandain, G., and Godin, C. (2001). Imaging plant growth in 4d: robust tissue reconstruction and lineaging at cell resolution. *Nat Meth*, 7(7):547–553. 3.1.3

[34] Flannery, B. P., Teukolsky, S., Press, W. H., and Vetterling, W. T. (1992). *Numerical Recipes in C*. Cambridge: Cambridge University Press, New York, NY, USA, 2nd edition. 2.2.4

[35] Garippa, R. J. (2004). A multi-faceted approach to the advancement of cell-based drug discovery. *Drug Discovery World*, 6:43–55. 2.2.2

[36] Gharipour, A. and Wee-ChungLiew, A. (2016). Segmentation of cell nuclei in fluorescence microscopy images: An integrated framework using level set segmentation and touching-cell splitting. *Pattern Recognition*, 58:1–11. 3.1.4

[37] Giusti, A., Corani, G., Gambardella, L., Magli, C., and Gianaroli, L. (2010). Blastomere segmentation and 3d morphology measurements of early embryos from hoffman modulation contrast image stacks. *in Proc. Biomedical Imaging: From Nano to Macro, 2010 IEEE International Symposium on*. Embryo from a Z-stack of HMC images. 1.3, 3.1.3, 3.3.4

[38] Goldenberg, R., Kimmel, R., Rivlin, E., and Rudzsky, M. (2001). Fast geodesic active contours. *IEEE Trans. Med. Imag.*, 10:14671475. 3.2.3

[39] Grushnikov, A., Kikuchi, K., Matsumoto, Y., Kanade, T., and Yagi, Y. (2017a). Automatic image analysis for rapid drug susceptibility testing. *Advanced Biomedical Engineering*, 6:76–82. 1.3

[40] Grushnikov, A., Niwayama, R., Kanade, T., and Yagi, Y. (2017b). 3d level set method for blastomere segmentation of preimplantation embryos in fluorescence microscopy images. *Machine Vision and Applications*, pages 1–11. 3.1.5

[41] Guillaud, M., Adler-Storthz, K., Malpica, A., Staerkel, G., Matisic, J., Van Niekirk, D., Cox, D., Poulin, N., Follen, M., and MacAulay, C. (2005). Subvisual chromatin changes in cervical epithelium measured by texture image analysis and correlated with hpv. *Gynecologic Oncology*, 99:16–23. 2.2.1

[42] Guo, Z. and Hall, R. W. (1989). Parallel thinning with two-subiteration algorithms. *Communications of the ACM*, 32:359–373. 2.2.6

[43] H., T. (1978). A comparison of line thinning algorithms from digital geometry viewpoint. *in Proc. 4th IJCPR*, pages 715–719. 2.2.6

[44] Hillman, N., Sherman, M. I., and Graham, C. (1972). The effect of spatial arrangement on cell determination during mouse development. *J. Embryol. Exp. Morphol.*, 28:263–278. 3.1.2

[45] Huang, M. B., Baker, C. N., Banerjee, S., and Tenover, F. C. (1992). Accuracy of the e test for determining antimicrobial susceptibilities of staphylococci, enterococci, campylobacter jejuni, and gram-negative bacteria resistant to antimicrobial agents. *J Clin Microbiol*, 30:3243–8. 2.1.3

[46] Huang, X., Metaxas, D., and Chen, T. (2004). Metamorphs: Deformable shape and texture models. *in IEEE Conf. on Computer Vision and Pattern Recognition*, pages 496–503. 3.2.6

[47] Iino, R., Nishino, K., Yamaguchi, A., and Matsumoto, Y. (2012). A microfluidic device for simple and rapid evaluation of multidrug efflux pump inhibitors. *Front Microbiol.*, 3. 1.3, 2.1.1, 2.1.3, 2.1.4, 2.4.1

[48] Jagusztyn-Krynicka, E. K. and Wyszynska, A. (2008). The decline of antibiotic era–new approaches for antibacterial drug discovery. *Polish Journal of Microbiology*, 57(2):91–98. 2.1.2

[49] Jorgensen, J. H. and Ferraro, M. J. (2009). Antimicrobial susceptibility testing: A review of general principles and contemporary practices. *Clin Infect Dis.*, 49:1749–1755. (document), 2.1.3, 2.1.3, 2.4

[50] Jorgensen, J. H., Ferraro, M. J., McElmeel, M. L., Spargo, J., Swenson, J. M., and Tenover, F. C. (1994). Detection of penicillin and extended-spectrum cephalosporin resistance among streptococcus pneumoniae clinical isolates by use of the e test. *J Clin Microbiol*, 32:159–63. 2.1.3

[51] Jungil, C., Jungheon, Y., Mincheol, L., Eun-Geun, K., Ji Soo, L., Seungok, L., Seik, J., Sang Hoon, S., and et. al. (2014). A rapid antimicrobial susceptibility test based on single-cell morphological analysis. *Science Translational Medicine*, 6. 2.1.1, 2.1.3, 2.4.1

[52] Jungil, C., Yong-Gyun, J., Jeewoo, K., Sungbum, K., Yushin, J., Hunjong, N., and

Sunghoon, K. (2013). Rapid antibiotic susceptibility testing by tracking single cell growth in a microfluidic agarose channel system. *Lab Chip*, 13:280–287. 2.1.1, 2.1.3, 2.4.1

[53] Kass, M., Witkin, A., and Terzopoulos, D. (1988). Snakes: Active contour models. *International Journal of Computer Vision*, 1(4):321–331. 3.2.1

[54] Kepner, R. L. and Pratt, J. R. (1994). Use of fluorochromes for direct enumeration of total bacteria in environmental samples: past and present. *Microbiol Rev*, 58:603–15. 2.2.2

[55] Keraudren, K., Spitaler, M., Braga, V., Rueckert, D., and Pizarro, L. (2011). Two-step watershed segmentation of epithelial cells. *in Proc. 6th int. MIAAB Workshop*. 2.2.2, 2.2.6

[56] Kiryati, N., Eldar, Y., and Bruckstein, A. M. (1991). A probabilistic hough transform. *Pattern Recognition*, 24:303–316. 2.2.5

[57] Klein, A., Van den Doel, R., Young, I. T., and Van Vliet, L. J. (2012). Quantitative evaluation and comparison of light microscopes. *in Proc. of SPIE The International Society for Optical Engineering*. 2.2.2, 2.2.4

[58] Kong, J., Wang, F., Teodoro, G., Liang, Y., Zhu, Y., Tucker-Burden, C., and Brat, D. J. (2015). Automated cell segmentation with 3d fluorescence microscopy images. *Proc IEEE Int Symp Biomed Imaging*, pages 1212–1215. 3.1.3

[59] Lee, V. C. (2015). The antibiotic resistance crisis: Part 1: Causes and threats. pharmacy and therapeutics. *Pharmacy and Therapeutics"*, 40:277–283. 2.1.2, 2.1.2

[60] Lefohn, A. E., Kniss, J. M., Hansen, C. D., and Whitaker, R. T. (2004). A streaming narrow-band algorithm: Interactive computation and visualization of level sets. *IEEE Trans. on Visualization and Computer Graphics*, 10:422–433. 3.2.1, 3.2.5

[61] Leonardis, A., Gupta, A., and Bajcsy, R. (1995). Segmentation of range images as the search for geometric parametric models. *International Journal of Computer Vision*, 14(3):253–277. 3.2.1

[62] Levy, S. B. (1992). *The Antibiotic Paradox. How Miracle Drugs are Destroying Miracle*. Plenum Publishing, New York. 2.1.2

[63] Levy, S. B. (2002). Factors impacting on the problem of antibiotic resistance. *J. Antimicrob. Chemother.*, 49:25–30. 2.1.2, 2.1.2

[64] Li, G., Liu, T., Tarokh, A., Nie, J., Guo, L., Mara, A., Holley, S., and Wong, S. T. (2007). 3d cell nuclei segmentation based on gradient flow tracking. *BMC Cell Biology*, 8. 3.1.3

[65] Lou, X., Kang, M., Muoz-Descalzo, S., and Hadjantonakis, A.-K. (2014). A rapid and efficient 2d/3d nuclear segmentation method for analysis of early mouse embryo and stem cell image data. *Stem Cell Reports*, 11:382–397. 3.1.4

[66] Malpica, N., de Solrzano, C. O., Vaquero, J. J., Santos, A., Vallcorba, I., Garca-

Sagredo, J. M., and del Pozo, F. (1997). Applying watershed algorithms to the segmentation of clustered nuclei. *Cytometry*, 28. 2.2.2, 3.3.4

[67] Mansouri, A.-R., Mitiche, A., and Vazquez, C. (2006). Multiregion competition: A level set extension of region competition to multiple region image partitioning. *Computer Vision and Image Understanding*, 101:137150. 3.2.2

[68] Masuda, N., Sakagawa, E., Ohya, S., Gotoh, N., Tsujimoto, H., and Nishino, T. (2000). Substrate specificities of mexab-oprm, mexcd-oprj, and mexxy-oprm efflux pumps in pseudomonas aeruginosa. *Antimicrobial Agents and Chemotherapy*, 44:3322–7. 2.1.4

[69] Matas, J., Galambos, C., and Kittler, J. (2000). Progressive probabilistic hough transform. *Computer Vision and Image Understanding*, 78:119–137. 2.2.5

[70] Matsumoto, Y., Hayama, K., Sakakihara, S., Nishino, K., Noji, H., Iino, R., and Yamaguchi, A. (2011). Evaluation of multidrug efflux pump inhibitors by a new method using microfluidic channels. *PLoS One*, 6. 2.1.1, 2.1.4, 2.4.1

[71] Matsumoto, Y., Sakakihara, S., Grushnikov, A., Kikuchi, K., Noji, H., Yamaguchi, A., Iino, R., Yagi, Y., and Nishino, K. (2016). A microfluidic channel method for rapid drug-susceptibility testing of pseudomonas aeruginosa. *PLoS One*, 11. 2.1.3, 2.3.1, 2.3.7

[72] Maxim, K., Jean C., L., Jennifer, C., Andre, S., and Alexis F., S.-B. (2012). A microfluidic platform for rapid, stress-induced antibiotic susceptibility testing of staphylococcus aureus. *Lab Chip.*, 12:4523–4532. 2.4.1

[73] Metzger, S., Frobel, R. A., and Jr., W. M. D. (2014). Rapid simultaneous identification and quantitation of staphylococcus aureus and pseudomonas aeruginosa directly from bronchoalveolar lavage specimens using automated microscopy. *Diagnostic Microbiology and Infectious Disease*, 79(2):160 – 165. 2.4.1

[74] Michael, C. A., Dominey-Howes, D., and Labbate, M. (2014). The antibiotic resistance crisis: Causes, consequences, and management. *Front Public Health*, 2. 2.1.2

[75] Mitchison, T. J. (2005). Small-molecule screening and profiling by using automated microscopy. *ChemBioChem*, 6:33–39. 2.2.1

[76] Mittman, S. A., Huard, R. C., Della-Latta, P., and Whittier, S. (2009). Comparison of BD Phoenix to Vitek 2, MicroScan MICroSTREP, and Etest for antimicrobial susceptibility testing of streptococcus pneumoniae. *J Clin Microbiol*, 47:3557–61. 2.1.3

[77] Mohan, R., Mukherjee, A., Sevgen, S. E., Sanpitakseree, C., Lee, J., Schroeder, C. M., and Kenis, P. J. (2013). A multiplexed microfluidic platform for rapid antibiotic susceptibility testing. *Biosensors and Bioelectronics*, 49:118 – 125. 2.4.1

[78] Murphy, R. F., Meijering, E., and Danuser, G. (2005). Special issue on molecular and cellular bioimaging. *IEEE Transactions on Image Processing*, 14:1233–1236. 1.1

[79] Muzumdar, M. D., Tasic, B., Miyamichi, K., Li, L., and Luo, L. (2007). A global double-fluorescent cre reporter mouse. *Genesis*, 45. 3.1.4, 3.1.5

[80] Niakan, K. K., Han, J., Pedersen, R. A., Simon, C., and Pera, R. A. (2012). Human pre-implantation embryo development. *Development*, 139:829–841. (document), 3.1, 3.1.2

[81] Nowotschin, S., Eakin, G. S., and Hadjantonakis, A.-K. (2009). Live-imaging fluorescent proteins in mouse embryos: Multi-dimensional, multi-spectral perspectives. *Trends Biotechnol.*, 27(5):266–267. 3.1.4

[82] Nowotschin, S. and Hadjantonakis, A.-K. (2014). Live imaging mouse embryonic development: Seeing is believing and revealing. *Methods Mol Biol.*, 1092:405–420. 3.1.4

[83] Ohnishi, Y., Huber, W., Tsumura, A., Kang, M., Xenopoulos, P., Kurimoto, K., Ole, A. K., and et. al. (2014). Cell-to-cell expression variability followed by signal reinforcement progressively segregates early mouse lineages. *Nat. Cell Biol.*, 16. 3.1.2

[84] Olivier, N., Luengo-Oroz, M. A., Duloquin, L., Faure, E., Savy, T., Veilleux, I., Solinas, X., Débarre, D., Bourgine, P., Santos, A., Peyriéras, N., and Beaurepaire, E. (2010). Cell lineage reconstruction of early zebrafish embryos using label-free nonlinear microscopy. *Science*, 329(5994):967–971. 3.1.3

[85] Ortiz De Solorzano, C., Malladi, R., Lelivre, S. A., and Lockett, S. J. (2001). Segmentation of nuclei and cells using membrane related protein markers. *Journal of Microscopy*, 201(3):404–415. 3.1.3

[86] Osher, S. and Sethian, J. A. (1988). Fronts propagating with curvature dependent speed: algorithms based on hamilton-jacobi formulations. *Journal of Computational Physics*, 79:1249. 3.2.1, 3.2.2

[87] Otsu, N. (1979). A threshold selection method from gray-level histograms. *IEEE Trans. Systems Man. Cybernet*, 9:62–66. 2.2.2, 2.2.4

[88] Pedersen, U. D., Fogh, O. O., and Holm, N. O. (2003). A multiphase variational level set approach for modelling human embryos. *In: Proc. Workshop on Variational, Geometric and Level set Methods in Computer Vision*, pages 25–32. 3.1.3

[89] Peitz, I. and van Leeuwen, R. (2010). Single-cell bacteria growth monitoring by automated dep-facilitated image analysis. *Lab Chip*, 10:2944–2951. 2.1.1, 2.4.1

[90] Peng, D., Merriman, B., Osher, S., Zhao, H., and Kang, M. (1999). A pde-based fast local level set method. *Journal of Computational Physics*, 155:410–438. 3.2.5

[91] Prewitt, J. M. and Mendelsohn, M. R. (1966). The analysis of cell images. *Ann. N Y Acad. Sci*, 128:1035–1053. 1.1

[92] Price, C. S., Kon, S. E., and Metzger, S. (2014). Rapid antibiotic susceptibility phenotypic characterization of staphylococcus aureus using automated microscopy of small numbers of cells. *J Microbiol Methods*, 98:50–58. 2.1.3, 2.4.1

[93] Qi, X., Xing, F., Foran, J. D., and Yang, L. (2012). Robust segmentation of overlapping cells in histopathology specimens using parallel seed detection and repulsive level set. *IEEE Trans. Biomed Eng.*, 59:754–765. 2.2.6

[94] Read, A. F. and Woods, R. J. (2014). Antibiotic resistance management. *Evol Med Public Health*, 1. 2.1.2

[95] Richter, S. S. and Ferraro, M. J. (2007). Susceptibility testing instrumentation and computerized expert systems for data analysis and interpretation. in: Murray p. r., baron e. j., jorgensen j. h., landry m.l., pfaller m.a. eds. manual of clinical microbiology. 9th. ed. *Washington, DC: American Society for Microbiology*, pages 245–56. 2.1.3

[96] Roland, E. and Chaitanya, A. (2003). Computational imaging in cell biology. *Journ. Cell Biol.*, 161. 1.1

[97] Rossant, J. and Tam, P. P. (2004). Emerging asymmetry and embryonic patterning in early mouse development. *Dev. Cell*, 7:155–164. 3.1.2

[98] Samet, H. and Tamminen, M. (1988). Efficient component labeling of images of arbitrary dimension represented by linear bintrees. *IEEE Trans. PAMI*, 10:579. 2.2.6

[99] Satoh, R., Tsukada, H., Tanabe, Y., Gejyo, F., Tamura, Y., Yamamoto, T., Takano, M., and et. al (2008). An outbreak and isolation of drug-resistant pseudomonas aeruginosa at niigata university hospital, japan. *Journal of Infection and Chemotherapy*, 14:325–329. 2.1.1

[100] Sekiguchi, J.-I., Asagi, T., Miyoshi-Akiyama, T., Kasai, A., Mizuguchi, Y., Araake, M., and et. al (2007). Outbreaks of multidrug-resistant pseudomonas aeruginosa in community hospitals in japan. *J. Clin Microbiol.*, 45:979–989. 2.1.1

[101] Selinummi, J., Seppala, J., Yli-Harja, O., and Puhakka, J. A. (2005). Software for quantification of labeled bacteria from digital microscope images by automated image analysis. *BioTechniques*, 39:859863. 1.1, 2.2.2

[102] Sethian, J. A. (1996). A fast marching level set method for monotonically advancing fronts. *Proc. Nat. Acad. Sci*, 93:1591–1595. 3.2.5

[103] Shi, Y. and Karl, W. C. (2005). A fast level set method without solving pdes. *in?Acoustics, Speech, and Signal Processing, 1988. ICASSP-88., 1988 International Conference on*, 2:97–100. 3.2.5, 3.2.6, B.1

[104] Shi, Y. and Karl, W. C. (2008). A real-time algorithm for the approximation of level-aet-based curve evolution. *IEEE Trans Image Process.*, 17:645–656. Implementation of the level set method. 3.2.1, 3.2.5

[105] Singh, A., Buonassisi, J., Saeedi, P., and Havelock, J. (2014). Automatic blastomere detection in day 1 to day 2 human embryo images using partitioned graphs and ellipsoids. *in Proc. Image Processing (ICIP), 2014 IEEE International Conference on*. 1.3, 3.1.3, 3.3.4

[106] Skiena, S. (2008). The algorithm design manual. *Springer*, page 480. 2.2.6

[107] Spellberg, B. and Gilbert, D. N. (2014). The future of antibiotics and resistance: A tribute to a career of leadership by john bartlet. *Clin Infect Dis*, 59:71–75. 2.1.2

[108] Stephenson, R. O., Yamanaka, Y., and Rossant, J. (2010). Disorganized epithelial polarity and excess trophectoderm cell fate in preimplantation embryos lacking e-cadherin. *Development*, 137(20):3383–3391. 3.1.2

[109] Strnad, P., Gunther, S., Reichmann, J., Krzic, U., Balazs, B., de Medeiros, G., Norlin, N., Hiiragi, T., Hufnagel, L., and Ellenberg, J. (2016). Inverted light-sheet microscope for imaging mouse pre-implantation development. *Nat Meth*, 13(2). 3.3.1

[110] Tam, P. P. and Rossant, J. (2003). Mouse embryonic chimeras: tools for studying mammalian development. *Development*, 130:6155–6163. 3.1.2

[111] Tarkowski, A. K. (1959). Experiments on the development of isolated blastomers of mouse eggs. *Nature*, 184:1286–7. 3.1.2

[112] Tarkowski, A. K. and Wróblewska, J. (1967). Development of blastomeres of mouse eggs isolated at the 4- and 8-cell stage. *Development*, 18(1):155–180. 3.1.2

[113] The Center for Disease Dynamics, E. . P. (Retrieved February 15, 2017). Resistance map. *https://resistancemap.cddep.org*. 2.1.2

[114] Thouis, J. R., Anne E., C., David, S. M., and Polina, G. (2006). Methods for high-content, high-throughput image-based cell screening. *in Proc. of the Workshop on Microscopic Image Analysis with Applications in Biology held in association with MICCAI06*, pages 65–72. 2.2.2

[115] Tian, Y., Yin, Y.-b., Duan, F.-q., Wang, W.-z., Wang, W., and Zhou, M.-q. (2014). Automatic blastomere recognition from a single embryo image. *Comput Math Methods Med*, 628312. (document), 3.1.3, 3.1.3, 3.4

[116] Vapnik, V. N. (2000). *The Nature of Statistical Learning Theory*. Springer New York, New York, NY, USA. 2.2.8

[117] Viswanathan, V. K. (2014). Off-label abuse of antibiotics by bacteria. *Gut Microbes*, 5:3–4. 2.1.2

[118] Wahba, G. (1998). Support vector machines, reproducing kernel hilbert spaces and the randomized gacv. 2.2.8

[119] Wahlby, C., Sintorn, I. M., Erlandsson, F., Borgefors, G., and Bengtsson, E. (2004). Combining intensity, edge and shape information for 2d and 3d segmentation of cell nuclei in tissue sections. *Journal of Microscopy*, 215(1):67–76. 3.1.3

[120] Wang, Y.-l., Hahn, K. M., Murphy, R. F., and Horwitz, A. F. (2006). From imaging to understanding: Frontiers in live cell imaging. *Journ. Cell Biol.*, 174:481–484. 1.1

[121] Wennekamp, S., Mesecke, S., Nedelec, F., and Hiiragi, T. (2013). A self-organization framework for symmetry breaking in the mammalian embryo. *Nature Reviews Molecular Cell Biology*, 14:452–459. 3.1.2

[122] Whitesides, G. M., Ostuni, E., Takayama, S., Jiang, X., and Ingber, D. E. (2001). Soft lithography in biology and biochemistry. *Annual Review of Biomedical Engineering*, 3:335–373. 2.1.4, 2.3.1

[123] Xenopoulos, P., Nowotschin, S., and Hadjantonakis, A.-K. (2012). Live imaging fluorescent proteins in early mouse embryos. *Methods Enzymology*, 506:361389. 3.1.4

[124] Zernicka-Goetz, M., Morris, S. A., and Bruce, A. W. (2009). Making a firm decision: multifaceted regulation of cell fate in the early mouse embryo. *Nature Reviews Genetics*, 10:467–477. 3.1.2

[125] Zhang, T. Y. and Suen, C. Y. (1984). A fast parallel algorithm for thinning digital patterns. *Communications of the ACM*, 27:236–239. 2.2.6

[126] Zhou, X., Cao, X., Perlman, Z., and Wong, S. T. (2006). A computerized cellular imaging system for high content analysis in monastrol suppressor screens. *J Biomed Inform*, 39:115–125. 1.1

[127] Zhu, S. C. and Yuille, A. (1995). Region competition: Unifying snakes, region growing, and bayes/mdl for multiband image segmentation. *In: Proc. Fifth International Conference on Computer Vision, 1995, Cambridge, MA*, pages 416–423. 3.2.3

# Appendices

# Appendix A

# Implementation of the algorithm for DST with DSTM device

## A.1 Implementation details

The goal of the conducted study was not only to design an algorithm for automatic analysis of input images of the DSTM device, but also to develop a stand-alone software tool, that could be used not only by highly skilled experts, but also by those without significant knowledge in the field of bacteriology.

The software application was created using the Java programming language. The choice of this particular language was based on the fact that it is platform independent, allowing to run code on any platform without modifications. Java is also a class-based, object-oriented language, which simplifies designing and maintaining applications. In addition, built-in libraries allow developing graphical user interfaces with ease.

There is a common misconception that a program written in Java cannot be as fast as the one coded in C++. However, there is no inherent reason why an algorithm coded in C++ will run significantly faster than the same algorithm coded in Java. The execution speed depends on how good a compiler is at optimizing the generated code, and modern compilers, that translate Java byte code into machine code, can do a better job of optimization because more information is available to them about the program being compiled and about the machine that it is running on.

For convenience of processing microscopy images, the developed software has a graphical user interface (GUI). The screenshot of the GUI is presented on Figure A.1. Panel on the left side of the application window is used for browsing input files, manually selecting areas occupied by microfluidic channels, specifying number of channels and parameters for susceptibility prediction. Panel on the right displays a cumulative chart of cell frequencies with particular lengths and a table of cell features, calculated for each channel. The central area of the application window can display an input image with or without detected channels and an image where detected cells are coloured with different colours. The tools for processing input images one by one or in a batch mode are located in the top toolbar of the application window.

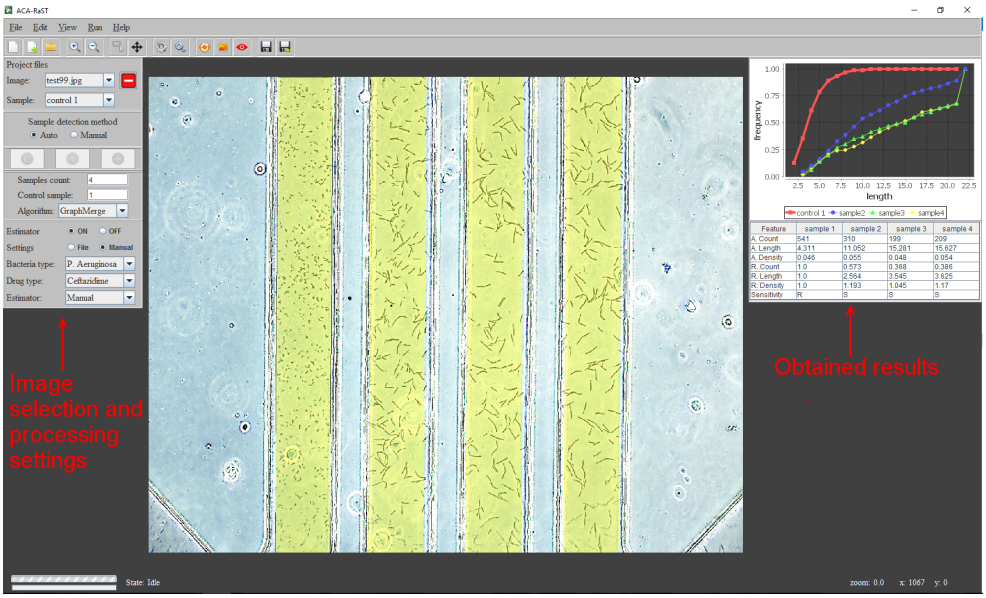


Figure A.1: A screenshot of the graphical interface of the developed software applications. The menu panels on the left side of the application allow to choose imported images, manually select channel areas, and specify processing parameters. The central area is designated for displaying input and processed images. The panel of the right displays a frequency chart and cell characteristics.

## A.2 Importing data

The developed application supports importing a single image as well as all images located in a specified folder in batch. Supported image formats are: JPEG, BMP and PNG. Each imported imaged can be selected via the menu and viewed in the main window of the application. It is possible to zoom in and out the displayed picture with the mouse or by using zoom buttons, located on the toolbar, or accessible via the *View* menu.

## A.3 Processing microscopy images

Imported images can be processed one by one or fully automatically in a batch mode. By default execution of the algorithm is performed automatically, without user intervention. Yet, in some cases it is not possible to detect all DSTM device channels on the input image automatically. The created application provides tools that allow user to manually select channels or channel areas for processing. To choose desired areas, it is necessary to click the *Select sample* button, located on the toolbar, and click and drag the mouse to select a rectangular area (see Figure A.4). Then the selected area can be added as a control or test sample by using the corresponding buttons *Add control sample* or *Add sample* located below the *Sample detection method* panel. The selected area can also be moved (*Move sample* button), allowing selecting areas with same size.

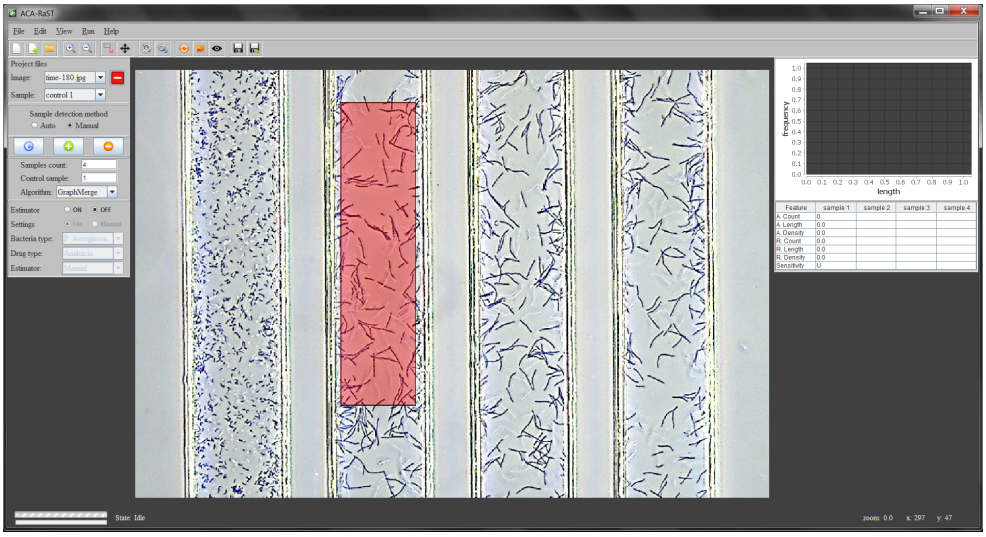


Figure A.2: A screenshot of the GUI of the application, where a channel area has been manually selected by the user.

During the course of the development of the method and the application it was observed that although the developed algorithm correctly detects channel borders, it often detects the most left and the most right positions. Thus, if a channel area is selected using this set borders it would often include dark lines, that in reality are parts of the channels, yet are perceived as bacteria by the cell detection procedure. Hence, to avoid miss-detection of cells it was decided to shrink the width of the obtained channels by moving borders closer to each other by a pre-defined margin (see Figure A.3).

## A.4 Examining the results

After computation is finished extracted cell characteristics and predicted susceptibility labels are displayed in the table located in the right panel of the application window. To visualize the distribution of cells with different lengths a cumulative histogram is built (see Fig. A.1). The calculated cell characteristics can be saved in a CSV file by choosing option *Save output as* located in the *File* menu.

There are two means of examining the output of the cell detection step of the algorithm. One way to visualize the bacteria, is to display image with cells enclosed with bounding boxes, while the other way displays colour coded bacteria. Both images can be saved, using the *Export* tab of the *File* menu.

## A.5 Processing speed

To evaluate the processing speed of the algorithm, described in Section 2.2.3, its implementation was executed on a machine that had the following characteristics: Intel Core

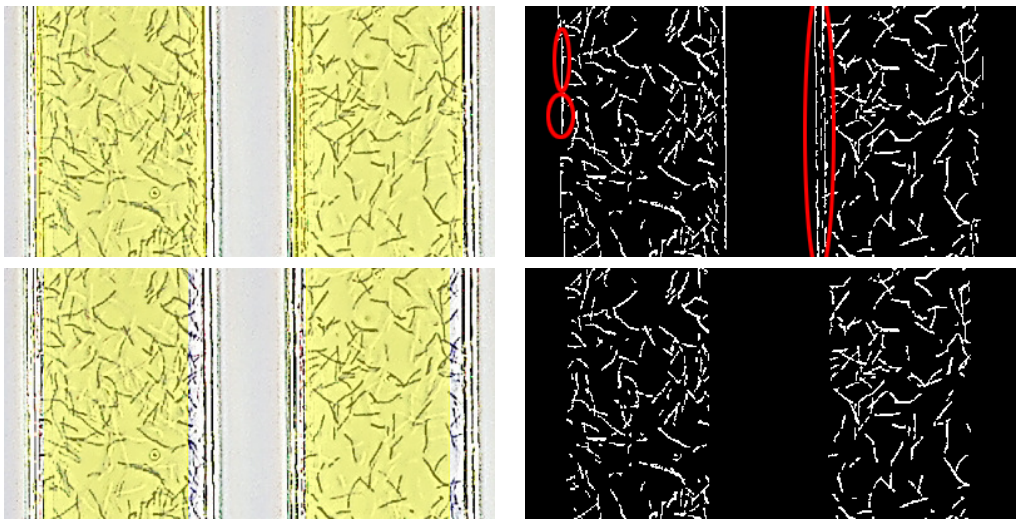

Figure A.3: Top row displays an example of cell miss-detection that occurs due to channel regions containing channel borders. Bottom row shows how shrinking of the channel area prevents treating channel borders as cells.

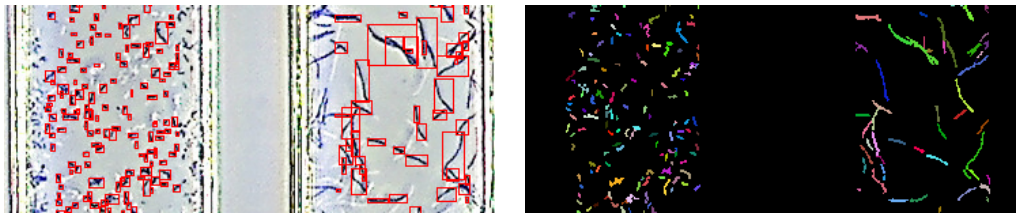

Figure A.4: Two different ways of examining output of the cell detector: (left) cells surrounded with bounding boxes; (right) colour coded cells.

i7-6700K, 4.0 GHz, 32 GB RAM. Since the cell detection step of the algorithm can be carried out independently for each channel, a parallel procedure using thread technology has been implemented.

The speed of processing varied, increasing with the number of cells. The longest time was observed for channels with highly overlapped samples (see Table A.1).

| **Cell count** | **100** | **300** | **600** |
|---|---|---|---|
| Without overlapped cells | 21s | 25s | 32s |
| With overlapped cells | 22s | 27s | 45s |

Table A.1: Processing speed, given in seconds, of the implemented algorithm for different average number of cells in a single channel.

# Appendix B

## Implementation of the algorithm for embryo segmentation

### B.1 Implementation details

The level set method has many advantages, yet its straightforward implementations that involve direct computation of certain PDEs are significantly computationally expensive. The implementation of the algorithm, described in this thesis, is based on fast level set method that avoids direct computation of the PDE, as is described in Section 3.2.5.

The whole scheme of the algorithm, including pre-processing steps that are necessary for computing sets $L_{in}$ and $L_{out}$ for each inner cell region and membranes is shown on the Figure B.1.

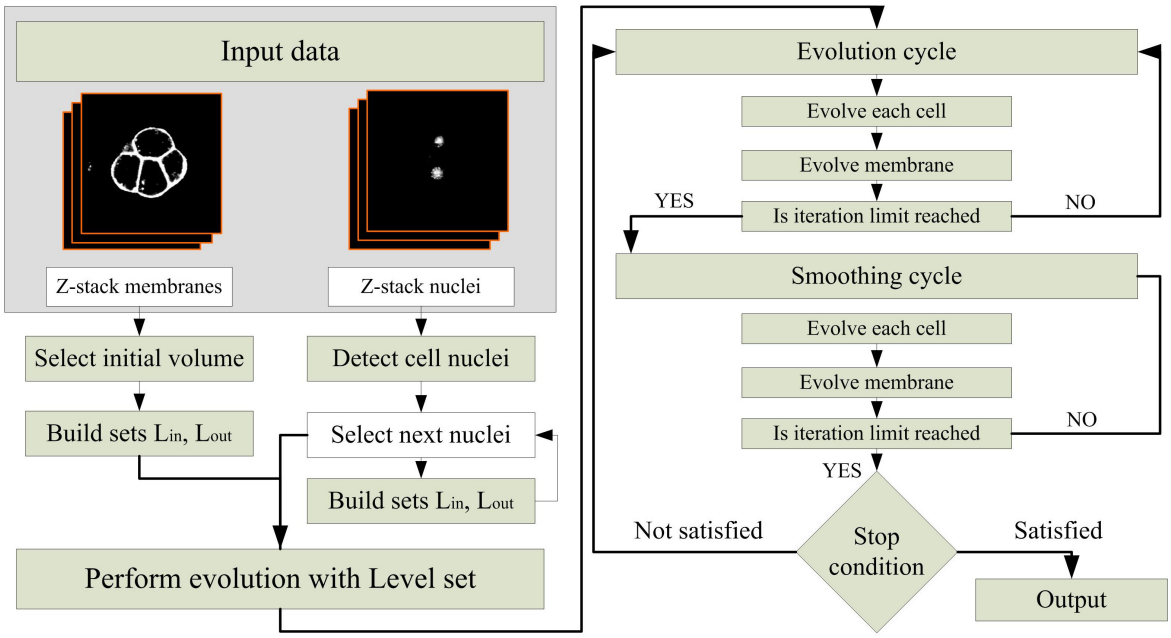


Figure B.1: A scheme of the implemented algorithm. First the sets $L_in$ and $L_out$ are computed for each inner cell region and membrane. Then the two cycle iterative algorithm is executed.

The detailed description of the fast two cycle method, written in pseudocode is given

below. The execution of the algorithm starts with initialization of two sets $L_{in}$ and $L_{out}$ for each inner cell region $\Omega_i$ in a loop, then the same sets are computed for cell membranes.

**Algorithm 1:** The main evolution procedure, that describes two main cycles of the level set implementation.

```
// initialize level set functions for cell regions
foreach cell region Ω_i do
    initialize φ_i(x, y, z), corresponding L_in(n), and L_out(n)
// initialize level set function for membrane
initialize ψ(x, y, z), corresponding L_in(n), and L_out(n)
// main loop
for t = 1, ..., T_max do
    stop = false
    // evolution cycle
    for k = 1, ..., K do
        // evolve cell regions
        foreach cell region Ω_i do
            UpdateCellRegion(Ω_i)
        // evolve membrane region
        UpdateMembraneRegion()
        if stopping condition is met then stop = true, exit cycle
    // regulation cycle
    for u = 1, ..., U do
        // evolve cell regions
        foreach cell region Ω_i do
            RegularizeCellRegion(Ω_i)
        // evolve membrane region
        RegularizeMembraneRegion()
    if stop then
        exit main loop
```

The main loop, that contains two cycles (evolution and regulation) is executed until stop condition is not met or until the maximum number of iterations $T_{max}$ is reached. Inside the *evolution cycle* the first part updates all boundaries of inner cell regions invoking procedure *UpdateCellRegion()* (see Algorithm 2), then the similar procedure *UpdateMembraneRegion()* (see Algorithm 3) is executed for membranes.

In both procedures, first, the corresponding approximation of the speed function $\hat{F}$ is computed in each point, that belong to the sets $L_{in}$ and $L_{out}$. Then for each point in set $L_out$ the sign of the speed function is checked. And, if it is more than zero, then an operation *SwitchIn(x,y,z)* is performed (see Algorithm 4), that removes point from $L_{out}$

**Algorithm 2:** Procedure UpdateCellRegion

**foreach** $(x, y, z) \in L_{in}(n) \cup L_{out}(n)$ **do** compute $\hat{F}(x, y, z)$
**foreach** $(x, y, z) \in L_{out}(n)$ **do**
  **if** $\hat{F}(x, y, z) > 0$ **then** SwitchIn(x,y,z)
UpdateInterior($L_{in}(n)$)
**foreach** $(x, y, z) \in L_{in}(n)$ **do**
  **if** $\hat{F}(x, y, z) < 0$ **then** SwitchOut(x,y,z)
UpdateExterior($L_{out}(n)$)

**Algorithm 3:** Procedure UpdateMembraneRegion

**foreach** $(x, y, z) \in L_{in}(n) \cup L_{out}(n)$ **do** compute $\hat{F}(x, y, z)$
**foreach** $(x, y, z) \in L_{out}(n)$ **do**
  **if** $\hat{F}(x, y, z) > 0$ **then** SwitchIn(x,y,z)
UpdateInterior($L_{in}(n)$)
**foreach** $(x, y, z) \in L_{in}(n)$ **do**
  **if** $\hat{F}(x, y, z) < 0$ **then** SwitchOut(x,y,z)
UpdateExterior($L_{out}(n)$)

and adds it into $L_{in}$, thus expanding the boundary surface. Then it checks neighbouring points, and adds them to $L_{out}$, initializing the level set function with the corresponding value.

**Algorithm 4:** Procedure SwitchIn

**foreach** $(x, y, z) \in L_{out}(n)$ **do**
  remove $(x, y, z)$ from $L_{out}(n)$ and add it to $L_{in}(n)$
  **foreach** $(x^*, y^*, z^*) \in N(x, y, z)$ *with* $\phi_i(x^*, y^*, z^*) = 3$ **do**
    add $(x^*, y^*, z^*)$ to $L_{out}(n)$; $\phi_i(x^*, y^*, z^*) = 1$

The procedure *SwitchOut(x,y,z)* (see Algorithm 5) is similar to the *SwitchIn(x,y,z)*, however it is responsible for shrinking the boundary by checking the sign of the speed function and removing point from $L_{in}$ and adding them to $L_{out}$.

Subroutines *UpdateInterior()* and *UpdateExterior* are necessary for cleaning the used sets $L_{in}$ and $L_{out}$ and removing all points that are not belong to these two sets.

When the execution of the evolution cycle is finished. The computations specified in the regulation cycle are carried out. In its core the steps performed in the regulation cycle are similar to the evolution cycle, described in *UpdateCellRegion()* and *UpdateMembraneRegion()*. Yet there is one major difference: instead of checking the sign of the speed function, the sign of convolution of the level set function with a gaussian filter $G$

**Algorithm 5:** Procedure SwitchOut

**foreach** $(x, y, z) \in L_{in}(n)$ **do**
  remove $(x, y, z)$ from $L_{in}(n)$ and add it to $L_{out}(n)$
  **foreach** $(x^*, y^*, z^*) \in N(x, y, z)$ *with* $\phi_i(x^*, y^*, z^*) = -3$ **do**
    add $(x^*, y^*, z^*)$ to $L_{in}(n)$; $\phi_i(x^*, y^*, z^*) = -1$

**Algorithm 6:** Procedure UpdateInterior points for the level set function $\phi_i(x, y, z)$

**foreach** $(x, y, z) \in L_{in}(n)$ **do**
  **if** $\phi_i(x^*, y^*, z^*) < 0$, $\forall (x^*, y^*, z^*) \in N(x, y, z)$ **then**
    remove $(x, y, z)$ from $L_{in}(n)$; $\phi_i(x, y, z) = -3$;

**Algorithm 7:** Procedure UpdateExterior points for the level set function $\phi_i(x, y, z)$

**foreach** $(x, y, z) \in L_{out}(n)$ **do**
  **if** $\phi_i(x^*, y^*, z^*) > 0$, $\forall (x^*, y^*, z^*) \in N(x, y, z)$ **then**
    remove $(x, y, z)$ from $L_{out}(n)$; $\phi_i(x, y, z) = 3$

(see Algorithms 8 and 9).

**Algorithm 8:** Procedure RegularizeCellRegion

**foreach** $(x, y, z) \in L_{out}(n)$ **do**
  **if** $(G * \phi_i)(x, y, z) > 0$ **then** SwitchIn(x,y,z)
UpdateInterior($L_{in}(n)$)
**foreach** $(x, y, z) \in L_{in}(n)$ **do**
  **if** $(G * \phi_i)(x, y, z) < 0$ **then** SwitchOut(x,y,z)
UpdateExterior($L_{out}(n)$)

**Algorithm 9:** Procedure RegularizeMemebraneRegion

**foreach** $(x, y, z) \in L_{out}(n)$ **do**
  **if** $(G * \psi)(x, y, z) > 0$ **then** SwitchIn(x,y,z)
UpdateInterior($L_{in}(n)$)
**foreach** $(x, y, z) \in L_{in}(n)$ **do**
  **if** $(G * \psi)(x, y, z) < 0$ **then** SwitchOut(x,y,z)
UpdateExterior($L_{out}(n)$)

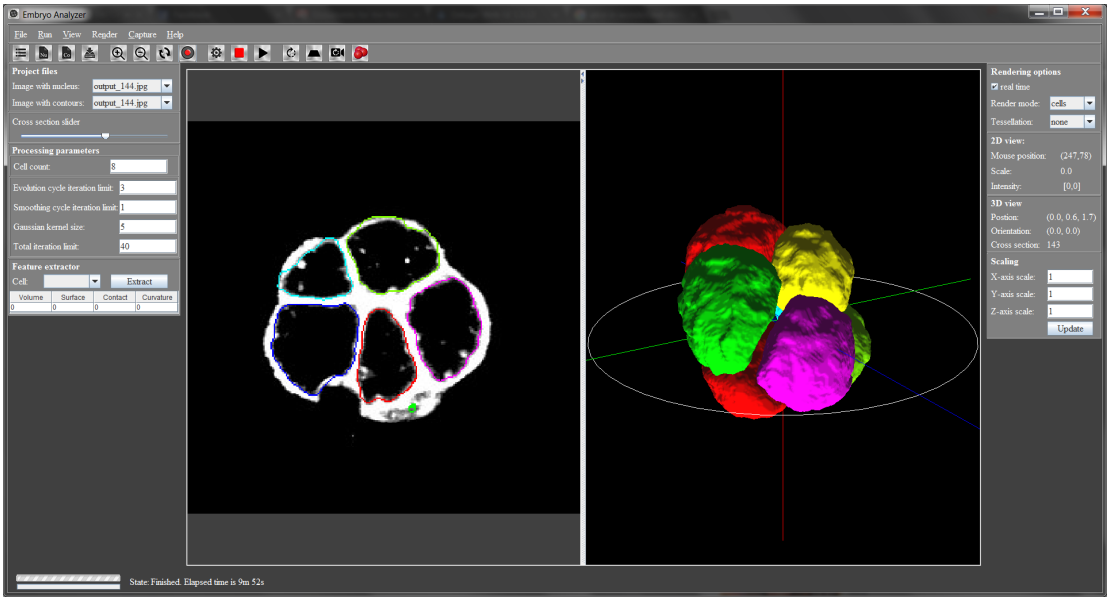


Figure B.2: The graphical user interface of the application, that implements the 3D level set method.

Thus the strength of the smoothness regulations is controlled by the size of the gaussian filter $G$ and the number of iterations $U$ done in the regulation cycle. Following suggestions given in [103] the size of the gaussian kernel was set up to 5x5x5, and for each 3 iterations of the evolution cycle one regulation was performed.

## B.2 Visualization of the segmentation

To make it easier to visualize processing steps of the developed algorithm an implementation was coded in Java, with 3D rendering of the segmentation results done with the OpenGL library. The graphical user interface of the developed software application is presented on the Figure B.2.

With the graphical interface it was possible not only render the reconstructed segmentation in 3D space, but also depict it in each one of the input cross-sections of the input images.

The results of the segmentations can be viewed not only after all computations are done, but also examined after each iteration, since the 3D and 2D renders are updated dynamically (see Figure B.3).

## B.3 Processing speed

The processing speed of the designed algorithm was measured using a machine with the following specifications: Intel Core i7-6700K, 4.0 GHz, 32 GB RAM. The Table B.1 presents the average time, required to perform segmentation for embryos with different

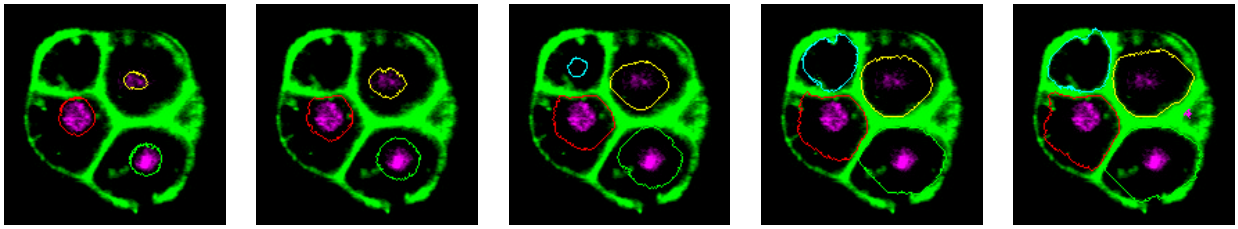

steps = 5 steps = 10 steps = 15 steps = 20 steps = 25

Figure B.3: Results of the segmentation, displayed on a cross-section, after several iteration steps.

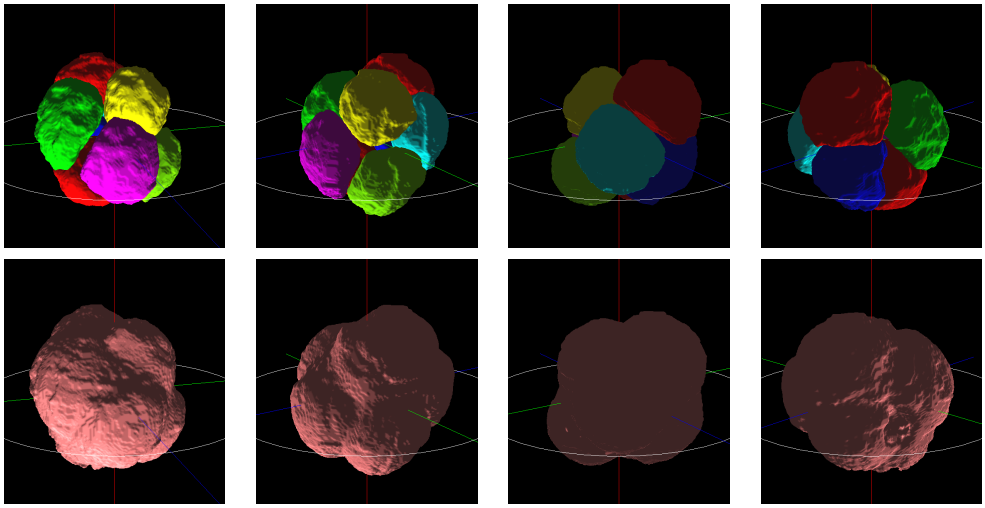

Figure B.4: Several images of the 3D renders of the segmentation results captured from different angles.

number of cells. In attempt to reduce computation time, the a version of the fast two cycle algorithm has been implemented, that avoids computation of the speed function at those points that have not been moved from set $L_{in}$ and $L_{out}$, or vice versa, for 5 of iterations (reached stability). This approached allowed slightly increase processing speed.

| Cell count | 4 | 8 | 16 | 24 | 32 |
|---|---|---|---|---|---|
| Without boosting (s) | 102 | 321 | 730 | 1621 | 2294 |
| With boosting (s) | 95 | 298 | 523 | 1501 | 2050 |

Table B.1: Processing speed, measured in seconds, for embryos with different number of cells.

The bottleneck of the algorithm is the calculation of the speed function, since each one of the speed function depends on each other. Further improvements of the processing speed could be achieved by using parallel processing, splitting sets $L_{in}$ and $L_{out}$ into batches.